UNIVERSITY OF TRENTO

Doctoral School in Civil, Environmental and Mechanical Engineering

Curriculum 3. Modelling and Simulation

Martina Azzolini

Monte Carlo Simulations of Electron Transport in 3D Solids and Molecular Dynamics Simulations of the Mechanics of 2D materials

2018 - Doctoral thesis

UNIVERSITY OF TRENTO - Italy
Department of Civil, Environmental
and Mechanical Engineering

Doctoral School in Civil, Environmental and Mechanical Engineering
Topic 3. Modelling and Simulation - XXXI cycle 2015/2018

Doctoral Thesis - May 2019

Martina Azzolini

Monte Carlo Simulations of Electron Transport in 3D Solids and Molecular Dynamics Simulations of the Mechanics of 2D Materials

Supervisors
Prof. Nicola Pugno - UNITN
Dr. Maurizio Dapor - ECT* - FBK

University of Trento
Doctoral School in Civil, Environmental and Mechanical Engineering
http://web.unitn.it/en/dricam
Via Mesiano 77, I-38123 Trento
Tel. +39 0461 282670 / 2611 - *dicamphd@unitn.it*

Abstract

The aim of this thesis is the study of electronic transport and mechanical properties of materials using computer simulations. In particular, we dealt with the charge transport in semiconductor and metallic samples and with the peeling of a graphene layer from bulk graphite. The computational methods used to investigate the samples are (i) the Monte Carlo (MC) statistical method to simulate the transport of electrons in solids and (ii) the molecular dynamic (MD) approach to study the mechanical characteristics. A relevant part of this thesis is focused on carbon-based material, such as diamond and graphite, and the stable two-dimensional allotrope, graphene. The response of diamond and graphite to external electromagnetic perturbations, due to e.g. an impinging electron beam, was investigated by calculating reflection electron energy loss (REEL) spectra with MC simulations. By comparing the calculated spectra, obtained using different dielectric models, and in-house recorded experimental results, the most effective dielectric model better describing the plasma losses was identified. Moreover, an extension to these models to describe the anisotropic response of graphite to an external electromagnetic perturbation was developed and included in the MC approach. Owing to the central role of carbon for future electronic and technological applications, also its mechanical properties were investigated by means of MD simulations. In particular, the peeling process of a layer of graphene from a bulk of graphite was investigated. This process is exploitable for graphene production and for adhesive applications of this material. Moreover, the MC approach, employed for calculating REEL spectra, was tested and compared to other computational techniques based on the solution of the Ambartsumian-Chandrasekhar equations. This consistency test was realized by considering three metals (copper, silver and gold) as target materials. Further studies were carried out on these materials by calculating secondary electron emission yields as a function of the electron beam energy. A remarkable good agreement with experimental data was obtained. The MC approach was also used to investigate the growth of particles in a $W(CO)_6$ layer deposited on a SiO_2 substrate upon irradiations by an electron beam in the context of the focused electron beam induced deposition technique. In particular, by applying the MC method, the radial distribution of emitted secondary electrons was calculated and then utilized as input data for further MD simulations. Moreover, the study of electron transport in an organic polymer (P3HT) was performed in order to understand how the molecular ordering affects the secondary electron emission. This aspect is of paramount importance to construct efficient organic electronic devices.

Contents

Chapter 1

Introduction

To completely understand complex physical phenomena, the role of modelling and simulations are becoming more and more fundamental. These procedures lay in the middle of theory and experiments. Indeed the modelling represents the transfer of the theory to the real phenomena under study, while the simulation is an in silico experiments, realized by following the statements of the theory. By comparing the results obtained from these virtual experiments and the real experimental outputs a theory can be verified and even developed. In this thesis the implementation of modelling and simulations methods is presented in the study of two different phenomena: (i) the electron transport in solid targets and (ii) the peeling of a graphene layer from a bulk of graphite. The first topic was addressed by statistical Monte Carlo (MC) model and relative simulations. The code developed to treat different materials and experimental situations. The peeling process was studied by means of Molecular Dynamic (MD) simulations and by the implementation of computational tools in order to analyze atom coordinates and record significant observables of the process. These computational methods are described in details in the **first chapter**.
The electron transport is a central topic, given the fact that electron motion is involved in a myriad of processes. Actually given the relative simplicity of handling electrons, electron microscopy and spectroscopy techniques are increasingly widespread. The use of electron beams is made in the fabrication of electronic devices and in materials characterizations. Other peculiarities are that the electrons can be detected, counted and their energy can be easily measured. As a result of inelastic interaction between traveling electrons and electron atomic clouds, secondary electrons can be generated with lower kinetic energy. They also travel inside the material, if they reach the surface with a sufficient energy, they can be emitted outside the sample. For example, in particle accelerators the electrons which remain in the proximity of the vacuum tube walls are accelerated by radio frequency waves, thus causing an avalanche of secondary electrons. This phenomenon, called multipacting effect, can produce detrimental effects on the machine stability that might result in beam loss [1, 2]. Thus, the study of electron transport is of paramount importance to well understand the mechanisms of electron interactions with different samples [3, 4, 5].

The first materials taken into account for the study on these phenomena are carbon-based materials, given their importance for future applications. Actually carbon-based materials present outstanding properties that make them optimal candidates to become constituent materials for electronic devices [6, 7]. There are different stable forms of carbon, as diamond, graphite and multi-layer graphene that can be exploited in this field. Diamond shows wide

band gap, optical isotropic structure, high thermal conductivity and charge mobility and robustness [8]. Graphite presents a layered structure, with strong two dimensional sp^2-hybridized lattice bonds in layers and softer interplanar bonds which make layers easily divisible. The anisotropy of its structure affects both mechanical and electronic properties. Indeed graphite shows higher thermal and electrical conductivity along the plane than across the plane [9, 10]. The most attractive carbon 2D material is graphene, which is composed by a honeycomb net of sp^2 bonds of carbon atoms. In this layer, electrons behave like fermions, with an extremely high mobility so that graphene can be exploited for optical and electronic devices [11]. Moreover, graphene shows attractive mechanical properties: it is characterized by superior strength, high in-plane stiffness and high Young Modulus [12]. Thus graphene shows the desired characteristic to be employed in the construction of wearable and folding systems. Moreover, in order to spread this technology, the production procedure of the material has to be efficient and scalable. Therefore for future exploitation of these carbon-based materials in the production of electronic devices both optical, electrical and mechanical properties have to be understood. In the **second chapter** the study about electron transport in diamond and graphite with MC simulations is presented. First of all effects of different dielectric models on reflection electron energy loss (REEL) spectra were examined. Then a model to consider the influence of the anisotropic structure of graphite was developed and the obtained results are shown. In particular, the outputs achieved with the simulations are compared to experimental results recorded at the laboratories of the LISC (Interdisciplinary Laboratory of Computational Science - ECT * - FBK) group and of the University of Sheffield. These studies were published in two research papers (Refs. [5, 13]). In the **third chapter** graphene and graphite are considered for mechanical tests carried out by means of MD simulations. In particular the peeling of a layer of graphene from a bulk of graphite was simulated and studied. Actually this process can constitute a new technique to produce free-standing graphene without involving chemical treatments. As a first step in the investigation, the behavior of graphene subjected to deformations under different conditions was analyzed. The adhesion energy between the two layers was calculated by realizing dedicated MD simulations. The classical theory of the peeling of an elastic layer from a solid substrate by Kendall [14] was tested for this nanoscale system and the conditions for its applicability are discussed.

The second group of materials considered as samples for our studies is metals. They are characterized by a high electron mobility and therefore by a high electron conductivity. This feature is largely exploited in electronics, where constituent elements of devices are mainly chosen among these materials. Moreover metals are also employed in the construction of particle accelerators and satellites. For these reasons, the knowledge of the electron transport properties of these materials is of paramount importance. In the **fourth chapter** the electron transport in three metals (copper silver and gold) is carefully investigated. Given the large literature regarding these samples, they were taken as standard targets to test our MC procedure with another computational tool the numerical solution of the Ambartsumian - Chandrasekhar equations using the Invariant Embedding Method [15]. This second method was developed by the computational group at the National Research University of Moscow. In particular, the methods were applied to calculate the REEL spectra of the three samples. The same input data were considered, concerning elastic and inelastic interaction, in order to significantly compare the results. A notably good agreement was found between two methods and the available experimental data [16]. The complete investigation was reported in Ref. [17]. The agreement

between calculated and experimental REEL spectra ensures that the description of the electron transport in these samples, achieved by the methods, is almost correct. Starting from this point, in the second part of the fourth chapter, the secondary electron emission yield calculation is performed. When the metal surface is irradiated by primary electrons, avalanches of secondary electrons are generated. A fraction of these secondary electrons is emitted from the surface and collected. In scanning electron microscopy [18, 19] and in electron multiplier based detectors [20, 21], the emission of secondary electrons is exploited in order to acquire sample's images. In these applications, the secondary electron emission yield should reach high values in order to guarantee images with good resolution. There are other circumstances, such as in particle accelerators, where the secondary electron emission has to be reduced or even suppressed, in order to prevent damages in the machinery [1, 2]. Some treatments [22] or creation of pattern [23] are realized on the target surfaces in order to reduce the risk of destructive effects due to secondary electrons emission. Our MC approach allows to carefully calculate the secondary electron emission yield and to predict the tendency of a specific metal to emit secondary electrons for given conditions. The optimal conditions for the employment of these materials, according to the desired yield, can be established. The simulation outputs were compared with experimental data acquired by the experimental INFN group in Frascati. This study was also reported in the published research paper (Ref. [24]).

Electron beams are also used in the fabrication of 2D and 3D nanostructures. Actually, the focused electron beam induced deposition (FEBID) technique employes a high-energy electron beam impinging on precursor adsorbed molecules on a given substrate. The beam electrons, given their high-energy, interact mainly with the substrate by producing the emission of primary and secondary electrons from the substrate. These electrons are transferred to adsorbed molecules. These additional charges involves molecules dissociation. The resulting free atoms arrange together forming nanostructures deposited on the substrate. In collaboration with the theoretical and computational group at the Univeristy of Murcia and of Alicante we intend to achieve a complete model of the FEBID process. The study is performed by combining two simulation techniques: MC simulation for the transport of the primary and secondary electrons through the substrate [5] and the irradiation driven molecular dynamics (IDMD) for the fragmentation, dynamics and reaction of precursor molecules on the substrate [25]. As a case study, 30 keV electron irradiation of $W(CO)_6$ molecules on silica (SiO_2) surface was chosen, since experimental results are available to compare to the simulations outputs. In the **fifth chapter** the first part of this complex model is reported by considering as a substrate, for the FEDIB technique, a bulk of SiO_2. First of all the MC method was tested in the calculation of SiO_2 REEL spectra by comparing the calculations with experimental data [26, 27]. Simulations with a high energy beam were performed and the electron energy spectra at several annular patches around the beam center were calculated. The electron energies and fluxes will be used to determine fragmentation rates for precursor molecules, to be used in IDMD.

The **sixth chapter** is devoted to the illustration of the study carried out in collaboration with the experimental group headed at the University of Sheffield, about the evaluation of the molecular ordering in a poly(3-hexylthiophene) (P3HT) sample via secondary electron emission spectroscopy measurements. This polymer material represents an element to be exploited in the construction of organic electronic devices. We considered an irradiated region composed by amorphous and crystalline regions. Their different electronic properties can be described by different values of electron affinity. We found out that electrons coming from regions with different molecular ordering are emitted with different energy distributions. The results are

published in Ref. [28].

Each chapter reports details about the initial conditions and the evaluations of input data. In the end, further remarks and conclusions will be provided.

Bibliography

[1] C. Lyneis, H. Schwettman, J. Turneaure, Elimination on electron multipacting in superconducting structures for electron accelerators, Applied Physics Letters 31 (8) (1977) 541–543.

[2] E. Somersalo, D. Proch, P. Ylä-Oijala, J. Sarvas, Computational methods for analyzing electron multipacting in rf structures, Part. Accel. 59 (1998) 107–141.

[3] M. Dapor, Mermin differential inverse inelastic mean free path of electrons in polymethylmethacrylate, Frontiers in Materials 2 (2015) 27.

[4] S. Taioli, S. Simonucci, L. Calliari, M. Dapor, Electron spectroscopies and inelastic processes in nanoclusters and solids: Theory and experiment, Physics Reports 493 (5) (2010) 237–319.

[5] M. Azzolini, T. Morresi, G. Garberoglio, L. Calliari, N. M. Pugno, S. Taioli, M. Dapor, Monte carlo simulations of measured electron energy-loss spectra of diamond and graphite: Role of dielectric-response models, Carbon 118 (2017) 299–309.

[6] L. L. Zhang, X. Zhao, Carbon-based materials as supercapacitor electrodes, Chemical Society Reviews 38 (9) (2009) 2520–2531.

[7] P. Avouris, Z. Chen, V. Perebeinos, Carbon-based electronics, in: Nanoscience And Technology: A Collection of Reviews from Nature Journals, World Scientific, 2010, pp. 174–184.

[8] L. S. Pan, D. R. Kania, Diamond: electronic properties and applications, Springer Science & Business Media, 2013.

[9] K. Krishnan, N. Sand Ganguli, Large anisotropy of the electrical conductivity of graphite, Nature 144 (1939) 667.

[10] B. T. Kelly, Physics of graphite, Applied Science, 1981.

[11] Y. Zhu, S. Murali, W. Cai, X. Li, J. W. Suk, J. R. Potts, R. S. Ruoff, Graphene and graphene oxide: synthesis, properties, and applications, Advanced materials 22 (35) (2010) 3906–3924.

[12] I. Ovid'Ko, Mechanical properties of graphene, Rev. Adv. Mater. Sci 34 (1) (2013) 1–11.

[13] M. Azzolini, T. Morresi, K. Abrams, R. Masters, N. Stehling, C. Rodenburg, N. Pugno, S. Taioli, M. Dapor, Anisotropic approach for simulating electron transport in layered materials: Computational and experimental study of highly oriented pyrolitic graphite, The Journal of Physical Chemistry C 122 (18) (2018) 10159–10166.

[14] K. Kendall, Thin-film peeling-the elastic term, Journal of Physics D: Applied Physics 8 (13) (1975) 1449–1452.

[15] V. Afanasev, D. Efremenko, P. Kaplya, Analytical and numerical methods for computing electron partial intensities in the case of multilayer systems, Journal of Electron Spectroscopy and Related Phenomena 210 (2016) 16–29.

[16] T. Nagatomi, Y. Takai, B. Crist, K. Goto, R. Shimizu, Construction of database of effective energy-loss functions, Surface and interface analysis 35 (2) (2003) 174–178.

[17] M. Azzolini, O. Riedzel, P. Kaplya, V. Afanasev, N. M. Pugno, S. Taioli, M. Dapor, Computational tools for calculating reel spectra in solids: a comparison between monte carlo method and the numerical solution of the Ambartsumian-Chandrasekhar equations,, Submitted.

[18] H. Seiler, Secondary electron emission in the scanning electron microscope, Journal of Applied Physics 54 (11) (1983) R1–R18.

[19] J. I. Goldstein, D. E. Newbury, J. R. M., N. W. Ritchie, J. H. J. Scott, D. C. Joy, Scanning electron microscopy and X-ray microanalysis, Springer, 2017.

[20] F. Sauli, Gem: A new concept for electron amplification in gas detectors, Nuclear Instruments and Methods in Physics Research Section A: Accelerators, Spectrometers, Detectors and Associated Equipment 386 (2-3) (1997) 531–534.

[21] J. Benlloch, A. Bressan, M. Capeáns, M. Gruwé, M. Hoch, J. Labbé, A. Placci, L. Ropelewski, F. Sauli, Further developments and beam tests of the gas electron multiplier (gem), Nuclear Instruments and Methods in Physics Research Section A: Accelerators, Spectrometers, Detectors and Associated Equipment 419 (2-3) (1998) 410–417.

[22] V. Baglin, J. Bojko, C. Scheuerlein, O. Gröbner, M. Taborelli, B. Henrist, N. Hilleret, The secondary electron yield of technical materials and its variation with surface treatments, Tech. rep. (2000).

[23] I. Montero, L. Aguilera, M. E. Dávila, V. C. Nistor, L. A. González, L. Galán, D. Raboso, R. Ferritto, Secondary electron emission under electron bombardment from graphene nanoplatelets, Applied Surface Science 291 (2014) 74–77.

[24] M. Azzolini, M. Angelucci, R. Cimino, R. Larciprete, N. M. Pugno, S. Taioli, M. Dapor, Secondary electron emission and yield spectra of metals from monte carlo simulations and experiments, Journal of Physics: Condensed Matter 31 (5) (2018) 055901.

[25] G. B. Sushko, I. A. Solov'yov, A. V. Solov'yov, Molecular dynamics for irradiation driven chemistry: application to the FEBID process*, The European Physical Journal D 70 (10) (2016) 217.

[26] M. Filippi, L. Calliari, M. Dapor, Joint experimental and computational study of silicon dioxide electron energy loss spectra, Physical Review B 75 (12) (2007) 125406.

[27] M. Dapor, Energy loss spectra of low primary energy ($E_0 \leq 1$ keV) electrons backscattered by silicon dioxide, Surface science 600 (20) (2006) 4728–4734.

[28] R. C. Masters, N. Stehling, K. Abrams, V. Kumar, M. Azzolini, N. M. Pugno, A. Dapor, M.. Huber, P. Schäfer, D. G. . Lidzey, C. Rodenburg, Secondary electron energy spectroscopy in the scanning electron microscope: Origins and applications for a conjugated polymer, Advanced Science (2019) 1801752.

Chapter 2

Computational methods

2.1 Monte Carlo simulation of electron transport

The Monte Carlo statistical method can be exploited to evaluate the transport of electron beam in solid samples. This method is based on the knowledge of characteristic probability distributions, about the interactions of the electrons with the sample, and on the generation of random numbers. Each step of the electron trajectory is determined by comparing the distribution with a random number. By performing a statistically significant number of trajectories, characteristic features of the electron transport in the sample can be obtained. In our research group, a computational tool based on the Monte Carlo method was developed in order to approach this problem. The electrons are followed from their entrance in the solid, along their entire path inside the solid till they are absorbed or emitted. When the electrons reach the surface and escape, they are collected and recorded as a function of their kinetic energy or their emission angle [1]. In the simulation, an electron beam impinges on a target surface inclined with an angle θ_0 with respect to the surface normal, with an assigned initial kinetic energy. The beam electrons interact with the scattering centres present in the solid. The calculation of trajectories is based on the evaluations of probability distributions and then on the comparison of these with random numbers uniformly distributed in the interval between 0 and 1. Here and after r is implied as a new random number for each sampling. The initial kinetic energy is sampled by considering a Gaussian distribution or the experimental distribution of the electron gun, centred at the desired initial kinetic energy. Usually, a Gaussian distribution with a full width half maximum equal to 0.4 eV is employed. Where the experimental distribution is used, it will be underlined. When the electron enters in the material, its kinetic energy is increased by the work function χ, to transfer it to the energy reference system of the solid.
Then, the electrons interact with the specimen, and different kinds of electron interactions are taken into account in the simulation. In particular:

- *elastic scattering* between electrons and atomic nuclei. It produces an angular deviation of the electron trajectory.
- *inelastic scattering* between travelling electrons and target electrons. It causes an energy loss by the travelling electron and an angular deviation of its trajectory. Moreover, the energy loss of the travelling electron can be transferred to an atomic electron, and if this energy is high enough a secondary electron is emitted and also its trajectory is simulated.

- *electron-phonon interaction* involves a fixed energy loss (W_{ph}) by the travelling electrons and an angular deviation of its trajectory.
- *trapping phenomena* which ends the trajectory. All the electron energy is locally deposited.

Each interaction is quantified by the corresponding cross section. These quantities will be denoted as σ_{el} for the elastic scattering, σ_{inel} for the inelastic scattering, σ_{ph} for the electron-phonon interaction and σ_{trap} for the trapping phenomena. The scattering cross section are related to the corresponding mean free path (λ) by this simple relation:

$$\lambda = \frac{1}{N\,\sigma}\,, \tag{2.1}$$

where N is the scattering centres density (number of scattering centres for unit volume).
The electron path is assumed to be described by a Poisson-like law, so the step length (Δs) between two subsequent collisions is given by:

$$\Delta s = -\lambda_{tot}\ln(r), \tag{2.2}$$

where λ_{tot} is the total mean free path, which depends on the kinetic energy of the travelling electron, and its calculated as:

$$\frac{1}{\lambda_{tot}} = \frac{1}{\lambda_{el}} + \frac{1}{\lambda_{inel}} + \frac{1}{\lambda_{ph}} + \frac{1}{\lambda_{trap}}. \tag{2.3}$$

The electron takes a step Δs. Then the kind of the interaction has to be chosen. This decision is performed in the calculation by comparing the probabilities to undergo each kind of interaction with a random number. The interaction probabilities are computed as:

$$p_i = \frac{\lambda_{tot}}{\lambda_i}, \tag{2.4}$$

where i stands for the different interaction kind. By this definition the sum of these probabilities is normalized to one and the 4 numbers [p_{el}, $p_{el} + p_{inel}$, $p_{el} + p_{inel} + p_{ph}$, 1] are considered. The value of the random number r is compared to these numbers and depending on which segment it belongs, the kind of interaction is identified. At this point the trajectory and the energy of the electron are modified according to the kind of the interaction suffered by the particle. After a series of interactions, the electron can reach the target surface and can be emitted from the target surface, provided that the emission condition is fulfilled. This emission condition is related to the target-vacuum interface, which represents by all means an energy barrier to be overcome. This condition is formulated as:

$$E\cos^2\bar{\theta} \geq \chi, \tag{2.5}$$

where $th\bar{e}ta$ is the angle inside the target between the electron trajectory and material the normal to the surface, E is the electron kinetic energy and χ the work function of the specimen.

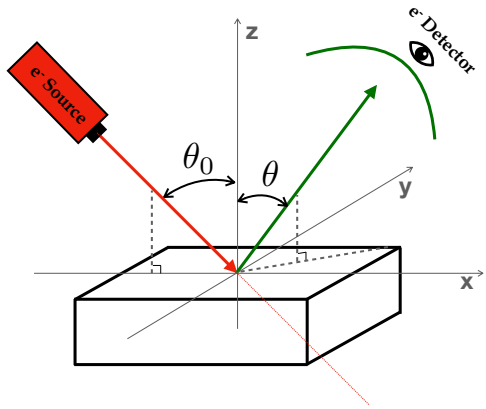

FIGURE 2.1: System considered in the simulation and experimental layout of a typical reflection electron energy loss measurement [3].

The surface emission probability is evaluated by comparing a random number with the transmission coefficient t. This is obtained by solving the problem of a step potential [1]:

$$t = \frac{4\sqrt{1-\chi/(E\cos^2\alpha)}}{\left[1+\sqrt{1-\chi/(E\cos^2\alpha)}\right]^2}. \tag{2.6}$$

If $r > t$, the electron is reflected back to the solid continuing its path inside the target; otherwise, it is emitted from the surfaced and its kinetic energy is diminished by χ. The ensemble of trajectories used in MC simulations of emission spectra is assessed so to reach statistical significance and low noise of the simulated data. Further details on the MC approach can be found in Refs. [1, 2]. In Fig. 2.1 a graphical layout of the simulated system is illustrated.

The following sections report a detailed description of each kind of interaction and of trajectory variations due to different collisions.

2.1.1 Elastic scattering: Mott theory

The elastic scattering between the travelling electron and the atomic nuclei is described by the Mott theory [1, 4, 5, 6]. This approach is based on the Partial Wave Expansion Method to solve the Dirac equation: this procedure therefore considers the quantum nature of the electron. Indeed, in this case, the use of the Rutherford cross section is not allowed, since we are considering electron with a kinetic energy lower than 5 keV. In this energy region the Born approximation, which requires that $E >> \frac{e^2Z^2}{2a_0}$, is not satisfied (with e the electron charge, Z the atomic number of the specimen and a_0 the Bohr radius). In particular, the Dirac equation describes the motion of charged particle with spin. In this case we consider the electrons subjected to a central spherical potential. The Dirac equation is given by:

$$\frac{d\phi_l^{\pm}(r)}{dr} = \frac{k^{\pm}}{r}\sin[2\phi_l^{\pm}(r)] - \cos[2\phi_l^{\pm}(r)] + W - V(r). \tag{2.7}$$

There the distances are given in unit of $h/(2\pi mc)$, with h the Planck constant, m the electron mass, c the speed of light. The energy is reported in unit of mc^2.
In the Eq. (2.7) $W = \frac{E+mc^2}{mc^2}$, with E the kinetic energy of the electron. $k^{\pm}$ are quantum numbers: in particular $k^{+} = -l-1$ and $k^{-} = l$ where l is the angular momentum quantum number. The functions obtained solving the previous equations are employed in the calculation of the phase shifts between the incoming and outcoming waves:

$$\tan\delta_l^{\pm} = \frac{Kj_{l+1}(Kr) - j_l(Kr)[(W+1)\tan\phi_l^{\pm} + (1+l+k^{\pm})/r]}{Kn_{l+1}(Kr) - n_l(Kr)[(W+1)\tan\phi_l^{\pm} + (1+l+k^{\pm})/r]}, \tag{2.8}$$

j_l and n_l are the regular and irregular Bessel functions, K is defined as $K^2 = W^2 - 1$ and $\phi_l^{\pm} = \lim_{r\to\infty}\phi_l^{\pm}(r)$. The differential cross section can be computed as:

$$\frac{d\sigma_{\mathrm{el}}}{d\Omega} = |f|^2 + |g|^2, \tag{2.9}$$

where the direct scattering amplitude is defined as:

$$f(\theta) = \frac{1}{2iK}\sum_{l=1}^{\infty}\{(l+1)[e^{2i\delta_l^{+}} - 1] + l[e^{2i\delta_l^{-}} - 1]\}P_l(\cos\theta), \tag{2.10}$$

with P_l the Legendre polynomials, while the spin-flip scattering amplitude is computed as:

$$g(\theta) = \frac{1}{2iK}\sum_{l=1}^{\infty}\{-e^{2i\delta_l^{-}} + e^{2i\delta_l^{+}} - 1]\}P_l^1(\cos\theta), \tag{2.11}$$

where $P_l^1(x) = (1-x^2)^{(1/2)}\frac{dP_l(x)}{dx}$ [7]. The total elastic scattering cross section is calculated as:

$$\sigma_{\mathrm{el}} = \int \frac{d\sigma_{\mathrm{el}}}{d\Omega}d\Omega = 2\pi\int_0^{\pi}\frac{d\sigma_{\mathrm{el}}}{d\Omega}\sin(\theta)d\theta \tag{2.12}$$

Evaluation of angular deflection due to an elastic interaction

The cumulative elastic probability is then defined, for any given kinetic energy E and fixed scattering angle $\bar{\theta}$, as

$$P_{\mathrm{el}}(\bar{\theta}, E) = \frac{1}{\sigma_{\mathrm{el}}}2\pi\int_0^{\bar{\theta}}\frac{d\sigma_{\mathrm{el}}}{d\Omega}\sin(\theta')d\theta' \tag{2.13}$$

A database is constructed and filled by the values of P_{el}, calculated for different values of the electron kinetic energy and for different values of angles $\bar{\theta}$ (the upper limit of the integral). The angular deflection of the trajectory is evaluated by generating a random number r, and by

finding the value of the upper extreme of integration $\bar{\theta}$ in Eq. (2.13) that produces a value of P_{el} equal to r.

Ganachaud and Mokrani correction

For low kinetic energy, the total elastic cross section σ_{el} reaches high values, involving a too low value of the elastic mean free path λ_{el} (lower than the characteristic lattice parameter of the target crystal structure). Therefore, when this condition occurs, a correction to the Mott cross-section at low energy is applied [8]. The σ_{el} is multiplied by the cut-off function $R(E)$ proposed by Ganachaud and Mokrani [9]:

$$R(E) = \tanh\left(\alpha\, E^2\right) \tag{2.14}$$

where α is a parameter to be determined. Thus, by applying the Ganachaud and Mokrani empirical correction, the pure elastic scattering is turned off gradually, so that the main quasi elastic interaction is the electron-phonon one.

2.1.2 Inelastic scattering: Ritchie Dielectric theory

The travelling electron in the solid is slowed down by single interaction with orbital electrons. The energy loss can be calculated by evaluating the dielectric function $\epsilon(\vec{q}, W)$ of the target material as a function of the momentum $\vec{q}$ and energy W transferred. The dielectric function measures the capability of a medium to be polarized or to absorb energy given the action of electromagnetic waves (that could arise from an applied field or by a travelling charged particle) [10]. Within the dielectric theory developed by Ritchie [11], the key ingredient is the energy loss function (ELF), which is defined as the imaginary part of the negative reciprocal dielectric function:

$$\text{ELF} = \text{Im}\left[-\frac{1}{\epsilon(\vec{q}, W)}\right]. \tag{2.15}$$

In the optical limit, where the transferred momentum tends to zero ($\vec{q} \longrightarrow 0$), the ELF can be fitted by a sum of Drude–Lorentz (D–L) oscillators as follows [12]:

$$\text{Im}\left[-\frac{1}{\epsilon(\vec{q}=0, W)}\right] = \sum_n \frac{A_n \Gamma_n W}{(E_n^2 - W^2)^2 + W^2\Gamma_n^2}, \tag{2.16}$$

where A_n is the excitation strength of the n-th oscillator, Γ_n the damping constant characterizing the finite life-time of the quasi-particle excitation, and E_n the plasmon excitation energy. The optical ELF is then extended to finite transferred momentum by applying the following dispersion law [13]:

$$E_n(\vec{q} \neq 0) = E_n(\vec{q} = 0) + \frac{\hbar^2 q^2}{2m}, \tag{2.17}$$

where m is the electron mass and $\hbar$ is the reduced Planck constant.
Moreover, from the ELF, the differential inverse inelastic mean free path (DIIMFP) can be computed as:

$$\frac{d\lambda_{\text{inel}}^{-1}}{dW} = \frac{1}{\pi E a_0} \int_{q_-}^{q+} \frac{dq}{q} \text{Im}\left[-\frac{1}{\epsilon(\vec{q}, W)}\right], \tag{2.18}$$

where a_0 is the Bohr radius and E the electron kinetic energy. The limits of integration of the integral in Equation (2.18) are set to $q_\pm = \sqrt{2mE} \pm \sqrt{2m(E-W)}$ (momentum conservation). Finally, the inelastic mean free path (IMFP) can be obtained by integrating the DIIMFP in the energy loss interval:

$$\lambda_{\text{inel}}^{-1} = \int_{E_{\text{th}}}^{(E+E_{\text{th}})/2} \frac{d\lambda_{\text{inel}}^{-1}}{dW} dW. \tag{2.19}$$

As bottom value of the integration interval the (E_{th}) energy threshold is considered. Depending on the electronic structure of the sample it is set equal to 0, to the binding energy or to the energy band gap. As upper limit of the integral is set the half of the sum of the kinetic energy and the energy threshold, due to the indistinguishability between the two electrons involved in the interaction. Moreover it is assumed that the travelling electron remain the most energetic after the inelastic interaction. Given the fact that the electrons are indistinguishable, we assume that the traveling electron is the one wich loses loss energy in the collision, so we set the maximum value of the integration interval to its

Evaluation of energy loss and angular deflection due to an inelastic interaction

The energy loss W of an inelastic scattering is evaluated by calculating the inelastic cumulative distribution $\text{P}_{\text{inel}}(E, W)$.

$$\text{P}_{\text{inel}}(E, W) = \lambda_{\text{inel}} \int_0^W \frac{d\lambda_{\text{inel}}^{-1}}{dW'} dW' \tag{2.20}$$

which depends on the kinetic energy E and on the energy loss W . A database composed by its values, for different kinetic energies and energy losses is constructed. The energy loss W is then determined by generating a random number r and by finding the value of P_{inel} equal to r. The angular deviation β is computed as $\sin^2(\beta) = W/E$ (energy and momentum conservation), with E the kinetic energy of the travelling electron.

Generation of secondary electrons

If a travelling electron loses an energy W higher than the threshold energy $< B >$, the energy is transferred to an orbital electron, which is finally emitted and named secondary electron. Its trajectory is also calculated and its path starts with an initial kinetic energy equal to $W - < B >$. Otherwise, if the energy loss W results to be smaller than the threshold energy $< B >$, the emission of a secondary electron does not occur, but the atom can be excited. In turn the atom de-energizes by emitting X-rays or Auger electrons. The value of $< B >$ is determined according to the electronic characteristics of the target material.

2.1.3 Electron - phonon interaction

The travelling electron can interact with optical phonons of the target material involving a phonon creation by transferring energy by the electron. This quasi - elastic interaction is described by the Fröhlich theory [14] and according to the formulation by Llacer and Garwin [15] the inelastic mean free path is given by:

$$\lambda_{\mathrm{ph}}^{-1} = \frac{1}{a_0}\frac{\epsilon_0 - \epsilon_\infty}{\epsilon_0 \epsilon_\infty}\frac{W_{\mathrm{ph}}}{E}\frac{n(T)+1}{2}\ln\left[\frac{1+\sqrt{1-W_{\mathrm{ph}}/E}}{1-\sqrt{1-W_{\mathrm{ph}}/E}}\right], \tag{2.21}$$

where a_0 is the Bohr radius, ϵ_0 and ϵ_∞ are the static and the high frequency dielectric constants respectively and W_{ph} is the energy loss transferred from the electron to the phonon. The occupation number $n(T)$ is defined as:

$$n(T) = \frac{1}{e^{W_{\mathrm{ph}}/k_{\mathrm{B}}T} - 1}, \tag{2.22}$$

with T the temperature and k_{B} the Boltzmann constant. Given the fact that the phonon energy is in the order of $k_{\mathrm{B}}T_{\mathrm{D}}$, with T_{D} the Debye temperature, the characteristic energy loss of this interaction W_{ph} does not exceed 0.1 eV [1]. Its value will be determined according to the target material characteristics and will be indicated for each different situation.

2.1.4 Trapping phenomena

Trapping phenomena are able to literally stop the electron trajectory. Depending on the electronic structure of target material different phenomena can occur. Conductor and semiconductor materials can present impurities or local deformations of crystalline structure that can act as traps for electrons, and affecting the charge mobility [16, 17, 18]. In case of insulating material, the main trapping phenomenon is represented by the generation of polarons. They are quasi-particles due to the interaction of the electron with the polarizing field generated from its passage [9]. The mean free path characteristic of the trapping phenomena is defined by Ganachaud and Mokrani [9] as:

$$\lambda_{\mathrm{trap}}^{-1} = C_{\mathrm{trap}}\, e^{-\gamma_{\mathrm{trap}}E}, \tag{2.23}$$

where C_{trap} and γ_{trap} are characteristic parameters of the sample.

2.2 Molecular Dynamics simulation

Molecular Dynamics (MD) simulation allows the study of the time evolution of a system composed by atoms or molecules. It is based on the computation of the trajectories of these elements in a given time interval. This method provides the measurement of important and interesting quantities that can be compared to experiments data. In particular, the model is based on the assumption that atoms and molecules are subjected to Newton laws of classical mechanics of a many-body system. This assumption is valid if the de Broglie wavelength, defined as $\lambda = h/p$ (h Planck constant, p particle momentum), results to be significantly smaller than the mean neighbor separation. Assuming that the system is composed by N particles, atoms or molecules, their temporal evolution is determined by solving the related system of equations of motion:

$$m_i \vec{r}_i'' = \vec{F}_i = -\nabla_{\vec{r}_i} U(\vec{r}) \tag{2.24}$$

where $\vec{r} = (\vec{r_1}, \vec{r_2}, ...\vec{r_N})$ is the vector containing the Cartesian coordinates $\vec{r_i} = (x_i, y_i, z_i)$ of each item of the system, $\vec{F_i}$ is the force acting on the i-element. The interatomic potential $U(\vec{r})$ determines the time evolution of the system and depends on the positions of all the particles in the system. Hence, the time evolution totally depends on the choice of the interatomic potential. It has to be selected according to the aim of the simulation, which observables are attempting to measure, and the kind of the sample, chemical elements, and bonds. For our purposes, with samples composed of carbon atoms, the adaptive intermolecular reactive empirical bond-order (AIREBO) potential was used [19]. The MD simulations were performed by using the LAMMPS software [20], where the time integration of equations of motion is performed for a given system and interatomic potential. The system of motion equations was solved by applying the Verlet algorithm. It provides the formulation for the system arrangement positions at the subsequent interval of time $t + \Lambda t$, known the state of the system at previous timesteps t and $t - \Lambda t$ [21].

$$\vec{r}(t + \Lambda t) = 2\vec{r}(t) - \vec{r}(t - \Lambda t) + (\Lambda t)^2 \vec{r}''(t) \tag{2.25}$$

Then thex velocity is given by:

$$\vec{r}' = [\vec{r}(t + \Lambda t) - \vec{r}(t - \Lambda t)]/2(\Lambda t) \tag{2.26}$$

To perform the integration with this method, initial conditions for positions and velocities at previous time steps have to be provided.

The first step for performing MD simulation is the initialization of the system. First of all, the structure is generated, by determining the values of atoms coordinates. In the following case study, the considered atom structure was constructed by using a Python code which generates coordinate of atoms given the desired geometry of the system. The system is contained in a fixed 3D cell. The walls of this box are subject to boundary conditions. If the boundary conditions are periodic, the particles can move from one side to the other and interact across the boundary, otherwise the walls block any kind of interaction and overcoming of particles.

On this generated particle structure the energy and force minimization is performed in order to relax the system in a balanced configuration. This minimization is realized by applying the conjugate gradient method and by considering the system at $0°$K. After minimization velocities are assigned to each element, with a uniform distribution of values and randomly in direction. The velocity value is determined according to the set temperature of the system.

After energy and force minimization and velocities assignment, the system can be evolved by setting the ensemble in which perform the integration. In our computation different ensembles were used:

- *canonical ensemble*: where the number of particles, the cell volume, and the temperatures are maintained constant;
- *isothermal-isobaric ensemble*: involves constant number of particles, system pressure and temperature;
- *microcanonical ensemble*: requires constant number of particles, system volume and energy. In our calculation where this ensemble was set, the temperature was kept constant by the action of a *Langevin thermostat.* This thermostat act directly on the equation of motion, by adding a friction component to the force, in order to dissipate heat and maintaining constant the temperature [22].

To thermalize the system at the desired temperature of the experiment, the system is kept for a sufficient interval of time at the desired temperature and without adding modification. In this period it is assured that the system is in a relaxed configuration at the required conditions. At this point, different perturbations as a forced movement of atoms or deformation on the cell can be applied to the system. Thus it is evolved by solving the equations of motion with these constraints. During the simulation, different observables can be measured in order to control the system evolution. In the chapter 3.3 the application of this method to the calculation of mechanical properties of a graphene layer, the calculation of the adhesion energy between two layers of graphene and the peeling of a graphene layer from a bulk of graphite are reported.

Bibliography

[1] M. Dapor, Transport of Energetic Electrons in Solids, Vol. 257, Springer Tracts in Modern Physics, 2017.

[2] S. Taioli, S. Simonucci, L. Calliari, M. Dapor, Electron spectroscopies and inelastic processes in nanoclusters and solids: Theory and experiment, Phys. Rep. 493 (5) (2010) 237 – 319.

[3] M. Azzolini, O. Riedzel, P. Kaplya, V. Afanasev, N. M. Pugno, S. . Taioli, M. Dapor, Computational tools for calculating reel spectra in solids: a comparison between monte carlo method and the numerical solution of the Ambartsumian-Chandrasekhar equations,, Submitted to Frontiers in Materials.

[4] N. Mott, The scattering of fast electrons by atomic nuclei, Proc. R. Soc. London, Ser. A 124 (794) (1929) 425.

[5] S. Taioli, S. Simonucci, M. Dapor, Surprises: when ab initio meets statistics in extended systems, Computational Science and Discovery 2 (1) (2009) 015002.

[6] S. Taioli, S. Simonucci, L. Calliari, M. Filippi, M. Dapor, Mixed ab initio quantum mechanical and monte carlo calculations of secondary emission from SiO_2 nanoclusters, Phys. Rev. B 79 (2009) 085432.

[7] M. Dapor, Elastic scattering calculations for electrons and positrons in solid targets, Journal of applied physics 79 (11) (1996) 8406–8411.

[8] M. Dapor, R. C. Masters, I. Ross, D. G. Lidzey, A. Pearson, I. Abril, R. Garcia-Molina, J. Sharp, M. Unčovskỳ, T. Vystavel, Secondary electron spectra of semi-crystalline polymers–a novel polymer characterisation tool?, J. Electron Spectrosc. Relat. Phenom. 222 (2018) 95–105.

[9] J. Ganachaud, A. Mokrani, Theoretical study of the secondary electron emission of insulating targets, Surf. Sci. 334 (1995) 329.

[10] H. Nikjoo, S. Uehara, D. Emfietzoglou, Interaction of radiation with matter, CRC Press, 2012.

[11] R. H. Ritchie, Plasma losses by fast electrons in thin films, Phys. Rev. 106 (1957) 874.

[12] R. H. Ritchie, A. Howie, Electron excitation and the optical potential in electron microscopy, The Philosophical Magazine 36 (2) (1977) 463.

[13] M. Azzolini, T. Morresi, G. Garberoglio, L. Calliari, N. M. Pugno, S. Taioli, M. Dapor, Monte carlo simulations of measured electron energy-loss spectra of diamond and graphite: Role of dielectric-response models, Carbon 118 (2017) 299–309.

[14] H. Fröhlich, Electrons in lattice fields, Advances in Physics 3 (11) (1954) 325–361.

[15] J. Llacer, E. L. Garwin, Electron-phonon interaction in alkali halides. i. the transport of secondary electrons with energies between 0.25 and 7.5 ev, Journal of Applied Physics 40 (7) (1969) 2766–2775.

[16] D. W. DiMaria, D. J .and Dong, C. Falcony, T. N. Theis, J. R. Kirtley, J. C. Tsang, D. R. Young, F. L. Pesavento, S. D. Brorson, Charge transport and trapping phenomena in off-stoichiometric silicon dioxide films, Journal of applied physics 54 (10) (1983) 5801–5827.

[17] J. Schafferhans, Investigation of defect states in organic semiconductors: Towards long term stable materials for organic photovoltaics, Ph.D. thesis, Universität Würzburg, Fakultät für Physik und Astronomie (2011).

[18] L. Kaake, P. F. Barbara, X.-Y. Zhu, Intrinsic charge trapping in organic and polymeric semiconductors: a physical chemistry perspective, The Journal of Physical Chemistry Letters 1 (3) (2010) 628–635.

[19] S. J. Stuart, A. B. Tutein, J. A. Harrison, A reactive potential for hydrocarbons with intermolecular interactions, The Journal of Chemical Physics 112 (14) (2000) 6472–6486.

[20] S. Plimpton, Fast parallel algorithms for short-range molecular dynamics, Journal of Computational Physics 117 (1) (1995) 1–19.

[21] D. Frenkel, B. Smit, Understanding Molecular Simulation, 2nd Edition, Academic Press, Inc., Orlando, FL, USA, 2001.

[22] T. Schneider, E. Stoll, Molecular-dynamics study of a three-dimensional one-component model for distortive phase transitions, Physical Review B 17 (3) (1978) 1302.

Chapter 3

Carbon based materials I: electron transport in diamond and graphite

3.1 Different dielectric descriptions of diamond and graphite

In this section, the impact of different theoretical descriptions of the dielectric response of diamond and graphite on the calculation of Reflection Electron Energy Loss (REEL) spectra was investigated. The dielectric models are presented in details and afterwards the results concerning observables, such as inelastic mean free paths and cross sections calculated with these different approaches are also presented. Finally, the comparison with the experimental data (acquired in the LISC group laboratories) allows identifying the dielectric theoretical approach that ensures the most accurate description of the inelastic interaction. This study was published as research paper in Ref. [1].

3.1.1 Dielectric models

The key quantity for the electron energy loss description is represented by the Energy Loss Function (ELF) [Eq. (2.15)] that is directly obtained from the dielectric function $\epsilon(\vec{q}, W)$ as previously explained in Section 2.1.2. For this investigation ELFs acquired with different techniques were taken into account. In one case dielectric functions of diamond and graphite were calculated by *ab initio* procedure in the optical limit and for different values of the transferred momentum [1]. Then the corresponding ELFs were simply computed according to Eq. (2.15) and afterwards directly employed in Eq. (2.18), without using the fitting and expansion procedures Eqs. (2.16) and (2.17). This is the first approach considered and it is a *full ab initio* calculation. The relative results will be denoted with **AI** label.
The second approach starts from the dielectric response in the optical limit obtained from the *ab initio* calculation, while the extension to finite transferred momentum is obtained by fitting the ELF in the optical domain (Eq. 2.16) and then by applying the quadratic dispersion law

n	E_n (eV^2)	Γ_n (eV)	A_n (eV)
1	21.59	0.95	8.58
2	25.40	5.68	61.62
3	32.28	11.38	626.46
4	36.39	5.25	224.76

TABLE 3.1: Fitting parameters of *AI* ELF in the optical limit with D–L functions for diamond [1].

n	E_n (eV^2)	Γ_n (eV)	A_n (eV)
1	6.75	1.17	6.38
2	27.76	8.68	573.09

TABLE 3.2: Fitting parameters of AI ELF in the optical limit with D–L functions for graphite [1].

(Eq. 2.17). To best fit the *ab initio* ELF of diamond in the optical limit, four harmonic oscillators were considered, while for the function of graphite two oscillators were necessary. These best fits fulfill the f-sum rule [2]: this means that the integral of the ELF multiplied by the energy loss sums up to the number of effective-electrons per atom [3], i.e. the valence electrons in our model. The corresponding parameters of these best fit procedures are reported in Tabs. 3.1 and 3.2. In Fig. 3.1 the comparison between the AI dielectric response (red curve) for diamond (left panel) and graphite (right panel) obtained in the optical limit with the D–L fit (dashed black line) is presented. This approach, which starts with *ab initio* data and then includes the D–L procedures, will be denoted with the **DL-AI** label.

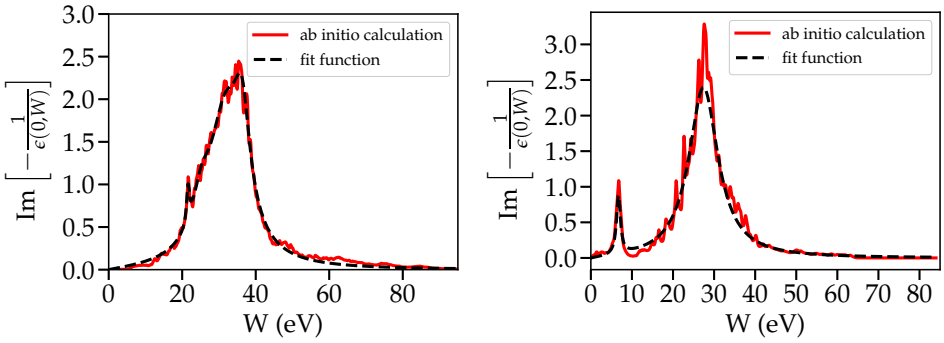

FIGURE 3.1: ELF in the optical limit ($\omega \to 0$) obtained from AI simulations (continuous red curve) along with the data fit (dashed black line) for diamond (left panel) and graphite (right panel) [1].

The third approach is given by the use of ELFs, in the optical limit, that were directly measured in transmission electron energy-loss experiments. Then, as fit values those reported by Garcia-Molina *et al.* [4] were taken into account. The expansion outside the optical limit was performed by applying the quadratic dispersion law (Eq. 2.17). Given the experimental origin of these ELFs, this approach will be denoted as *Drude–Lorentz from experimental optical data* **(DL–E)**. Figure 3.2 reports ELFs of diamond and graphite (respectively left and right panel) in the optical limit: (i) *ab initio* calculated, (ii) from experiments and taken from references [5] and [6] and (iii)best fit achieved by Garcia-Molina *et al.* [4].

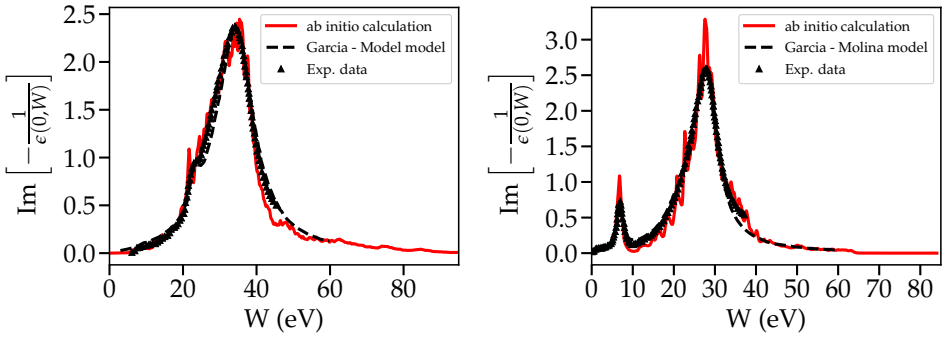

FIGURE 3.2: Comparison between the ELF of diamond (left panel) and graphite (right panel) in the optical limit obtained from AI simulations (continuous red curve), experimental data from Refs. [5] and [6] (black triangles) and fit obtained with the model of Garcia-Molina *et al.* [4] (dashed black line) [1].

Inelastic mean free path calculation

Inelastic mean free paths (IMFP) for diamond and graphite were calculated starting from the three different approaches of dielectric descriptions [Eq. (2.19)]. IMFPs for different kinetic energies are reported in Fig. 3.3 and compared with calculated data with the Tanuma-Powell-Penn (TPP) model [7].

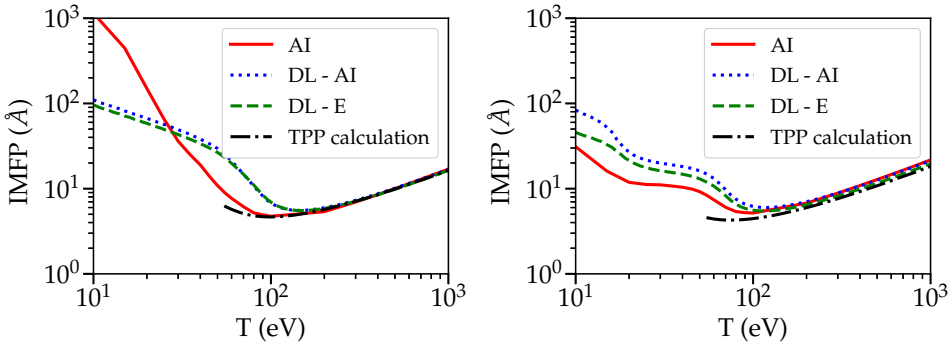

FIGURE 3.3: IMFP of diamond (left) and graphite (right). Data obtained from AI simulations are reported in red (AI), DL-AI in blue and with the DL-E in green. Black dashed lines correspond to the same quantities obtained by Tanuma *et al.* (TPP) [7] [1].

Fig. 3.3 shows a very good agreement, for energies higher than 100 eV, between results achieved with the different approaches and the reference curve by Tanuma, Powell and Penn (TPP). The discrepancy found for lower energy can be attributed to the different dispersion

laws applied to extend the ELFs outside the optical limit. Indeed, the discrepancy is relevant among the results obtained with the quadratic dispersion law (DL-AI and DL-E) with the ones obtained with the full ab initio calculation (AI). The quadratic dispersion law is derived from the hypothesis of a homogeneous electron gas model. Actually, diamond is a semiconductor, with a wide band gap, and graphite presents an anisotropic structure with metallic behaviour in the in-plane direction. So, the *ab initio* calculation takes into account these features, while the dispersion law generalizes the system. The IMFP is an input information for the MC calculation and in the simulations we assume homogeneous systems described by mean ELFs, that are those previously reported, without a preferential direction of interaction.

3.1.2 Calculated reflection electron energy loss spectra

Monte Carlo simulations were performed as previously described in section 2.1, by including as possible interactions the elastic and the inelastic scattering. To reproduce the spectra, 10^9 electron trajectories were computed. The beam direction was set orthogonal to the surface and the electron beam energy varies from 250 to 2000 eV. A Gaussian distribution of the initial energy was set (with σ = 0.4 eV). The elastic scattering was evaluated by applying the analytical formulation by Salvat [8] reported in Appendix A. The computation of input data concerning the inelastic scattering started from different descriptions of the dielectric behaviour of diamond and graphite was performed as reported before.

Diamond: The diamond target was considered with density equal to 3.515 g/cm^3 [4]. The energy band gap was calculated in our research group by density functional calculation [1] and set to 4.16 eV. The calculated spectra, by applying the different approaches, are reported and compared with experimental data in Fig. 3.4. All the spectra show a main σ plasmon peak

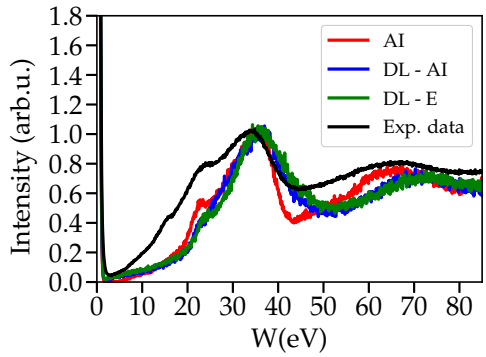

FIGURE 3.4: REELS of diamond: experimental data are reported in black, while simulated results using the three different dielectric models are sketched in red (AI), blue (DL-AI) and green (DL-E). Electron beam kinetic energy is 1000 eV. Data are normalized with respect to the height of σ plasmon peak [1].

at $\sim$ 35 eV. This can be brought back to the ELF main peak (Figs. 3.1 and 3.2) at the same energy. Moreover, the two-plasmon excitations at higher energy are present in both experimental and calculated spectrum. However, the spectrum obtained with the full AI approach shows a higher agreement with experimental data than the spectra obtained with the dispersion law (Eq. 2.17). Indeed, the latter spectra show blue-shifted peaks at higher energies.
By considering the full AI dielectric approach, different simulations were carried out by changing the value of the beam energy T. The results are compared to experimental data in Fig. 3.5. The agreement with experimental data is increased by the increase of the beam energy. This is due to the fact that our MC simulation does not take into account surface effects, that becomes less important for higher beam energies.

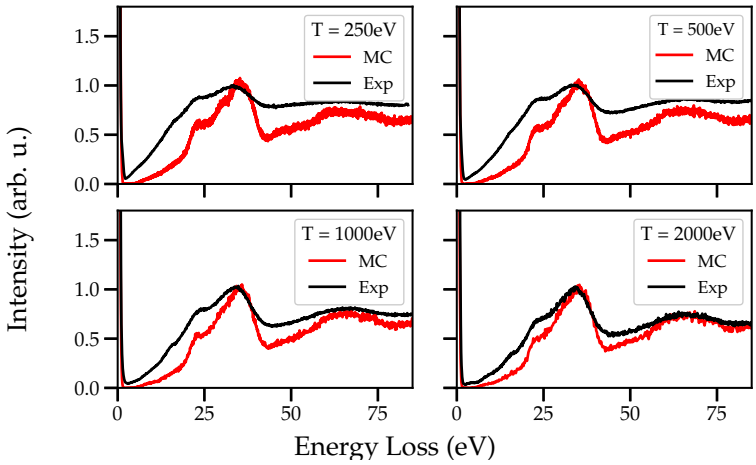

FIGURE 3.5: REELS of diamond obtained by calculating the ELF with the full AI approach (red line) at different momentum transfer compared to experimental data (black line) for several primary electron beam kinetic energies T. Data are normalized with respect to the height of σ plasmon peak [1].

From this comparison, it can be deduced that the **DL-AI** and **DL-E** approaches are less accurate in the description of electronic properties of semiconductors than the full **AI** approach, with the aim to reproduce REEL spectra. The reason can be found in the strongly inhomogeneous electron density and, thus, to the complexity of the dielectric response of this material that can not be considered as the response of a free electrons gas [1, 9].

Graphite: The graphite sample was considered with a density of 2.25 g/cm^3 [4]. Fig. 3.6 shows the REELS obtained with MC simulations (red line) and our experimental measurements (black line). The calculated spectra in Fig.3.6 show the two main plasmon peaks of graphite: the π peak (due to the collective excitation of valence electrons in the π band) and the $\pi + \sigma$ peak (due to collective excitation of all valence electrons) . These correspond to the two main peak of graphite ELF (Fig.s 3.1 and 3.2). The π peak is well defined in all the

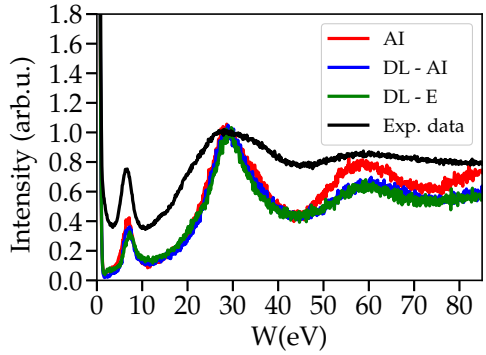

FIGURE 3.6: REEL spectra of graphite: experimental data are reported in black, while simulations using the 3 different models are sketched in red (AI), blue (DL-AI) and green (DL-E). Electron beam kinetic energy is 1000 eV. Data are normalized with respect to the height of the $\pi + \sigma$ plasmon peak [1].

spectra. It corresponds to the oscillations of electrons in the π band where the electrons can be considered almost de-localized. The hypothesis in which the dispersion law is developed (Eq. 2.17) considers a free electrons gas and in the case of graphite it is a correct assumption, indeed along graphite planes electron motion is characterized by a high mobility. And for this reason the spectra calculated with different dielectric approaches agree. The only discrepancy between the three calculated spectra is represented by the rise of a peak around 60 eV in the spectrum obtained with the full **AI** approach. The full **AI** approach guarantees a more accurate description of the ELF at different momenta. Other simulations were carried out, by using the **AI** approach, at different energies T of the beam and the results are compared to experimental data in Fig. 3.7. As in the case of diamond (Fig. 3.5) the agreement with experimental data is enhanced by the increase of the beam kinetic energy, as a result of the reduced influence of surface effects.

3.2 Anisotropy of the graphite structure in the simulation of electron transport

In this section calculated REEL spectra and secondary electron emission spectra (SEE) of graphite were calculated by presenting and testing a new model to take into account the anisotropic structure of graphite [10]. First of all the calculation of input data for MC simulation is explained in detail, then the MC model will be presented and the obtained spectra will be shown and commented.
This chapter is reproduced in part with permission from *M. Azzolini, T. Morresi, K. Abrams, R. Masters, N. Stehling, C. Rodenburg, N. M. Pugno, S. Taioli, M. Dapor, An Anisotropic Approach for Simulating Electron Transport in Layered Materials: Computational and Experimental Study of Highly*

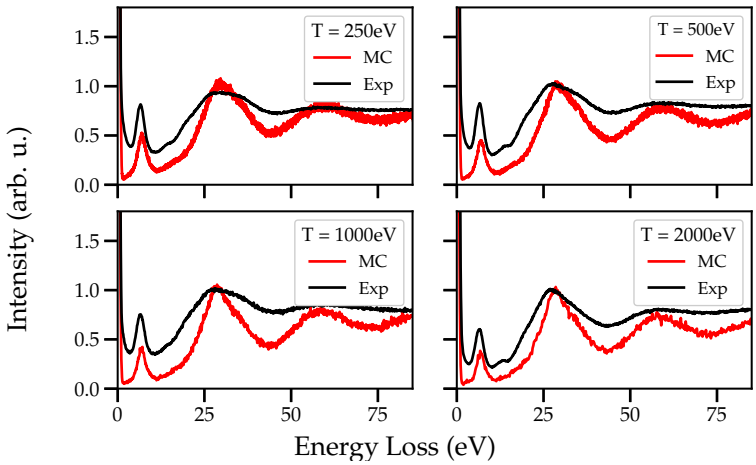

FIGURE 3.7: REEL spectra of graphite obtained by calculating the ELF with the full AI approach (red line) at different momentum transfer compared to experimental data (black line) at different primary electron beam kinetic energy T. Data are normalized with respect to the height of the $\pi + \sigma$ plasmon peak [1].

Oriented Pyrolitic Graphite, The Journal of Physical Chemistry C 122 (18), 10159-1016 (Copyright 2018 American Chemical Society).

3.2.1 Input data calculation

Elastic scattering The elastic scattering was considered by applying the Mott theory as indicated in Section 2.1.1. In this case the atomic potential was carefully calculated by using the ELK software program to solve the Dirac-Kohn-Sham equations for the carbon atom within the local-spin-density approximation (LSDA). The application of the Ganachaud-Mokrani correction (see section 2.1.1) is necessary since the total elastic scattering cross-section σ_{el} is equal to 28.3 Å^2 for the kinetic energy equal to $T = 10$ eV. This correspond to an elastic mean free path $\lambda_{el} = 0.31$ Å. The latter results to be one order of magnitude lower than the lattice parameters of graphite ($a = 2.46$ Å, $c = 6.71$ Å) . By choosing $\alpha = 0.003$ eV^{-2} the value of the elastic mean free path for $T = 10$ eV is $\lambda_{el} = 1.15$ Å. Fig. 3.8 shows the behaviour of σ_{el} (left panel) and λ_{el} (right panel) obtained with $\alpha = 0.003$ eV^{-2}, along with those calculated by using the bare Mott theory.

By applying this correction, the elastic scattering cross section is consistently diminished for low energy values. Furthermore, the introduction of this correction allows to achieve a good agreement between calculated and experimental secondary electron emission spectrum [10], as will shown later.

Inelastic scattering To take into account graphite anisotropy, the dielectric function and the ELF of graphite, were calculated in the optical limit ($\epsilon_{\vec{q}\to 0}$) , along the two main directions of the

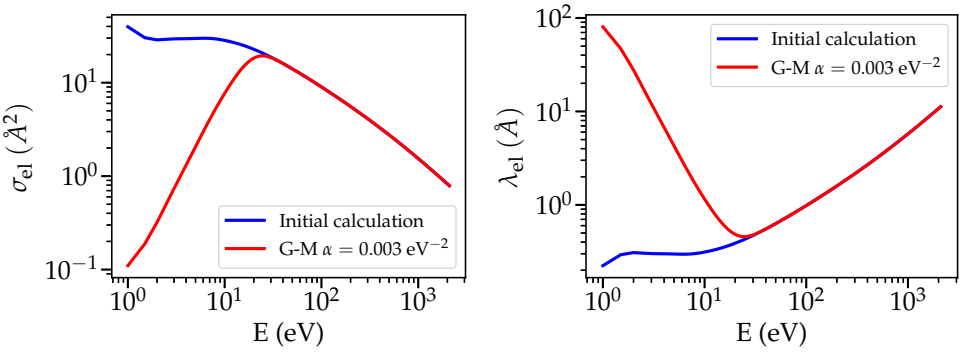

FIGURE 3.8: Total elastic scattering cross-section σ_{el} (left panel) and elastic mean free path λ_{el} (right panel) calculated from the bare Mott theory (blue line) and by using the correction proposed by Ganachaud and Mokrani (α = 0.003 1/eV^2) (red line) [10].

structure: along the direction normal to the layer (identified by the vector $\vec{c}$), which accounts for intra-planar interactions ($\vec{q}||\vec{c}$), and along that one perpendicular to $\vec{c}$ ($\vec{q}\perp\vec{c}$), which describes in-plane excitations. These dielectric functions will be denoted respectively as $\epsilon_{||}(q, W)$ and $\epsilon_{\perp}(q, W)$. Moreover, to distinguish them, the same notation is applied to the corresponding inelastic mean free paths $\lambda_{||}$ and $\lambda_{\perp}$. These dielectric functions were achieved by *ab initio* time-dependent density functional calculations performed in our research group [10]. Then the ELFs in the two directions, calculated in the optical limit, were fitted by using Drude–Lorentz functions (Eq. 2.16). Fig.3.9 compares final fit functions with *ab initio* ELF data, while the fitting parameters are reported in Tabs. 3.3 and 3.4. The number of oscillators was select in order to reach the best fit of *ab intio* data. Furthermore, the f-sum rule validity was taken into account [2]. It is worth noting that in this case the fit of the $ELF_{\perp}$ is achieved by using a higher number of oscillators than in the previous case (Tab. 3.2). In this way, an accurate reproduction of the *ab intio* result, without ignoring any possible excitation, is realized.

n	A_n (eV^2)	Γ_n (eV)	E_n (eV)
1	0.15	1.75	0.80
2	0.62	1.76	4.06
3	13.26	4.22	15.57
4	51.80	1.90	18.23
5	25.52	6.23	20.73
6	452.31	20.02	37.93
7	112.91	19.84	48.25

TABLE 3.3: D–L parameters ($\vec{q}||\vec{c}$ direction)

n	A_n (eV^2)	Γ_n (eV)	E_n (eV)
1	0.43	5.36	2.58
2	8.96	1.73	6.99
3	0.25	8.30	14.53
4	33.93	10.16	21.77
5	32.00	10.50	24.32
6	466.69	6.99	28.03
7	100.30	30.03	38.09

TABLE 3.4: D–L parameters ($\vec{q}\perp\vec{c}$ direction)

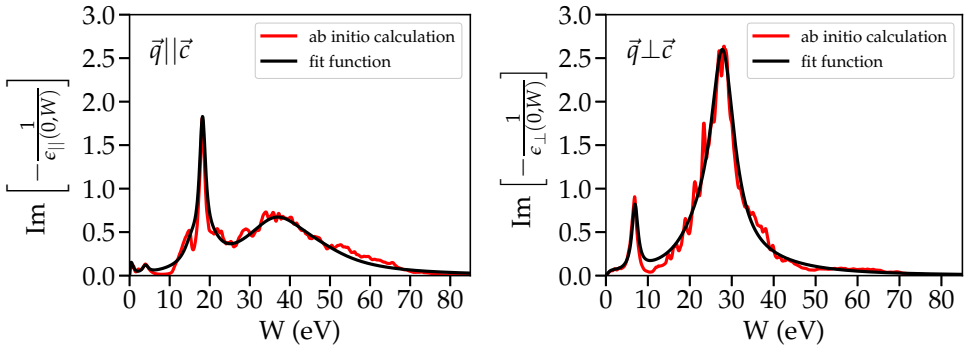

FIGURE 3.9: ELF functions along the two possible orthogonal directions of transferred momentum $\vec{q}$: *ab initio* calculations (red lines) are compared to the Drude–Lorentz best fits (black lines).

The extension of these ELFs for finite momenta, beyond the optical limit, i.e., was achieved by applying the quadratic dispersion law Eq. (2.17). Then, the inelastic mean free paths in the two directions were calculated by applying Eq. (2.19) and results are shown in the following Fig. 3.10:

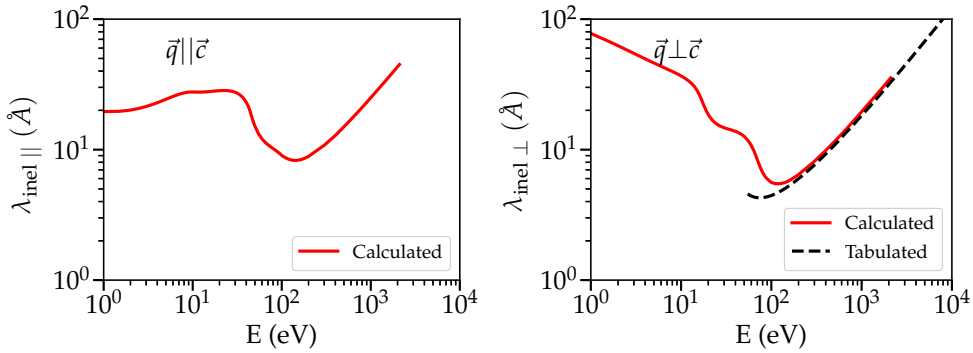

FIGURE 3.10: Inelastic mean free paths calculated along the two possible orthogonal directions of transferred momentum $\vec{q}$. In the case $\vec{q}\perp\vec{c}$ the calculated values are compared with the data by Tanuma et al. (dashed lines) [7] [10].

To consider the anisotropic structure of graphite, a linear combination of inelastic interaction along the two main directions was introduced to calculate the energy loss W and the inelastic mean free path λ_{inel} :

$$W = f\ \cos^2\theta\ W_{||} + [(1-f) + f\ \sin^2\theta]\ W_{\perp} \tag{3.1}$$

$$\lambda_{\text{inel}} = f\ \cos^2\theta\ \lambda_{||} + [(1-f) + f\ \sin^2\theta]\ \lambda_{\perp} \tag{3.2}$$

Here f is an *anisotropy parameter* in the range [0:1], and θ is the scattering angle $\vec{c}$ and $\vec{q}$. The role of the parameter f is to promote the movement of the electron along the plane($\vec{q}\perp\vec{c}$), given the fact that graphite shows a higher conductivity along this direction. The value of the parameters in the linear combination in Eqs. (3.2) and (3.1) are calculated at different values of f (Fig. 3.13), $f\cos^2\theta$, the coefficient of the $||$ component, is reported in red and $[(1-f) + f\sin^2\theta]$, the coefficient of the $\perp$ component, in blue.

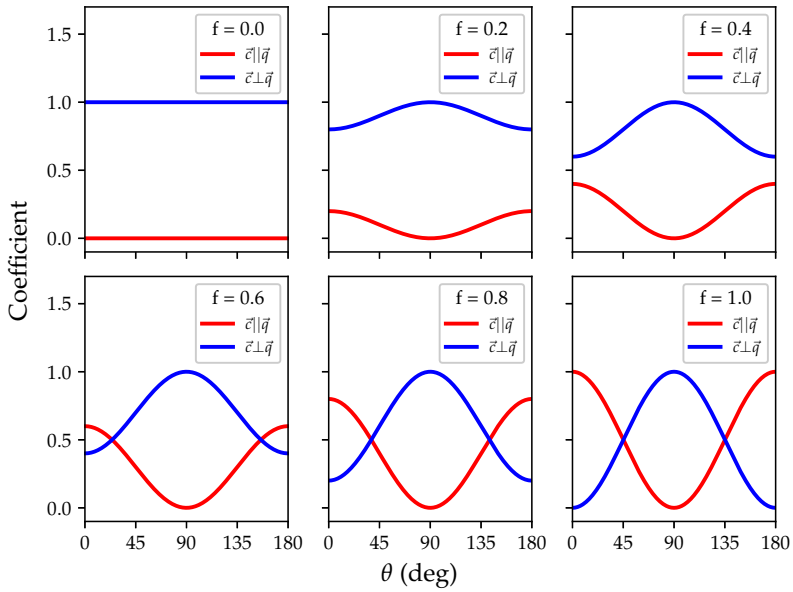

FIGURE 3.11: Coefficient of each component in Eqs.(3.2) and (3.1)

3.2.2 Anisotropic model and calculated emission spectra

Monte Carlo simulations were performed as reported in section 2.1 by considering only elastic and inelastic scattering. To simulate REEL spectra, 10^9 trajectories were calculated, while to reproduce secondary electron emission spectrum 10^6 primary electrons in the beam were considered. This reduction of electron number in the beam is determined by the fact that the number of secondary electrons generated and emitted is order of magnitude higher that the back-scattered electrons, and so to obtain statistically significant curves a lower number of beam electron is sufficient. Different simulations were performed by changing electrons beam energy and the f parameter value, in order to compare the calculated spectra with the experimental data.

The characteristic quantities of the sample required by the MC routine are: the atomic number ($Z = 6$), the atomic mass ($A = 12.011$ amu) [11], the density ($d = 2.25$ g/cm^3) [4], the electronic band gap E_g (0.0 eV), and the work function ($WF = 4.6$ eV) [12].
The total mean free path (λ), which characterizes the electron path within the target material is defined as:

$$\frac{1}{\lambda} = \frac{1}{\lambda_{\text{el}}} + \frac{1}{\lambda_{\text{inel}}} \tag{3.3}$$

where λ_{el} is the elastic mean free path. The probabilities of the elastic and inelastic events can be evaluated, for any fixed value of kinetic energy and angle, as:

$$\text{p}_{\text{el}} = \frac{\lambda}{\lambda_{\text{el}}} \qquad \text{p}_{\text{inel}} = \frac{\lambda}{\lambda_{\text{inel}}} \tag{3.4}$$

The decision on the type of collision that the electrons undergo is made by generating another random number r. Whether this number is lower than p_{el} the interaction will be elastic, otherwise it will be inelastic. In Fig. 6.9 we report the elastic and inelastic collision probabilities as a function of the relevant variables θ and T.

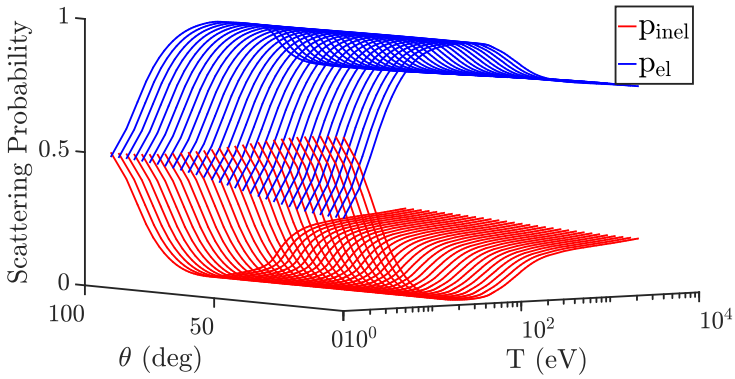

FIGURE 3.12: Collision probabilities as a function of the electron kinetic energy (T) and of the scattering angle (θ) between the transferred momentum $\vec{q}$ and the vector $\vec{c}$ normal to the surface [10].

REELS Simulations were performed in order to compare calculated REEL spectra with experimental data [1]. The incidence beam angle was set to 30° with respect to the normal to the surface, in order to reproduce the experimental conditions. First, the investigation on the role of the f parameter was carried out by calculating spectra at 1500 eV by changing its value in Eqs. (3.2) and (3.1). The comparison is visible in Fig. 3.13.

The rise of a shoulder around 20 eV, which corresponds to the main oscillation of the ELF along the $\vec{q}||\vec{c}$ direction (see Fig. 3.9, left panel), is present as a consequence of the increase of the value of f. The higher agreement between experimental and calculated REEL spectra

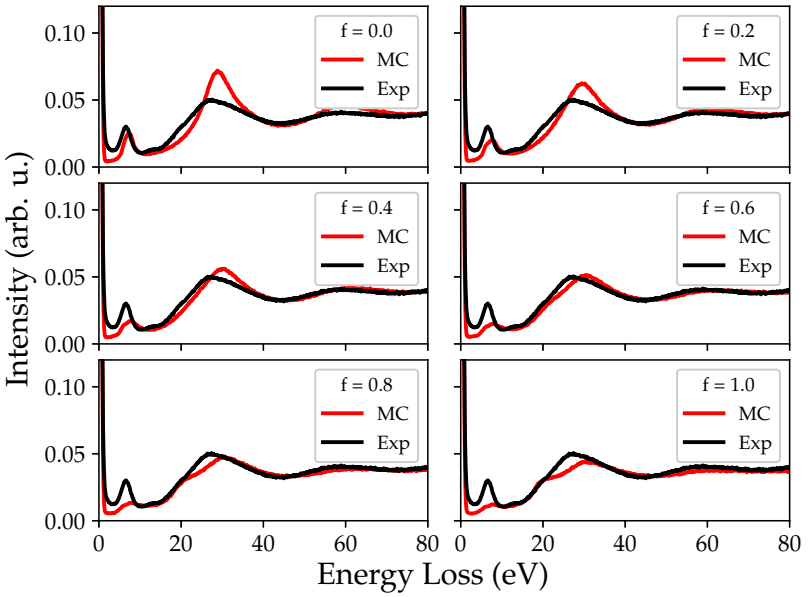

FIGURE 3.13: REELs of graphite for different values of the f parameter (red lines). The kinetic energy of the primary beam is set to 1500 eV. MC calculations are compared with our experimental data (black lines) [1]. The spectra are normalized at a common area of the elastic peak [10].

is obtained with the anisotropy parameter f equal to 0.6. It is also confirmed by the χ^2 test, performed in an energy loss range [-2:80] eV (Fig. 3.14). The value of $f = 0.6$ can be visualized by considering a beam impinging normally on the target surface (orthogonal to graphite layers), the travelling electron is slowed down by losing energy in interactions that are for a 40% given from in-plane direction collisions ($\vec{q} \perp \vec{c}$) and for the other 60% given from inelastic interactions with transferred momentum along the $\vec{q} || \vec{c}$ direction. In the simulation, each directional change of the electron trajectory is taken into account and the linear combinations of Eqs. (3.2) and (3.1) are carefully calculated at each MC step according to the actual θ angle of the electron trajectory.

It is worth noting, that this good agreement is reached by normalizing the spectra at a common area of the elastic peak, and therefore this anisotropic model reproduce quantitatively the experimental spectra, by maintaining the correct ratio between the two main peaks. The best anisotropic parameter ($f = 0.6$) was maintained fixed and MC simulations were realized by changing the value of the primary beam kinetic energy. The results are reported and compared with experimental data in Fig. 3.15.

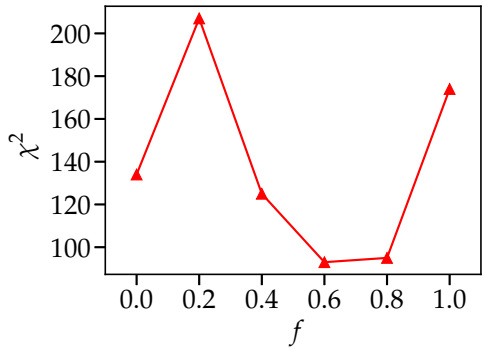

FIGURE 3.14: χ^2-test carried out by considering the experimental and calculated data normalized at a common area of the elastic peak in the energy loss range [-2:80] eV for different values of the parameter f [10].

As in previous cases (Fig. 3.5 and 3.7) the agreement between calculated and experimental data improves as the energy increases. Indeed, the surface plasmon contribution, which is not taken into account in the MC calculation, diminishes its contribution at higher beam kinetic energy.

Secondary Electron Emission spectrum Secondary electron emission spectrum of graphite was calculated by considering the beam kinetic energy equal to 1000 eV and by maintaining the direction normal to the target surface, according to the experimental conditions [10]. The obtained spectrum is reported and compared with the experimental one in Fig. 3.16. The experiemental measurement was acquired by the experimental group at the University of Sheffield (UK).

The calculated spectrum has been shifted by 0.7 eV along the positive axis direction, in order to align the emission peak, showing that the shapes of the two peak are quite similar.

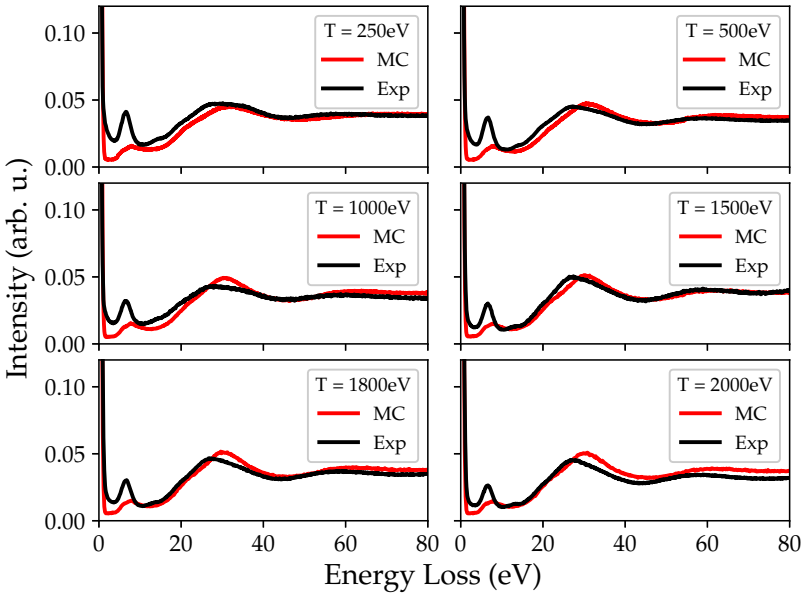

FIGURE 3.15: REELs of graphite for several primary beam kinetic energies. Red lines show simulated spectra, while black curves report our experimental data [1]. The results are normalized at a common area of the elastic peak [10].

3.3 Conclusions

In this section the most stable carbon-based materials, diamond and graphite, were considered for studying the electron transport phenomena. First of all, different models on the evaluation of the dielectric response of these materials were tested. Their accuracy was assessed by comparing results about REEL spectra with experimental data. It emerges from this analysis that the *ab initio* evaluation of dielectric properties of diamond and graphite ensures an increase in the accuracy of the method. Indeed, the *ab initio* procedure overcomes the assumption of the free electron gas. The free electron gas approximation is satisfied for metals samples, while in semiconductors and insulators where the electron density is not homogeneous this hypothesis is no longer properly valid. The *ab initio* calculation of dielectric properties of graphite was further exploited, by obtaining the energy loss function in the two main directions of the target crystalline structure of graphite. Starting from this directional information, a new MC model was developed to consider the anisotropic structure in inelastic interactions, by evaluating the inelastic mean free path and the energy loss as linear combinations of these quantities along the two main directions. The results obtained further enhance the accuracy of the method emphasizing the fact that the conductive properties of the sample, in particular if they are not

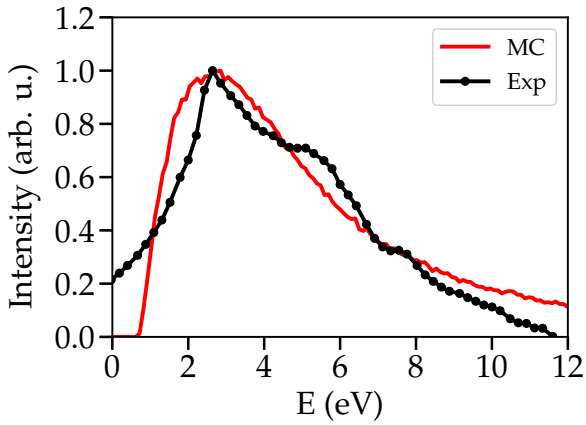

FIGURE 3.16: Secondary electron spectra of graphite. Black line represents experimental data, while in red we report the theoretical spectrum. The data are normalized to a common height of the secondary electron emission peak [10].

homogeneous, significantly affect the electron transport within it.

Bibliography

[1] M. Azzolini, T. Morresi, G. Garberoglio, L. Calliari, N. M. Pugno, S. Taioli, M. Dapor, Monte carlo simulations of measured electron energy-loss spectra of diamond and graphite: Role of dielectric-response models, Carbon 118 (2017) 299.

[2] E. Shiles, T. Sasaki, M. Inokuti, D. Y. Smith, Self-consistency and sum-rule tests in the Kramers – Kronig analysis of optical data: Applications to aluminum, Phys. Rev. B 22 (1980) 1612–1628.

[3] I. Abril, R. Garcia-Molina, C. D. Denton, F. J. Pérez-Pérez, N. Arista, Dielectric description of wakes and stopping powers in solids, Physical Review A 58 (1) (1998) 357.

[4] R. Garcia-Molina, I. Abril, D. Denton, S. Heredia-Avalos, Allotropic effects on the energy loss of swift H^+ and He^+ ion beams through thin foils, Nucl. Instrum. Methods Phys. Res., Sect. B 249 (1–2) (2006) 6 – 12.

[5] J. Daniels, C. V. Festenberg, H. Raether, K. Zeppenfeld, Optical constants of solids by electron spectroscopy, in: Springer Tracts in Modern Physics, Volume 54, Springer, 1970, pp. 77–135.

[6] H. Raether, Excitation of plasmons and interband transitions by electrons, Vol. 88, Springer, 1980.

[7] S. Tanuma, C. J. Powell, D. R. Penn, Calculations of electron inelastic mean free paths. IX. Data for 41 elemental solids over the 50 eV to 30 keV range, Surface and Interface Analysis 43 (3) (2011) 689–713.

[8] F. Salvat, J. Martinez, R. Mayol, J. Parellada, Analytical Dirac-Hartree-Fock-Slater screening function for atoms (Z=1–92), Phys. Rev. A 36 (1987) 467–474.

[9] H. Nikjoo, D. Emfietzoglou, T. Liamsuwan, R. Taleei, D. Liljequist, S. Uehara, Radiation track, DNA damage and response: a review, Rep. Prog. in Phys. 79 (2016) 116601.

[10] M. Azzolini, T. Morresi, K. Abrams, R. Masters, N. Stehling, C. Rodenburg, N. Pugno, S. Taioli, M. Dapor, Anisotropic approach for simulating electron transport in layered materials: Computational and experimental study of highly oriented pyrolitic graphite, The Journal of Physical Chemistry C 122 (18) (2018) 10159–10166.

[11] Royal Society of Chemistry. Periodic Table: Carbon, `http://www.rsc.org/periodic-table/element/6/carbon`, (Accessed March 10, 2016).

[12] Y. Zhou, D. S. Fox, P. Maguire, R. O'Connell, R. Masters, C. Rodenburg, H. Wu, M. Dapor, Y. Chen, H. Zhang, Quantitative secondary electron imaging for work function extraction at atomic level and layer identification of graphene, Sci. Rep. 6 (2016) 21045.

Chapter 4

Carbon based materials II: peeling of a graphene layer from a bulk of graphite

In this chapter the peeling of a graphene layer from a bulk of graphite was modeled and simulated by means of Molecular Dynamics method. To quantitatively understand the phenomenon, initially mechanical tests were carried out on free-standing layers of graphene. To evaluate the energy adhesion between two attached layers of graphene, dedicated simulations were done. Finally, the simulations of the complete peeling process were realized and here the results and the application of the classical theory by Kendall are presented and discussed. In particular, the Molecular Dynamic simulation of tensile test of a graphene layer, measurement of adhesion energy and the peeling of a graphene layer from a bulk of graphite were realized by using the software LAMMPS [1]. The atomic structures were visualized by using the OVITO package [2] and the atomic interaction was modeled with the AIREBO potential [3] with a long range cutoff of 10.2 Å.

4.1 Mechanical test on a graphene layer

Molecular dynamic simulations were realized to test the mechanical behaviour of a free standing graphene layer to calculate the value of the Young's Modulus, the strength and the fracture strain for different deformation conditions.
The sample considered is a free standing layer of graphene, composed by 960 atoms, with a square shape of side dimension of 50 Å. This structure was constructed by developing a python code that generates atoms coordinates. The x-direction corresponds to the zig-zag configuration, the y-direction to the armchair configuration (Fig. 5.1). The thickness of the graphene layer is equal to 3.4 . The simulation cell was created with these dimensions in the three directions (L_x, L_y, L_z) = (49.2, 51.2, 30.0) Å and periodic boundary conditions were set along the three directions. After the structure energy and force minimization, in order to thermalize the sample at room temperature, an isothermal-isobaric (NPT) ensemble was set. The initial velocities were assigned at a temperature equal to 10 K. During the integration in the NPT ensemble,

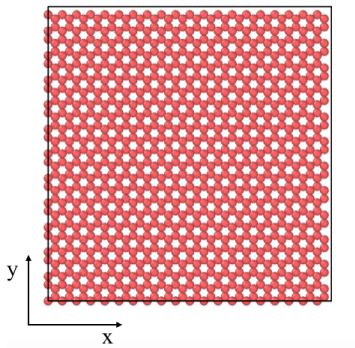

FIGURE 4.1: Free standing graphene layer considered in molecular dynamics simulations, the black box represent the simulation cell.

the temperature is increased reaching the value of 300 K and maintaining the pressure in x and y directions equal to zero. The time-step was set equal to 0.001 ps and this part of the thermalization process lasted for 50 ps. Then the system was kept at 300 K in a canonical ensemble for 100 ps to asses a solid thermalization. In the following charts (Fig. 4.2) the temperature and the kinetic energy of the system during the thermalization process are reported. The values are obtained by averaging the observables in an interval of 0.2 ps and they were sampled every 0.2 ps.

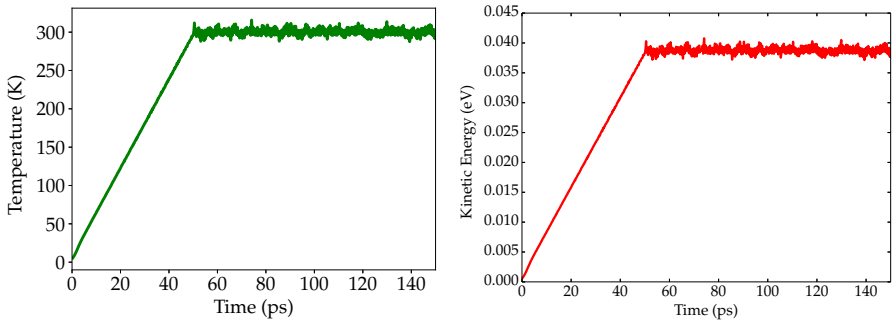

FIGURE 4.2: Temperature and kinetic energy of the system during the thermalization process.

The temperature was calculated by averaging the values in the interval between 50 and 150 ps and it results to be 300 K, in agreement with the desired temperature for the tensile test. The deformation was realized in an NPT ensemble, at the constant temperature of 300 K and maintaining zero the pressure in the direction without applied deformation. A constant deformation velocity of the box length, actually an engineering strain rate, was imposed and

it was set at different values between 0.1 Å/ps and 10.0 Å/ps. To stretch along the armchair direction the deformation was applied in the y-direction while to stretch along the zigzag direction a constant velocity was applied in the x-direction. After the rupture, structures appear as reported in Fig. 4.3.

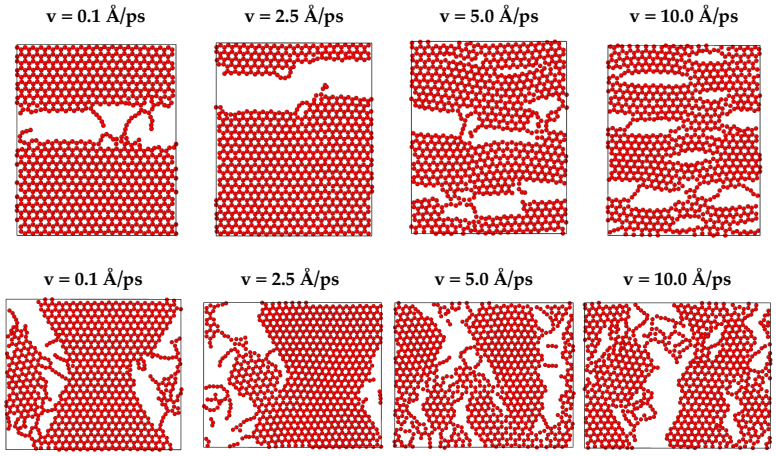

FIGURE 4.3: Free standing graphene layers after deformations obtained with different velocities: in the upper panel armchair deformations, in the bottom panel zigzag deformations.

The stress and strain values are sampled, during simulations carried out with different velocities, in order to obtain data set with the same length. In Fig.4.4 stress - strain curves are reported, for different values of velocity deformation.

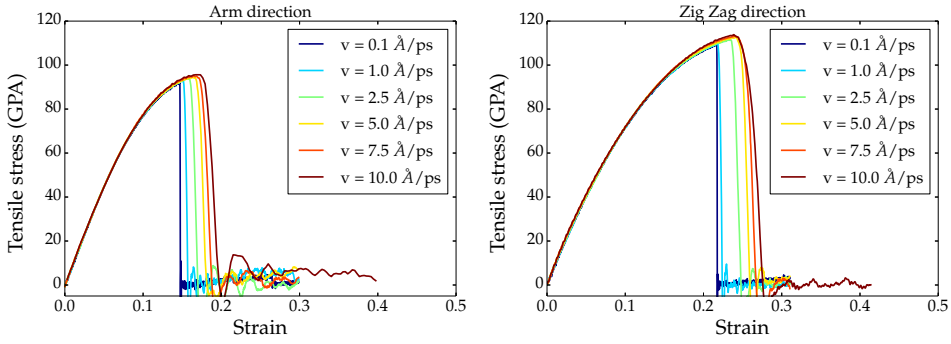

FIGURE 4.4: Stress strain curve of the graphene layer subjected to traction

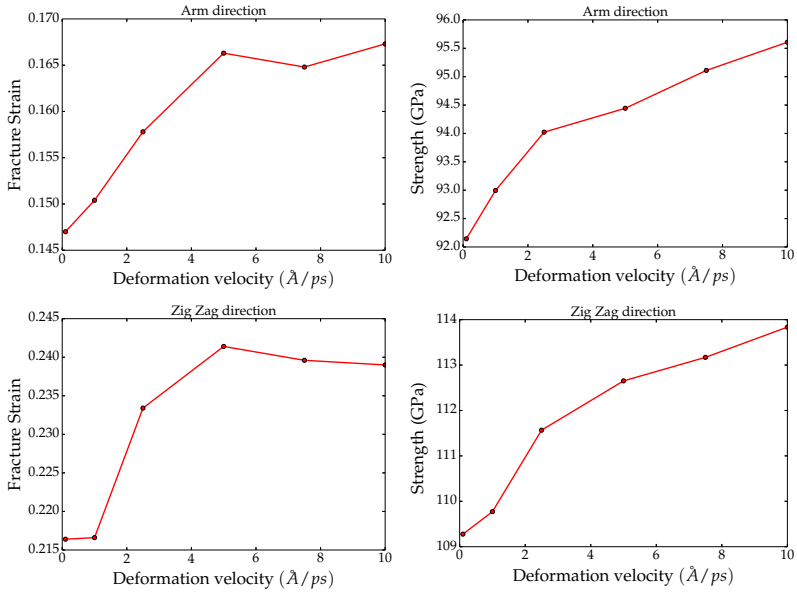

FIGURE 4.5: Values of fracture and rupture strength as a function of the applied deformation velocity

The elastic modulus was obtained by a linear fit of the first part of the stress-strain curve. The strength was determined by choosing the highest value of the stress-strain curve and the correspondent value of fracture results to be the fracture strain. In Tab. 4.1 the values of strength (σ), fracture strain (ϵ_F) and Young's modulus (Y) are reported for different velocities.

From the previous figures (Fig. 4.4 and 4.5) it is clear that the Young Modulus remains constant by considering different situations of deformation, and it is in agreement with those reported in Ref.[4], while the strength and the fracture strain tends to increase for higher deformation velocity. This can be interpreted as a tendency of the material to become more resistant to the fracture if the deformation is faster.

4.2 Measure of the adhesion energy

The adhesion energy is the energy that has to be transferred to the system in order to detach two layers. In the case of the peeling process it has an important role. This quantity can be measured by considering the system in two different configurations: with the two layers attached and with the two layers detached. Indeed, the adhesion energy R, per unit of surface, can be defined as:

$$R = [U(a) + U(b) - U(a/b)]/S \tag{4.1}$$

where $U(a) + U(b)$ is the total energy of the detached system and $U(a/b)$ the total energy in presence of a common interface with S the area of the interface.

Armchair

Velocity (Å/ps)	Strength (GPa)	Fracture strain	Young modulus (TPa)
0.1	92.1	0.147	0.9
1.0	93.0	0.150	0.9
2.5	94.2	0.158	0.9
5.0	94.4	0.166	0.9
7.5	95.1	0.164	0.9
10.0	95.6	0.167	0.9

Zigzag

Velocity (Å/ps)	Strength (GPa)	Fracture strain	Young modulus (TPa)
0.1	109.3	0.216	0.8
1.0	109.7	0.216	0.8
2.5	111.6	0.233	0.8
5.0	112.7	0.241	0.8
7.5	113.2	0.239	0.8
10.0	113.8	0.239	0.8

TABLE 4.1: Values of strength, fracture strain and Young's modulus (E) for different applyied deformation velocities.

To measure the adhesion energy between two graphene layers, two different molecular dynamic simulations were realized.
The considered system was composed of two layers of graphene, in the AB configuration, with a square shape of the side length of 50 Å. In the "*attached case*" layers were separated by 3.4 Å, in the "*detached case*" they were separated by 13.4 Å (Fig. 4.6).

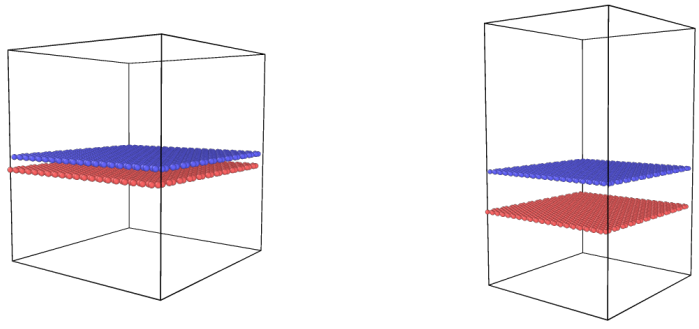

FIGURE 4.6: Graphene layers considered to calculate the adhesion energy, on the left the *attached configuration* and on the right the *divided configuration*.

The total number of atoms in the system was equal to 1920. The timestep was chosen equal to 0.001 ps and periodic boundary conditions were set around the cell.
In the two different configurations, the energy and forces of the system were minimized at 0 K . Then random velocities at 300 K were assigned to each atom and for 10 ps the system was kept at 300 K in a canonical ensemble. After the minimization at 0 K and after the thermalization at 300 K, the total energies of the two systems were measured. The values of adhesion energy R, at different temperatures, were computed as reported in Eq. 4.1, obtaining this values:

$$R(T = 0\ K) = 0.281\ \mathrm{J/m^2}$$

$$R(T = 300\ K) = 0.280\ \mathrm{J/m^2}$$

These results are in agreement with the experimental value and the DFT result, respectively $0.221 \pm 0.011\ \mathrm{J/m^2}$ and $0.235\ \mathrm{J/m^2}$ at $T = 77$K, reported by Wang et al. [5].

4.3 Simulation of the peeling of a graphene layer from a bulk of graphite

The simulation of the peeling of a graphene layer from a bulk of graphite was carried out by considering two different structures: one with the peeling direction along the armchair direction and the other along the zigzag direction. The structures are composed by 16 layers in the AB stack configuration. The width was set equal to 15 Å and the length to 600 Å. The total number of atoms in the armchair direction structure is 53763 and in the zigzag case is equal to 46632. The deeper layer and the sides were maintained fixed with no force applied (indicated in red in Fig. 4.7), in order to simulate a bulk structure.

In the width direction (x for armchair, y for zigzag) periodic conditions were set. The generation of atoms coordinates of these structures was realized by developing an in-house Python code. First of all, the samples were subjected to energy and force minimization in order to arrange the system in the equilibrium configuration. After the minimization process, the equilibration at room temperature was achieved by initially generating random velocities at 600 K. Then systems were kept for 20 ps in an NVE ensemble with a Langevin thermostat at 300 K and by setting the timestep to 0.001 ps. To ensure the proper thermalization, the systems were later subjected to an NPT ensemble, maintaining the temperature at 300 K and by asking for zero pressure in the direction of the width. This last step of thermalization lasts for 40 ps. In Figure 4.8 the temperature trend is reported for the two systems, and we see that its value converges to the required temperature of 300 K.

A constant velocity was applied in the z direction to the atoms of the free side of the upper layer, indicated in orange in the previous figure 4.7. For these atoms, the forces in the x and y directions were set to zero to maintain this coordinates fixed during the simulation. The system was kept at 300 K in a canonical ensemble.
Integration was stopped when the top layer was completely detached (Fig.4.9). The applied velocity was varied in the interval between 0.1 Å/ps and 10.0 Å/ps. Figs. 4.10 and 4.11 report snapshots zoomed on the peeling zone during the simulations at different applied velocities.

The color code of atoms evidences the atoms vertical displacement. The pictures show that for the intermediate velocity of 5 Å/ps there is a substantial vertical displacement of the

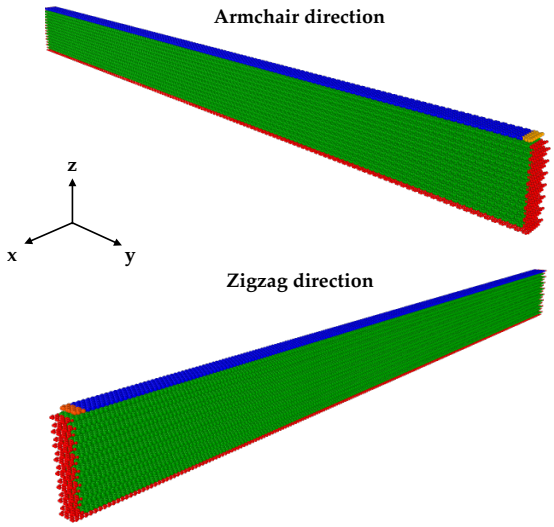

FIGURE 4.7: Structures considered in MD simulation of the peeling of a graphene layer. In red fixed atoms, in blue the layer to be peeled off, in orange the atoms with applied velocity.

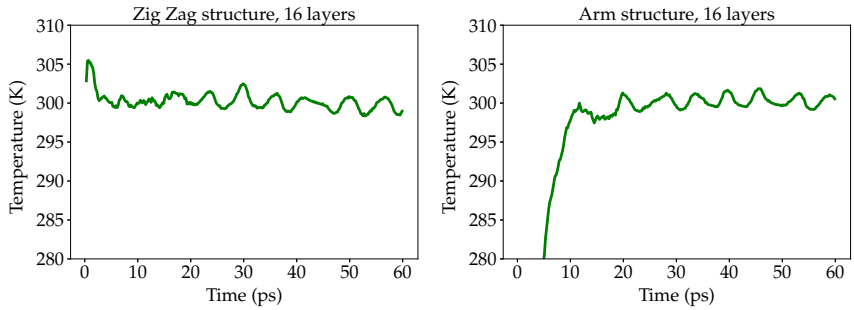

FIGURE 4.8: Temperature of the two systems, as a function of time, during the thermalization stages.

substrate layers. For the other velocities, the displacement is not so intense and dissolves with the continuation of the process. Details about the vertical displacement of atoms are given by the following pictures (Fig. 4.12), in which the percentage of substrate atoms that have undergone a vertical translation higher than 3.4 Å is reported as a function of the z position of the atoms to which the constant velocity is applied.

For velocities lower or equal to 2.5 Å/ps and higher than 8 Å/ps the substrate can be considered not influenced by the peeling process.

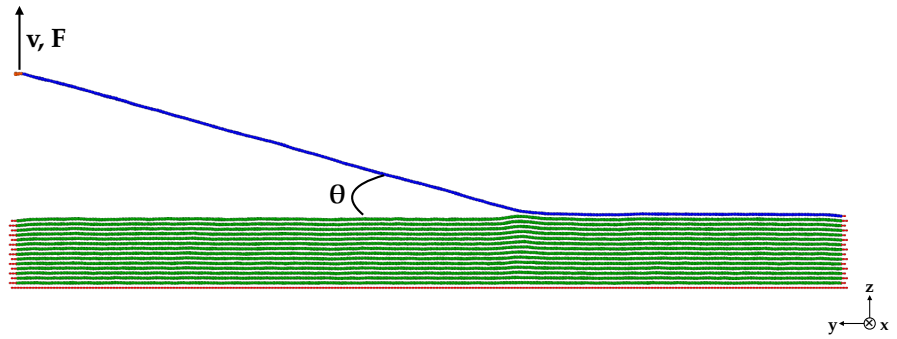

FIGURE 4.9: Peeling simulation on an Armchair structure.

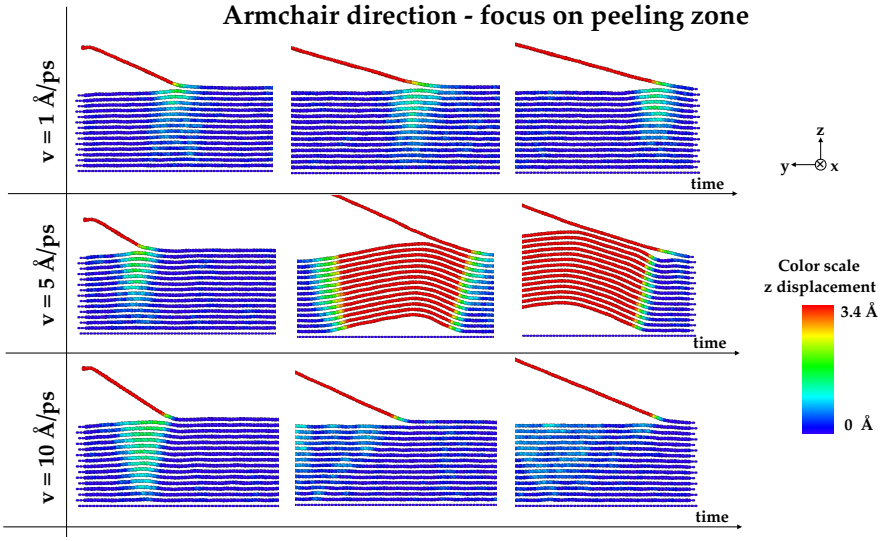

FIGURE 4.10: Snapshot of peeling zone during the MD simulation for the Armchair structure with different applied constant velocities. The atoms colormap reports the z displacement.

To quantitatively analyze this process the peeling angles and the force F were calculated for each system and velocity during the entire simulation. In particular, the force F is the sum of forces along the z direction of those atoms to which the constant velocity was applied. The Kendall theory [6] states that the force f, along the peeling direction, required to peel off an

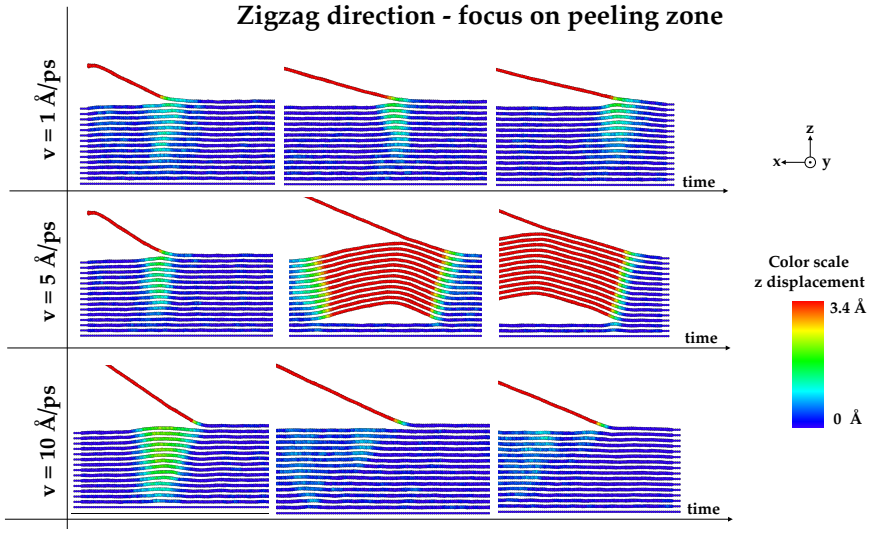

FIGURE 4.11: Snapshot of peeling zone during the MD simulation for the Armchair structure with different applied constant velocities. The atoms colormap reports the z displacement.

elastic medium from a rigid substrate is equal to:

$$f = b\,t\,Y\left[\cos(\theta) - 1 + \sqrt{(1-\cos(\theta))^2 + \frac{2R}{tY}}\right] \tag{4.2}$$

where b and t are respectively the thickness and the width of the layer, R the adhesion energy per unit surface, Y the Young modulus and θ the peeling angle (Fig. 4.7). The force f can be computed from the calculated force F value as:

$$f = F/\sin(\theta) \tag{4.3}$$

The Kendall equation can be rewritten in terms of the measured F as:

$$F = \sin(\theta)\,b\,t\,Y\left[\cos(\theta) - 1 + \sqrt{(1-\cos(\theta))^2 + \frac{2R}{tY}}\right] \tag{4.4}$$

Atom trajectories were elaborated in order to obtain the value of the peeling angle (θ) as a function of the z position of the atoms with applied constant velocity.
The applied peeling velocity which ensures a quasi-static deformation of the system is the lowest one, equal to 0.1 Å/ps. The peeling angle is reported as a function of the z displacement of the atoms with applied velocity.

Looking at the peeling angle behavior, an initial spike indicates the initial detachment of

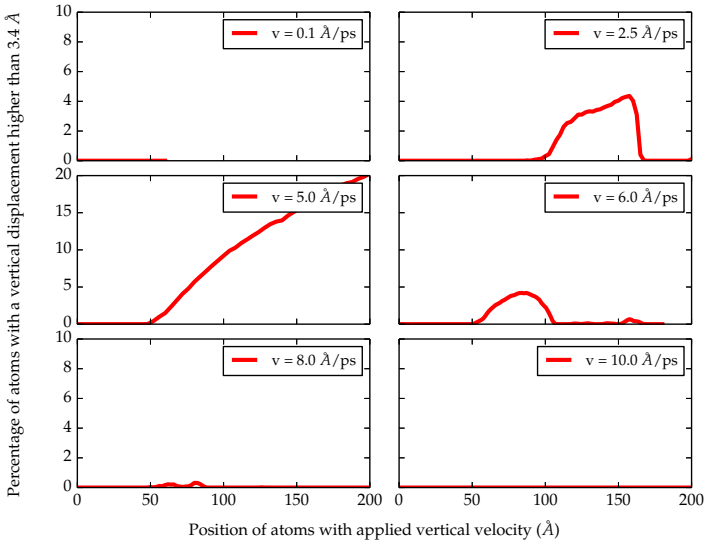

FIGURE 4.12: Percentage of atoms of the substrate that have undergone a z displacement higher than 3.4 Å as a function of the z position of the atoms with applied velocity for the armchair structure.

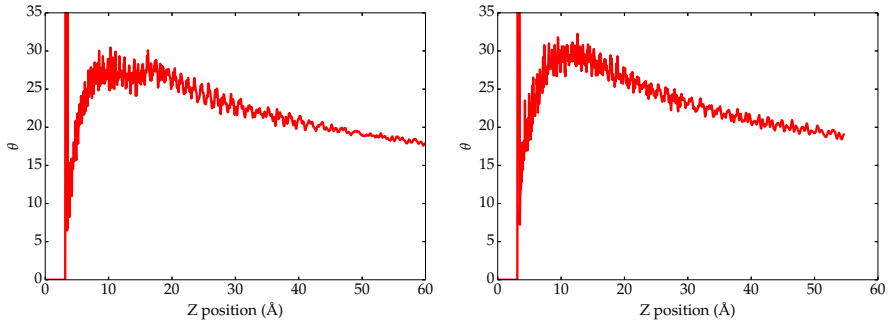

FIGURE 4.13: Angle as a function of z position of those atoms to which the constant velocity is applied. Results for the armchair structure on the left and for the zigzag structure on the right.

the layer, for higher detachments the angle, tends to stabilize. Also the force was computed at fixed integration steps during the different simulations. For those realized with a peeling velocity equal to 0.1 Å/ps, the values of the peeling force F, as a function of the peeling angle

and as a function of z position of the atoms with the applied velocity, are reported in figure 4.14.

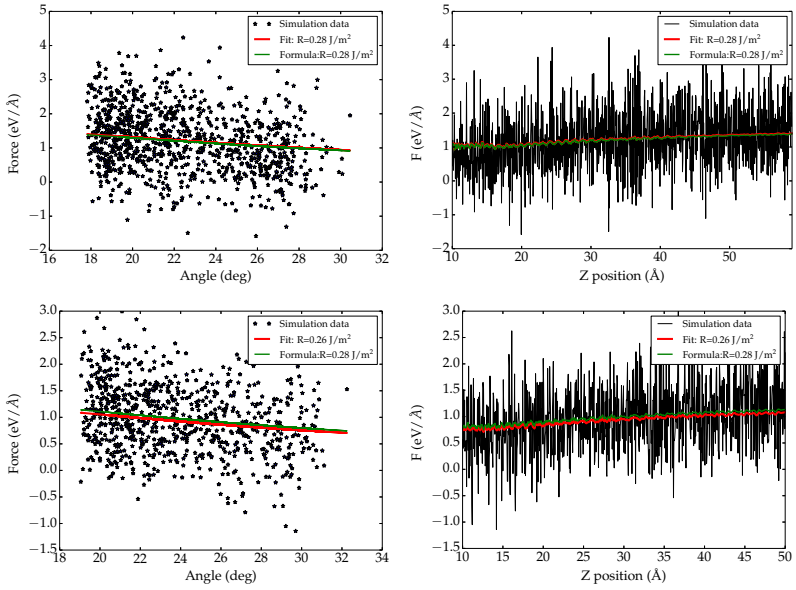

FIGURE 4.14: Force suffered in the z direction by the atoms with applied velocity: on the left as a function of the peeling angle and on the right as a function of the atoms z position. Upper panels show results for armchair peeling structure and the lower panels for the zigzag configuration. The data were recorded by setting the peeling velocity equal to 0.1 Å/ps. In red the curves predicted by the Kendall theory by using the fitted value of R, in green by using the value of R calculated from a dedicated MD simulation (see section 4.2).

By considering the force value as a function of the peeling angle, the Kendall theory can be applied to calculate the adhesion energy. This was realized by fitting the data with Eq. 4.4 by maintaining the adhesion energy R as a free parameter. The employed values of the Young Modulus Y is the one calculated in the previous section 4.1. For the quasi static simulation (at a peeling velocity equal to 0.1 Å/ps) the obtained values of the adhesion energy are for the armchair structure equal to 0.284 J/m^2 and for the zigzag structure equal to 0.276 J/m^2, which are both in agreement with the value calculated before (section 4.2). The obtained fit function is drown in red in Figs. 4.14 and in green is shown the curve obtained with the value of R determined from the previous dedicated MD simulations. These fitting procedure was implemented for all the data sets concerning the results of simulations realized at different velocities and the obtained values of adhesion energy are displayed in the following Fig. 4.12.

From the previous figure it is clear that the agreement between the previous calculated and the effective value of R (assessed via fitting procedure) is achieved only for the lowest applied velocity. Indeed the effective R tends to increase with the raise of the velocity. Around 5 Å/ps

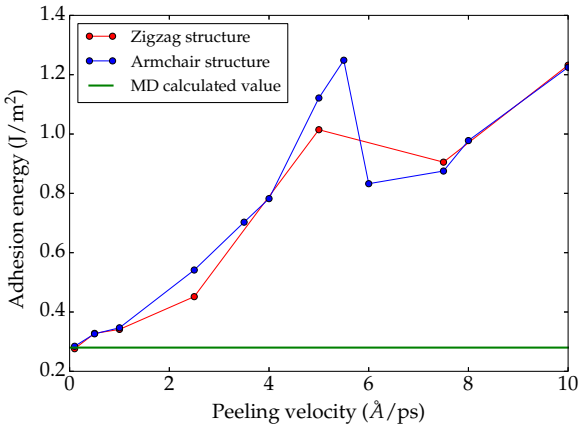

FIGURE 4.15: Values of effective adhesion energy, for different applied velocities, obtained from fitting procedure and compared to the value calculated with static MD simulation.

a local maximum is reached. This corresponds to an increase of the force. In fact for this velocity there was a collective movement of the substrate in the z direction. By further increasing the applied velocity, the effective adhesion energy diminishes and then increases again. The decrease of effective energy corresponds to a lower perturbation of the substrate (Fig. 4.12). However, even if the adhesion energy further increases, the substrate is no longer affected by the peeling of the upper layer.
Taking into account the above analysis leads to the conclusion that, if the peeling of the upper layer occurs with low velocity, the system is subjected to a quasi static perturbation without involving the substrate. By increasing the velocity, the detachment action competes with the adhesion between the layers, producing the temporary translation of the substrate in the vertical direction. At higher velocity, the detachment of the upper layer occurs almost instantaneously and, given the inertia of the substrate, it remains unperturbed.

Deeper structure

From the previous set of simulations, it was found that the most substantial influence on the substrate occurs for a peeling velocity of 5 Å/ps. To investigate how long in depth is the substrate deformation due to the peeling of the first layer a structure (armchair direction) with the same geometry in the x-y plane (15 Å in width and 600Å length) and with 26 total layer is generated. The system is composed of 83976 atoms and was subjected to the same thermalization procedure than the previous case.

Snapshots of the structure during the simulations are shown in the figure 4.16.

In this case the deformation undergone by the substrate is more complex than before. Proceeding with the peeling, a further delamination between substrate layer occurs. In the end,

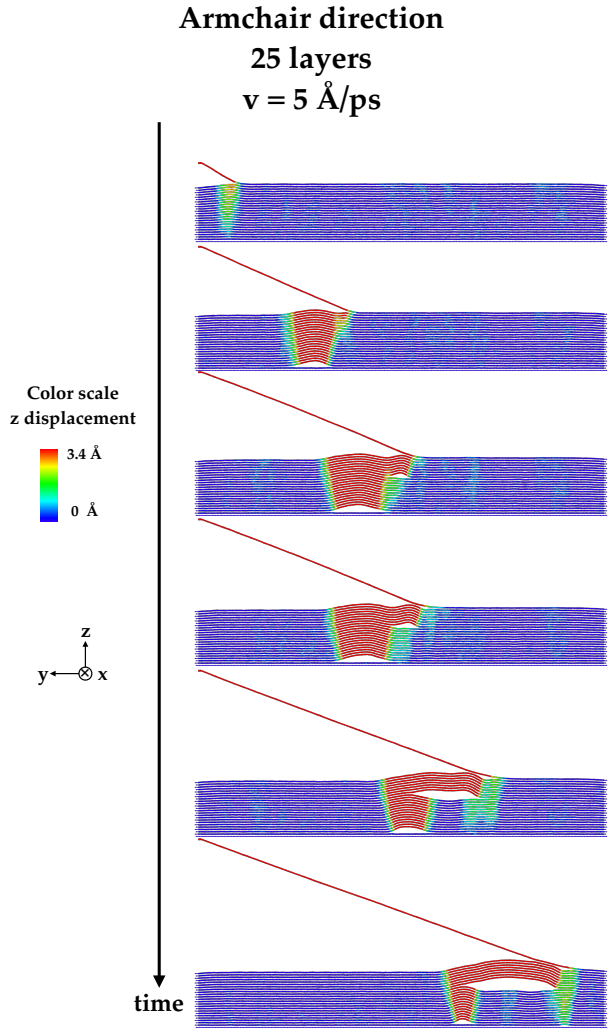

FIGURE 4.16: Snapshots of the armchair structure, composed by 25 layers, during the MD simulation of the peeling of the upper layer at a velocity of 5.0 Å/ps.

the peeling position exceeds the deformation of the substrate by reaching the other side of the sample first.

4.4 Conclusions

Molecular dynamic simulations were realized in order to investigate the peeling of the graphene layer from a bulk of graphite. As preliminary study, a graphene layer was subjected to tensile test by changing the values of the deformation velocity. It was found that the graphene reaches higher fracture stress at higher deformation velocity. As preliminary study for the peeling process, the energy adhesion between two graphene layer was determined from a dedicated molecular dynamic simulation. After that, the simulation of a graphene layer from a bulk of graphite was realized for different applied peeling velocities. The Kendall theory results to be valid only in the case of the quasi static deformation obtained with the lowest velocity (v = 0.1 Å/ps). For intermediate applied velocity the substrate is consistently affected by the delamination of the upper layer with their translation in the vertical direction. For higher velocity the substrate is basically unperturbed, due to the inertia of it to the fast impulse given from the peeled upper layer.

Bibliography

[1] S. Plimpton, Fast parallel algorithms for short-range molecular dynamics, Journal of computational physics 117 (1) (1995) 1–19.

[2] A. Stukowski, Visualization and analysis of atomistic simulation data with ovito–the open visualization tool, Modelling and Simulation in Materials Science and Engineering 18 (1) (2009) 015012.

[3] S. J. Stuart, A. B. Tutein, J. A. Harrison, A reactive potential for hydrocarbons with intermolecular interactions, The Journal of chemical physics 112 (14) (2000) 6472–6486.

[4] Q. Pei, Y. Zhang, V. Shenoy, A molecular dynamics study of the mechanical properties of hydrogen functionalized graphene, Carbon 48 (3) (2010) 898–904.

[5] J. Wang, D. C. Sorescu, S. Jeon, A. Belianinov, S. V. Kalinin, A. P. Baddorf, P. Maksymovych, Atomic intercalation to measure adhesion of graphene on graphite, Nature Communications 7.

[6] K. Kendall, Thin-film peeling-the elastic term, Journal of Physics D: Applied Physics 8 (13) (1975) 1449.

Chapter 5

Electron transport in Metals

5.1 Comparison and validation of methods for REEL spectra calculation

In this section the calculation of reflection electron energy loss (REEL) spectra of three metals (copper, silver and gold) was achieved with two different methods: (i) the Monte Carlo (MC) procedure as presented in the section 2.1 and (ii) the numerical solution (NS) of the Ambartsumian - Chandrasekhar equations using the Invariant Embedding Method [1]. In the following section the calculation of input data, concerning elastic and inelastic interaction, is presented. Regarding the inelastic scattering, two different energy loss function (ELF) were employed: one accounting only for plasmon bulk excitations and the other which includes both surface and bulk plasmon excitations. The two computational methods were tested with both the dielectric description and the results were compared to experimental measurements. The overall investigation was published in Ref. [2].

5.1.1 Calculation of input data

Logical flow of the calculations The calculation of REEL spectra, by means of MC or NS methods, starts from a database reporting information about elastic and inelastic scattering. Figure 5.1 outlines the sequence of computational steps to perform in order to simulate the emission spectra. Both computational methods include only elastic and inelastic scattering as interactions performed by electrons. In particular, the inelastic scattering was assessed by applying the Ritchie dielectric method as described above in section 2.1.2. The elastic scattering was evaluated by considering the Mott theory as explained in section 2.1.1. The calculated elastic and inelastic features, such as cross sections, mean free paths and cumulative probabilities as well as the routines implemented to evaluate them, are stored in the open access Mendley databases [3, 4, 5, 6]

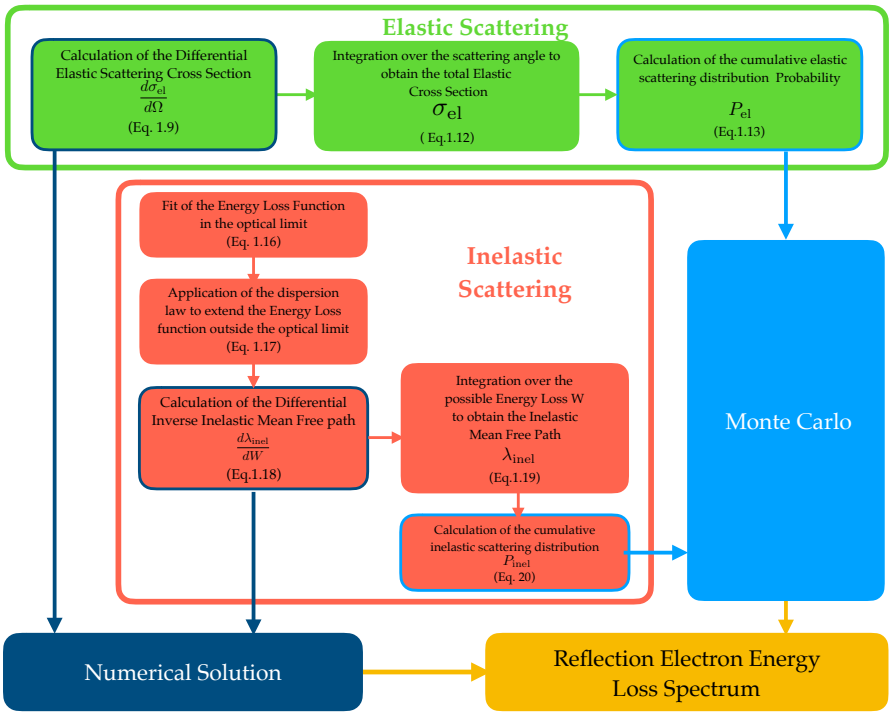

FIGURE 5.1: Sketch of the logical flow of the REEL spectra calculation [2]

Elastic scattering:

To simulate the elastic collisions, we solve according to the Mott approach [7] the Dirac equation in a central field using the partial wave expansion. In particular, the differential elastic scattering cross section (DESCS, $d\sigma_{el}/d\Omega$) is computed for each sample as reported in Eq. (2.9). The achieved DESCSs values for copper, silver, and gold are reported in figure 5.2 as a function of the scattering angle θ, for a beam kinetic energy of 1000 eV.

These values represent the input information necessary for performing NS calculations. To obtain the input data for the MC approach, the differential elastic scattering cross section is integrated over the possible elastic scattering angles to obtain the total elastic scattering cross section σ_{el} [Eq.(2.12)]. The elastic mean free path (EMFP), which is used in both MC and NS simulations, can be computed from Eq. 2.1. Finally, the elastic cumulative distribution probability is evaluated for the full range of possible scattering angles [Eq. (2.13)] and reported in Fig. 5.3. This latter set of data are provided as input information to the MC code suite for calculating the REEL spectrum.

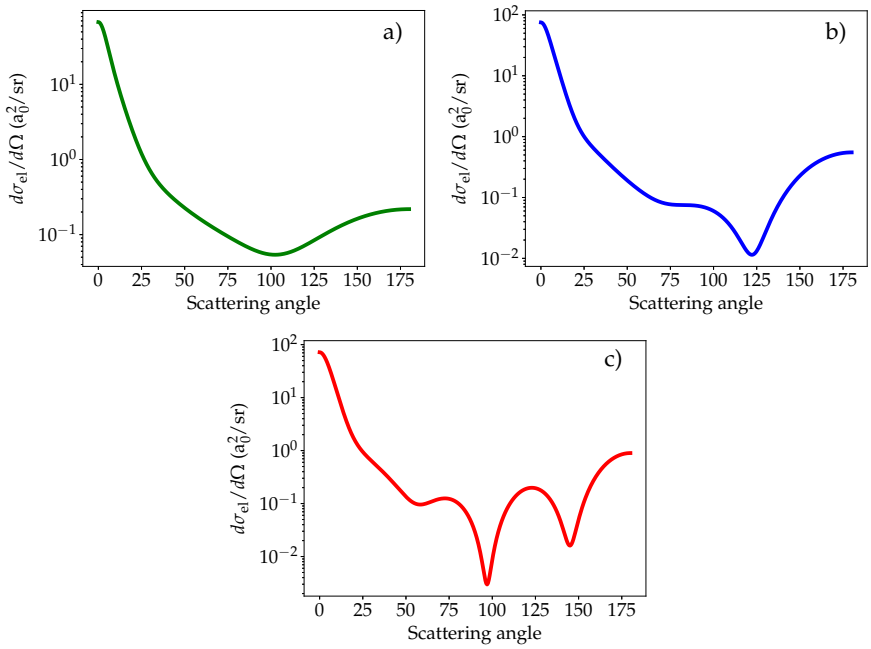

FIGURE 5.2: DESCSs of Cu a), Ag b) and Au c) as a function of the scattering angle. The kinetic energy of the primary beam is set to 1000 eV [2].

These cumulative distributions tend to 1 asymptotically and display a sharp slope at small scattering angles. The whole calculation concerning the elastic scattering is realized by running the MATLAB code Elastic_calculation.m in the ESCcal environment based on the ELSEPA code [8]. The code is made publicly available through the Mendeley database [6].

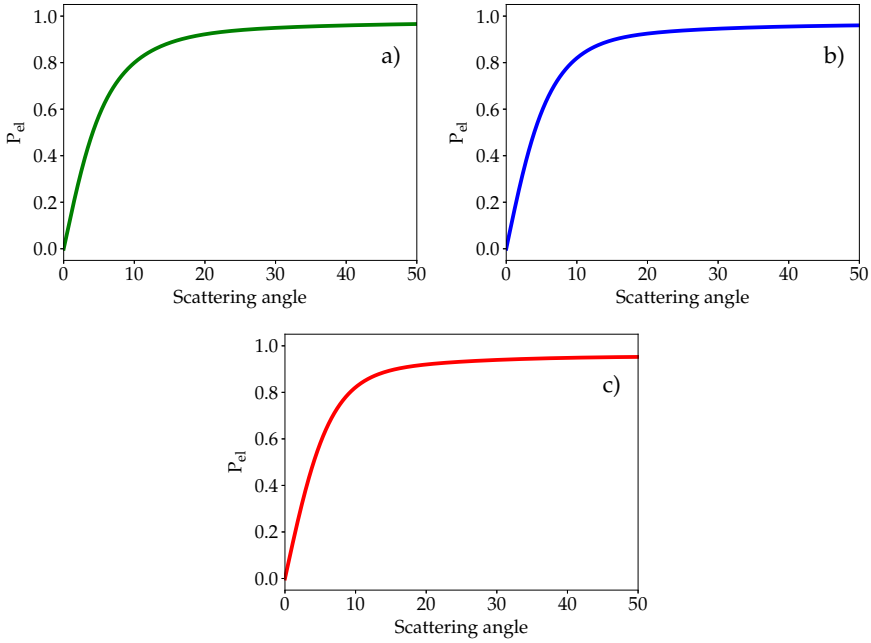

FIGURE 5.3: Cumulative elastic probability distributions of Cu a), Ag b) and Au c) as a function of the scattering angle. The kinetic energy of the primary beam is set to 1000 eV [2].

Inelastic scattering:

The description of the inelastic scattering is based on the Ritchie dielectric theory as described in the previous section 2.1.1. For the three investigated metals two different kinds of energy loss functions (ELF) in the optical limit were used to perform REEL calculations: the (i) the *bulk ELF* accounting for plasmon bulk excitations and (ii) the *effective ELF* which includes also the surface plasmon excitations. These ELFs were fitted [Eq. (2.16)] in the optical limit and then extended to finite momenta with the quadratic dispersion law (Eq. 2.17). The NS procedure requires the knowledge of the differential inverse inelastic mean free path (DIIMFP , $d\lambda_{\text{inel}}/dW$) as a function of the energy loss for a fixed initial kinetic energy, calculated by applying Eq. (2.18). Then the total inelastic mean free path (IMFP, λ_{inel}) is obtained by integrating the DIIMFP in the energy loss range (Eq. 2.19). The dataset required by the MC method is composed of the values of the cumulative inelastic probability distribution P_{inel} calculated as indicated in Eq. (2.20). The overall calculation of input data for inelastic scattering can be performed by running the Inelastic_calculation.cpp program, which is provided via the Mendeley database [4] . In the following paragraphs the input data, computed by applying the just described scheme, for the three metals with the two different ELFs, are presented

Bulk ELF As best-fit parameters for bulk ELFs in the optical limits, those reported by Smith et al. [9] were used for Ag, those achieved by Denton *et al.* [10] for Au and those achieved by C.C. Montanari et al [11] for Cu. The f-sum rule was verified with these parameters. The ELFs given by these best-fit parameters are shown in Fig. 5.19 and the used parameters are reported in Tab. 5.1.

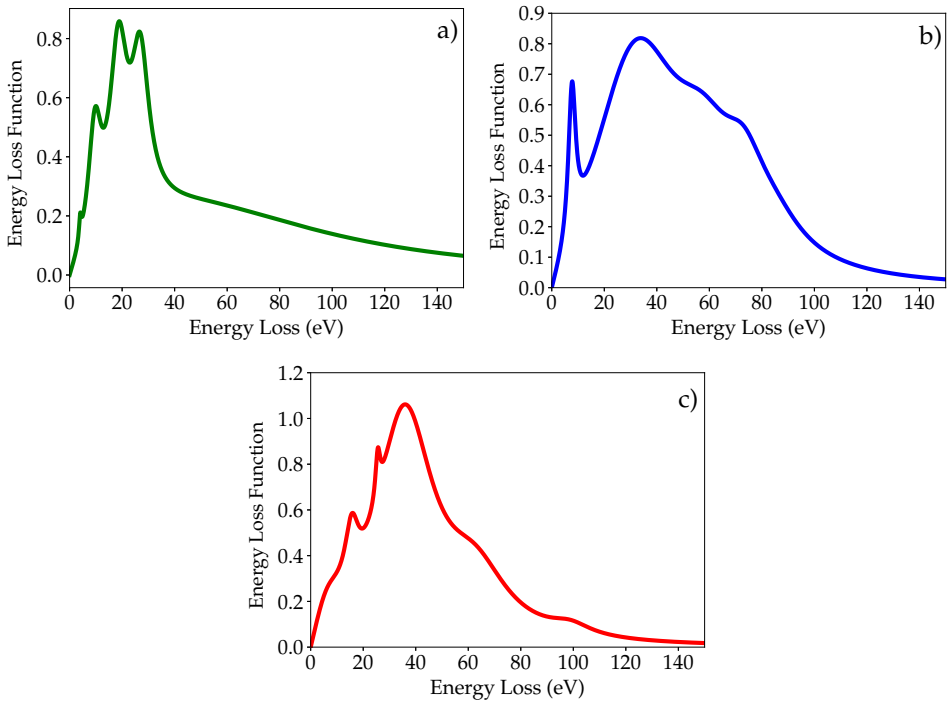

FIGURE 5.4: Bulk energy loss functions of Cu a), Ag b), and Au c) in the optical limit ($\vec{q} \longrightarrow 0$) obtained using Eq. (2.16). These ELFs were obtained by best-fitting the optical data reported in [9] for Ag, while we used the parameters from [11] and [10] for Cu and Au, respectively [2].

Cu				Ag				Au			
n	E_n (eV)	Γ_n (eV)	A_n (eV^2)	n	E_n (eV)	Γ_n (eV)	A_n (eV^2)	n	E_n (eV)	Γ_n (eV)	A_n (eV^2)
1	4.08	1.09	0.33	1	7.89	3.37	12.80	1	9.52	14.97	18.49
2	10.07	5.99	22.10	2	38.20	42.93	1109.46	2	15.92	6.26	25.85
3	19.05	8.16	88.91	3	59.58	29.93	480.38	3	25.58	2.18	11.12
4	27.21	8.16	112.54	4	73.81	20.12	300.6	4	38.09	26.67	973.52
5	78.91	152.38	2216.74	5	85.70	27.70	226.83	5	64.49	30.48	507.39
								6	99.32	19.05	88.88
								7	402.71	612.23	337.32

TABLE 5.1: Fit parameters of Equation (2.16) obtained for bulk ELFs. The best-fit parameters of Cu were provided by C.C. Montanari *et al.* [11], while for Au were given by C.D. Denton *et al.* [10]. In the case of Ag the parameters were obtained by best-fitting the optical measurements by Smith et al [9].

The DIIMFPs were calculated and for the three investigated materials are reported in Fig. 5.5 by considering the kinetic energy of the primary beam equal to 1000 eV. Those are the input data, relative to inelastic scattering, for the NS approach. Starting from the DIIMFPs also IMFPs were computed ad compared to those achieved by applying the Tanuma, Powell and Penn (TPP) algorithm [12] in Fig. 5.6.

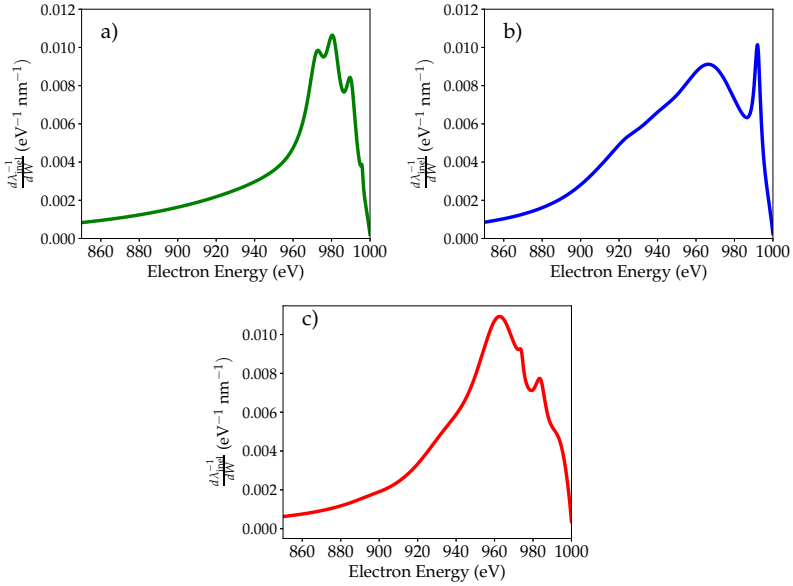

FIGURE 5.5: DIIMFP of Cu a), Ag b) and Au c) calculated using the Equation (2.18) and bulk ELFs, for a kinetic energy of the primary beam equal to 1000 eV [2].

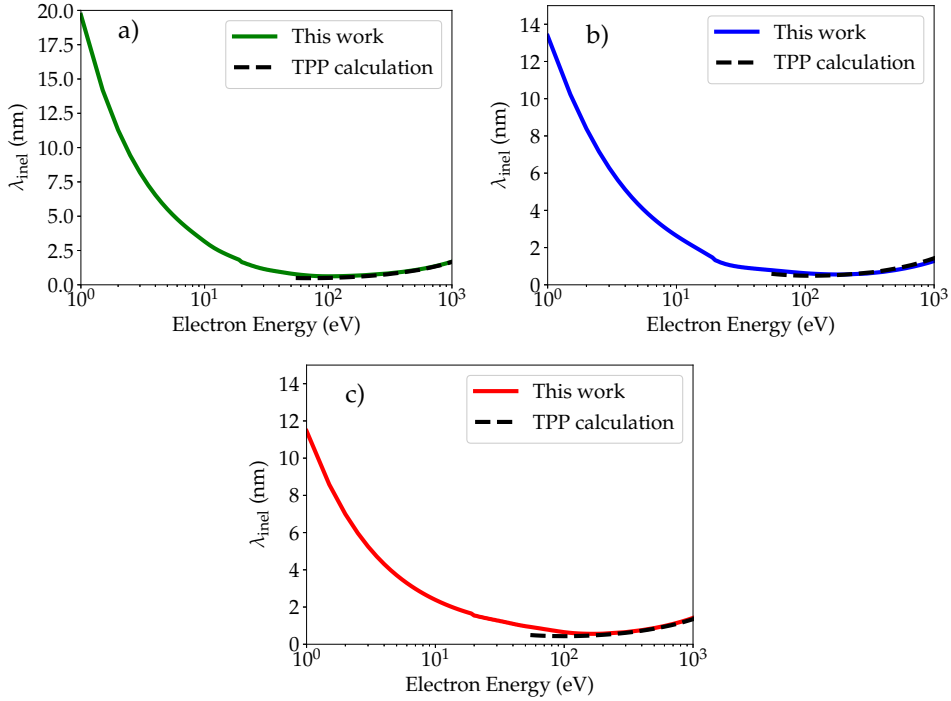

FIGURE 5.6: IMFPs for bulk ELFs of Cu a), Ag b) and Au c) compared with data reported by Tanuma et al. [12].

A good agreement between tabulated values, obtained with TPP algorithms, and the values achieved with our procedure is shown. To conclude the computation for the MC model, the inelastic cumulative probability distributions $P_{inel}(E_0, W)$, for the three materials, by setting the initial kinetic energy to 1000 eV, were calculated. These are shown in the following Fig. 5.7.

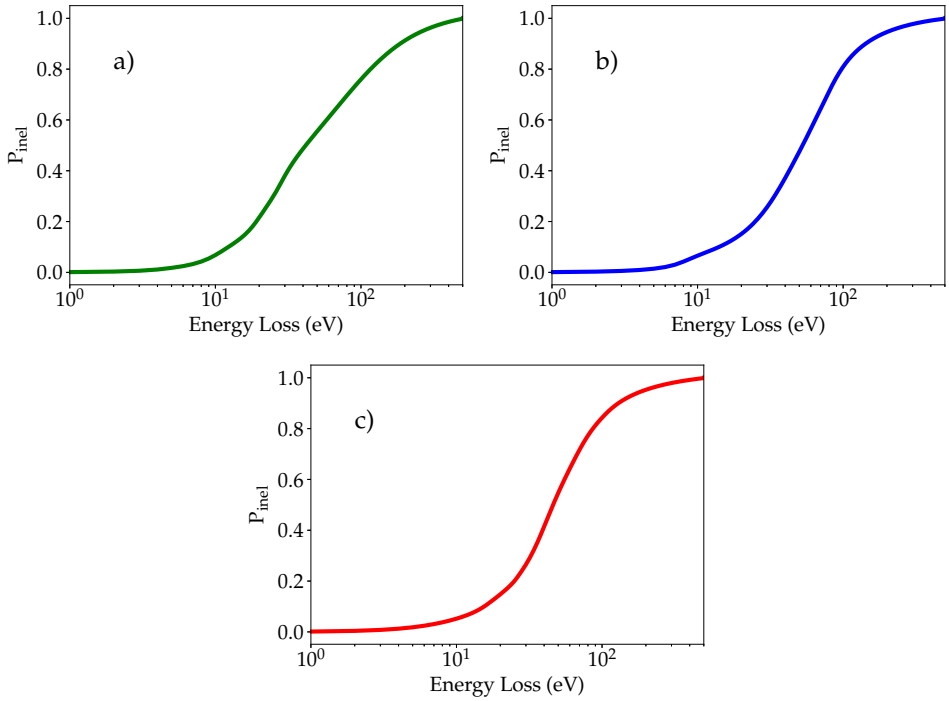

FIGURE 5.7: Cumulative inelastic probabilities as a function of energy loss of Cu a), Ag b) and Au c), obtained with Equation (2.13) and bulk ELFs, for a primary beam kinetic energy equal to 1000 eV [2].

The cumulative distributions tend to 1, but show the maximum slope at energy losses corresponding to the main bulk plasmon excitations.

Effective ELF for including surface plasmons A further step towards a higher accuracy of the overall REEL calculation can be achieved starting from ELFs which includes both surface and bulk plasmon excitations, a sort of *effective* ELFs. Those functions were computed by Nagatomi et al. [13] from experimental REEL spectra by applying the extended Landau theory [14]. These effective ELFs were fitted [Eq. (2.16)] by using the best-fit parameters reported in Tab. 5.2. The resulting functions are shown in 5.8. Compared to bulk ELFs, the effective ELFs present more complex structures, reporting a different variety of excitations. To well reproduce these features the number of used oscillators is increased with respect to the previous case.

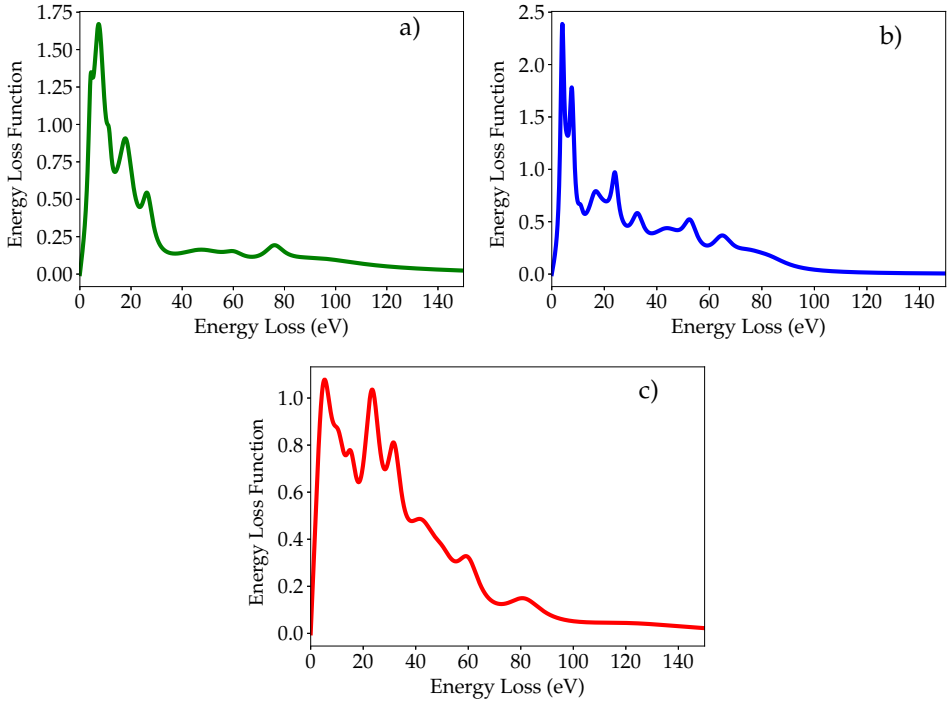

FIGURE 5.8: Effective energy loss functions of Cu a), Ag b), and Au c) in the optical limit ($\vec{q} \longrightarrow 0$) obtained by using Eq. (2.16). These ELFs were obtained by best-fitting the effective ELFs calculated by Nagatomi et al [13, 2].

Cu				Ag				Au			
n	E_n (eV)	Γ_n (eV)	A_n (eV^2)	n	E_n (eV)	Γ_n (eV)	A_n (eV^2)	n	E_n (eV)	Γ_n (eV)	A_n (eV^2)
1	4.28	2.09	5.80	1	4.09	1.70	13.80	1	6.40	8.77	46.92
2	7.90	5.79	67.00	2	5.91	2.80	8.42	2	11.11	6.52	26.16
3	11.45	2.20	6.50	3	7.73	2.13	21.16	3	26.16	5.62	30.56
4	14.76	5.20	5.20	4	10.98	2.30	3.72	4	23.68	7.72	148.97
5	18.30	7.16	95.00	5	16.58	4.80	15.80	5	31.90	6.90	110.32
6	26.51	5.16	50.12	6	20.58	18.20	190.83	6	42.82	15.60	220.60
7	48.91	25.30	146.00	7	24.10	2.90	33.60	7	50.51	11.20	65.50
8	60.30	9.30	28.20	8	32.75	5.60	53.60	8	60.12	10.70	132.50
9	76.20	9.00	75.20	9	44.48	16.20	220.30	9	81.65	16.78	143.20
10	95.20	45.00	330.00	10	52.75	6.50	102.20	10	125.60	60.30	250.50
11	130.40	90.30	180.20	11	65.09	9.20	138.50				
				12	75.21	16.50	140.70				
				13	83.15	17.30	120.50				

TABLE 5.2: The best-fit parameters (Eq. (2.16)) of effective ELFs of Cu, Ag and Au.

To compute the DIIMFP, necessary for the NS approach, the ELFs function were extended towards the optical limit with the dispersion law [Eq. (2.17)]. Then those values were integrated in Eq.(2.18) obtaining the DIIMFPs reported, for the metals, in the following Fig. 5.9, for an initial kinetic energy of the beam equal to 1000 eV.

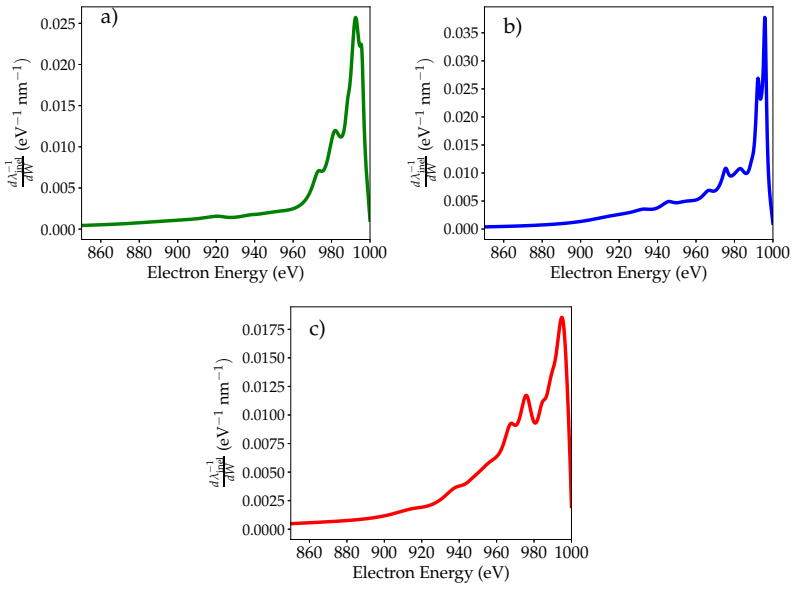

FIGURE 5.9: DIIMFPs of Cu a), Ag b) and Au c) calculated using Eq. (2.18) and the effective ELFs, for a kinetic energy of the primary beam equal to 1000 eV [2].

The IMFPs were then computed by integrating the DIIMFPs as indicated by Eq. (2.19). The thus obtained IMFPs are shown together with the tabulated data, achieved with the Tanuma Powell Penn algorithm, in Fig. 5.10.

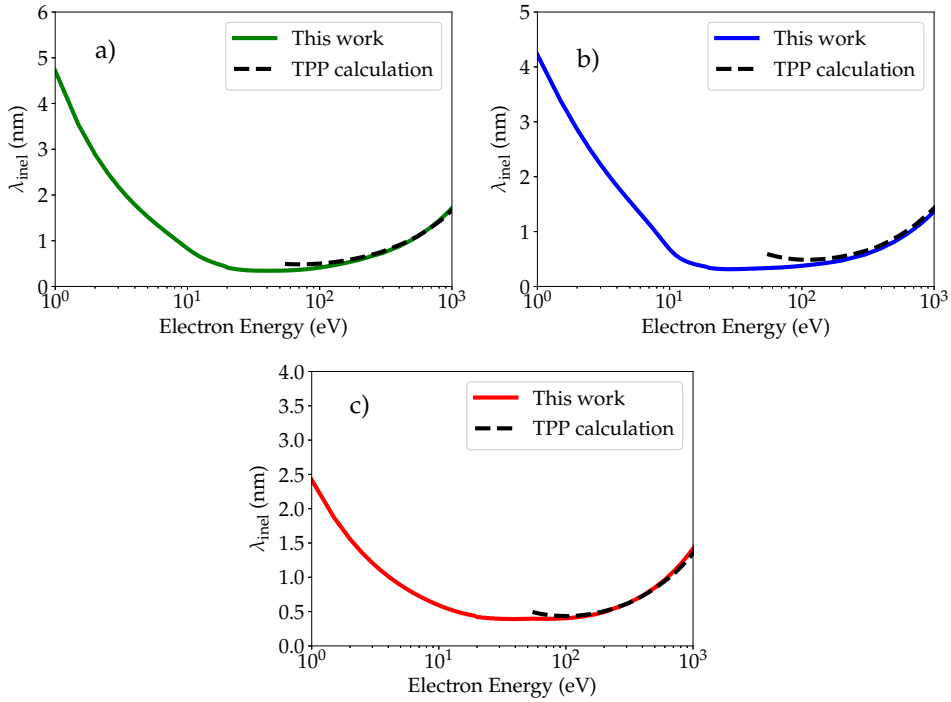

FIGURE 5.10: IMFPs calculated using the effective ELFs, of Cu a), Ag b) and Au c) compared to data reported by Tanuma et al [12, 2] .

The cumulative inelastic probabilities, to pass as input information to MC routines, were obtained with Eq. 2.20 and displayed for the three samples and kinetic energy equal to 1000 eV in Fig. 5.11.

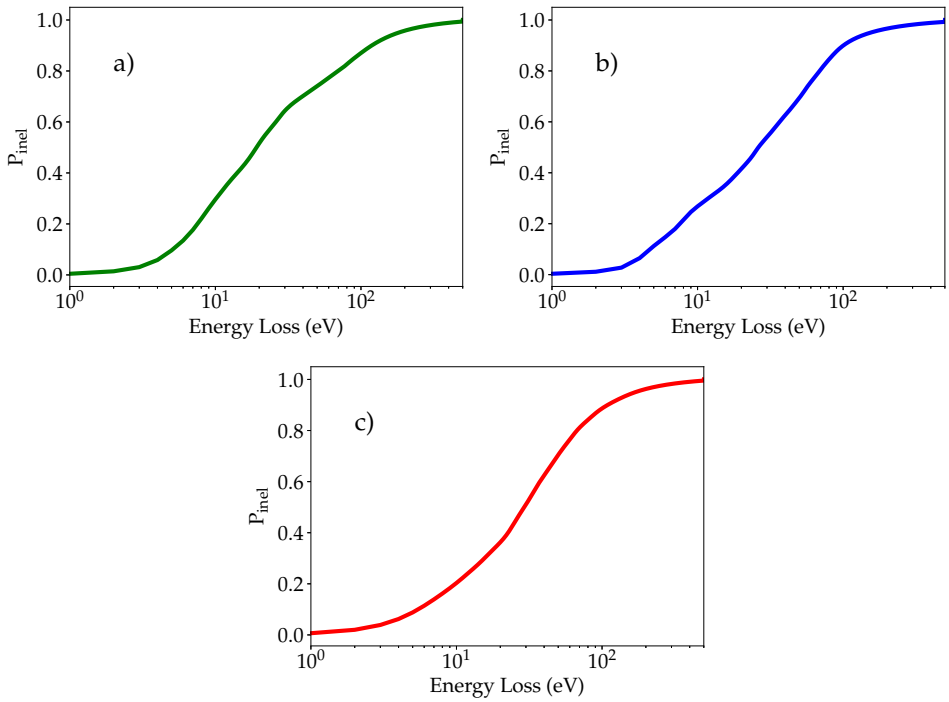

FIGURE 5.11: Cumulative inelastic probabilities as a function of energy loss of Cu a), Ag b) and Au c), obtained with Eq. (2.20) and effective ELFs, for a primary beam kinetic energy equal to 1000 eV[2].

As in the previous case, the distributions tends to 1 and the slope varies at energy loss values correspondent to main plasmon excitations.

5.1.2 REEL spectra results and discussion

REEL spectra of the three different metal samples, copper, silver and gold, were modeled by using the following characteristic parameters reported in Tab. 5.3.

	Cu	Ag	Au
density (g/cm^3)	8.96 [11]	10.5[12]	19.32[10]
λ_{el} (nm)	0.866	0.783	0.677
λ_{inel} (Bulk ELF) (nm)	1.686	1.277	1.414
λ_{inel} (Effective ELF) (nm)	1.713	1.369	1.418

TABLE 5.3: Target material characteristic parameters. Elastic and inelastic mean free paths have been assessed at $E_0 = 1000$ eV primary beam kinetic energy [2].

In both the approaches to calculate REEL spectra, the initial kinetic energy of beam electrons was set to 1000 eV and the beam was maintained orthogonal to the surface. In the NS approach, to calculate REEL, only the primary electrons which had undergone at maximum 25 inelastic collisions were considered in the computation. In the MC procedure, to asses the sufficient statistic avoiding noisy signals, 10^9 electron trajectories were computed.

Bulk ELF: Fig. 6.10 shows the comparison between REEL spectra obtained by means of MC and NS computations and Nagatomi et al. calculations [13], all considering the input data produced with the bulk ELFs of the three samples. An overall agreement between the three calculated spectra, for all the sample, is reached. Moreover, from this comparison, the MC and NS results can be considered equivalent for all intents and practical purposes.

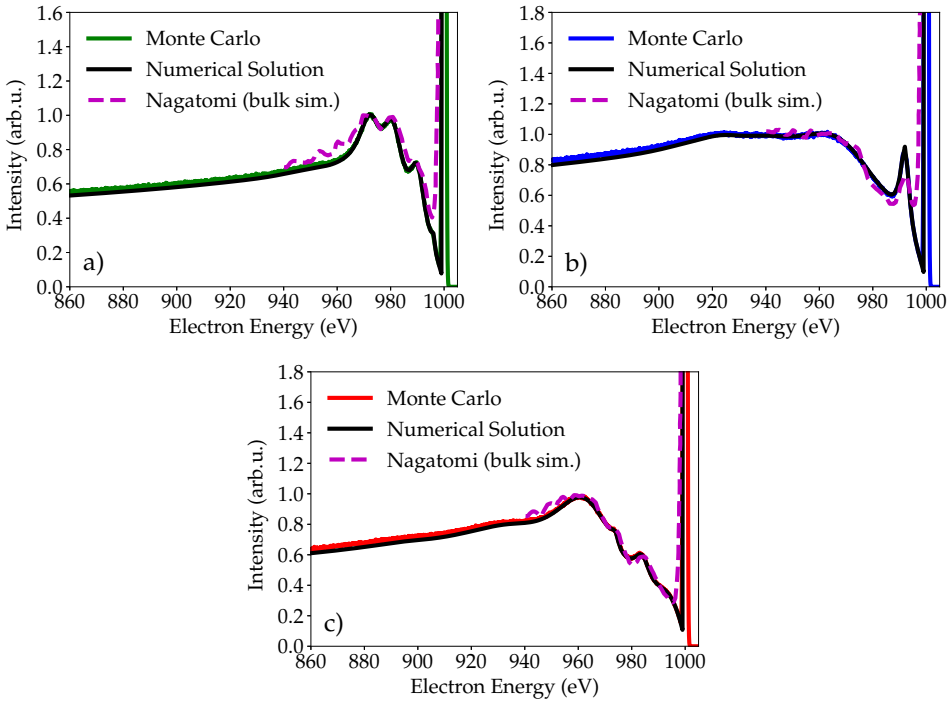

FIGURE 5.12: REEL spectra of Cu a), Ag b), and Au c), obtained by the NS (black curves) and MC approaches, for a primary beam kinetic energy equal to 1000 eV and by considering bulk ELFs. Our results are compared to the spectra calculated by Nagatomi et al [13] (magenta dashed lines). The data are normalized to a common height of the main plasmon peak [2].

By deconvoluting the REEL spectra (Fig. 5.13), as a function of the number of inelastic interactions that electrons at most undergo in their way out of the solid, the main contributors to the spectra are given by those electrons which undergone only one inelastic interaction. Indeed, this contribution follows the trend of the DIIMFP (Fig. 5.5). From this analysis can be seen that the electrons performing more inelastic interactions contribute directly to the part of the spectrum ascribable to multiple plasmon excitations. Furthermore, also in this case, the agreement between the deconvoluted spectra assessed with the two approaches result to be very satisfactory.

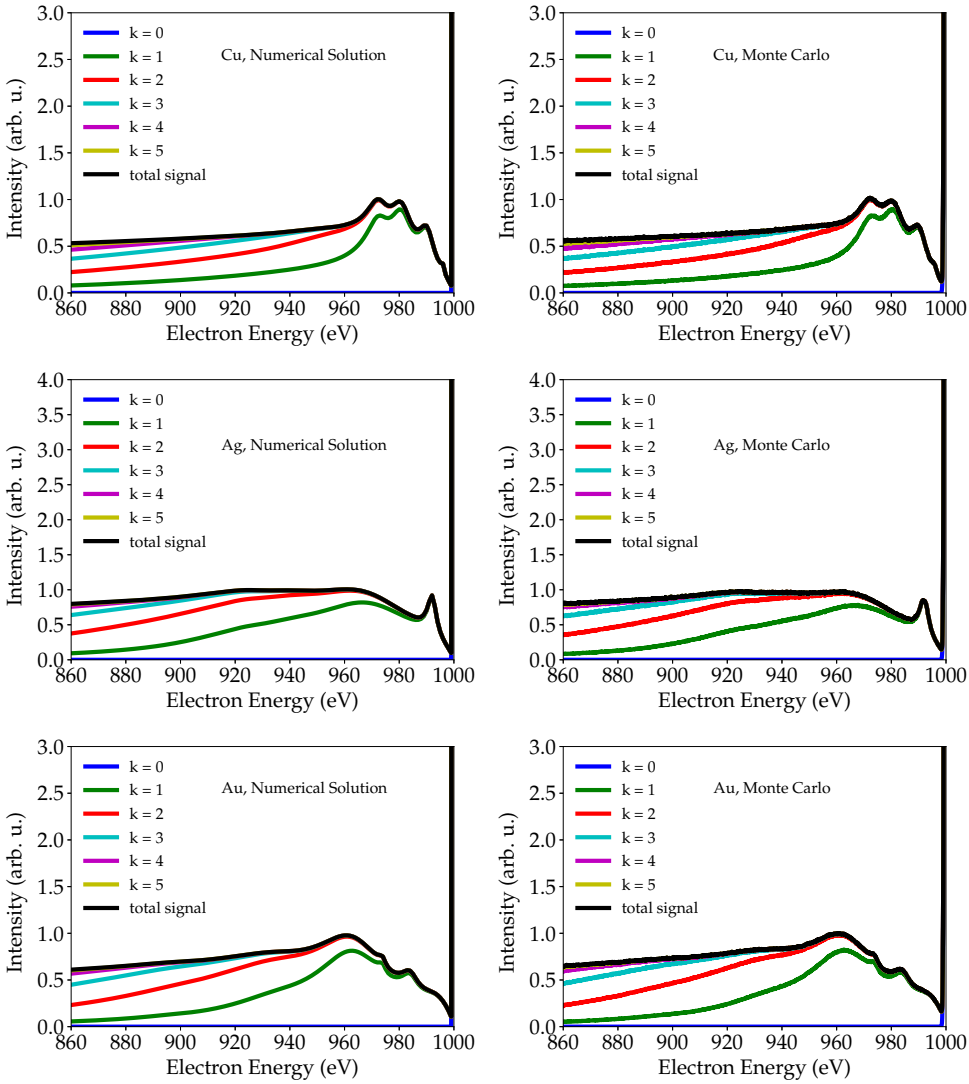

FIGURE 5.13: REEL spectra of Cu, Ag and Au, deconvoluted for the number of inelastic collisions that electrons undergo in their way out of the solid. On the right panel we show MC simulations, while on the left panel we report the same quantities obtained by the NS approach. The primary beam kinetic energy is set to 1000 eV. The data are normalized at a common height of the main plasmon peak [2].

Effective ELF To include surface plasmon excitation, naturally present in experimental REEL spectra, calculations (MC and NS) were performed by using inelastic scattering databases, obtained with the effective ELF. Indeed, the inclusion of those kinds of interaction leads to a good agreement with the experimental data. Fig. 5.14 shows the correspondence of calculated spectra, for copper, silver and gold with the experimental curves acquired by Nagatomi et al. [13]. Also in these case, the theoretical spectra computed with the two investigated procedures produces comparable lineshapes.

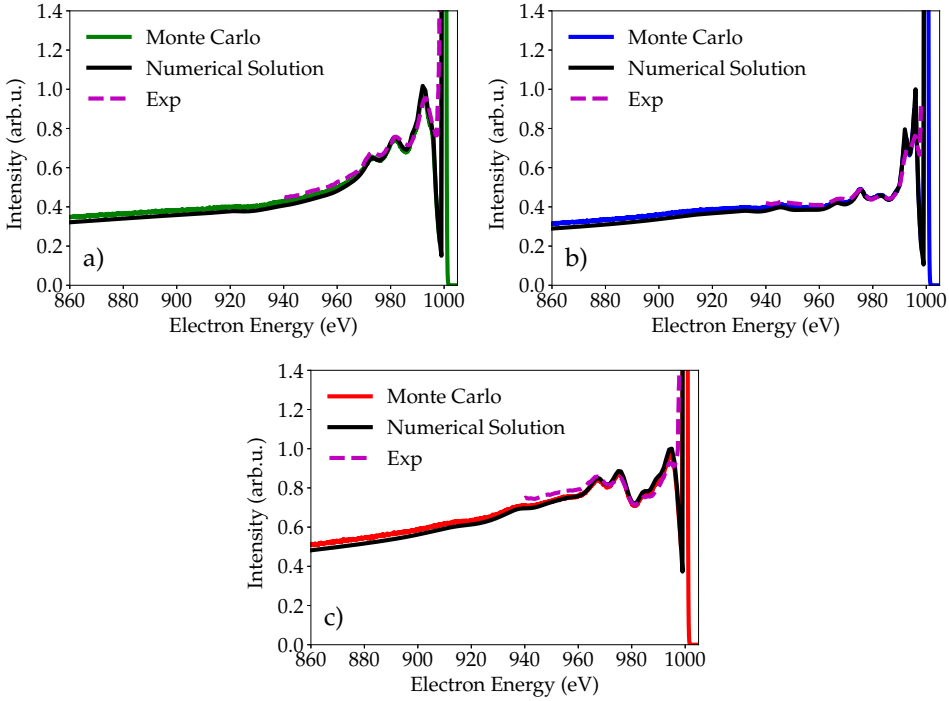

FIGURE 5.14: REEL spectra of Cu a), Ag b), and Au c), obtained by the NS (black curves) and MC approaches, for a primary beam kinetic energy equal to 1000 eV, starting from Effective ELF. Our results are compared to the experimental spectra by Nagatomi et al [13] (magenta lines). The data are normalized at a common height of the background [2].

Concerning the computational cost, the NS procedure results to be quantitatively less expensive than MC method. Computational efficiency tests were performed by running simulation on 2.9 Ghz Intel Core i7 processors. MC method performs REEL calculation employing 4 CPUs for 70 minutes, while NS procedure runs on only one CPU and delivers results in 10 seconds. However, it is worth noting that the MC method reproduces the full emission spectrum, considering also the generation and emission of low energy secondary electrons, while NS provides information concerning only back-scattered electrons. Nevertheless, from these

investigations it was proved the equivalence of the two independent computational methods in the calculation of REEL spectra. The choice between the two has to be made in function of the required information and on the available computational resource.

5.2 Calculation of Secondary electron yield of metals

In this section, the application of the MC method for the calculation of the secondary electron emission yield of copper, silver and gold is presented. The method was applied starting from dielectric functions derived from REEL experiments. The full emission spectra and yield curves as a function of different initial kinetic energies were calculated. These theoretical results were compared to experimental measurements recorded by the experimental INFN group in Frascati. This section is mainly based on the results reported in our published paper [15].

Monte Carlo model

For the purpose of this investigation, the MC model was set by including elastic and inelastic interactions. Moreover the secondary electrons generations and their consequent trajectories were carefully simulated. The overall calculation followed the algorithm reported in the previous section 2.1. The kinetic energy of the beam electrons is determined by considering the energy distribution of the experimental elastic peak. The elastic peak of the energy emission spectrum is generated by those electrons which have been elastically reflected by the target surface, and thus it provides information about the energy distribution of the beam. In order to reproduce the experimental distribution of the elastic peak, the initial kinetic energy of the beam was set to a fixed value E, and then a correction ΔE was added. To evaluate this correction, the experimental elastic peak of copper is taken into account. First of all the elastic peak was centered to zero and the resulting curve is named $f(\Delta E)$ (Fig. 5.15a), where ΔE represents the energy correction. The total area of the peak was calculated by integrating the experimental $f(\Delta E)$ curve in the energy symmetric interval $[E_-; E_+]$, with $E_\pm = \pm 2.5$ eV to obtain the total peak area.

$$Area = \int_{E_-}^{E_+} f(\Delta E')d(\Delta E'). \tag{5.1}$$

Then, the cumulative distribution probability (Fig. 5.15 b), describing the experimental elastic peak, is computed, as a function of the energy correction, by applying the following equation:

$$P(\Delta E) = \frac{1}{Area} \int_{E_-}^{\Delta E} f(\Delta E')d(\Delta E'). \tag{5.2}$$

For each electron in the beam, the value of the correction ΔE to add to the set initial kinetic has to be determined. This is done by generating another random number r, uniformly distributed in the interval [0,1]. Then the value of ΔE for which the $P(\Delta E)$ is equal to r is identified. So the initial kinetic energy of the considered electron was set to $E + \Delta E$.
In the next sections the input data to pass to the MC routine are displayed and discussed, subsequently the calculated full emission spectra and secondary electron yields are presented. In

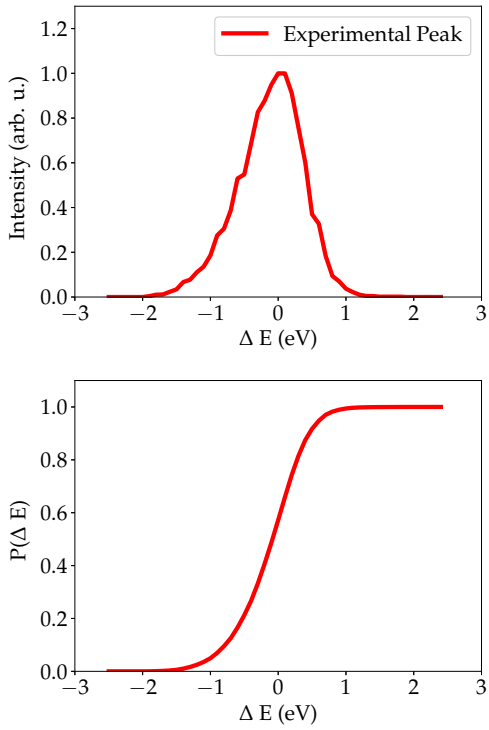

FIGURE 5.15: (Upper panel) Experimental elastic peak of copper; (Lower Panel) Cumulative probability distribution describing the experimental elastic peak [15].

particular the role of the work function is probed in promoting or preventing the emission of electrons from the sample interface.

Elastic scattering

The Mott theory [7], as described in section 2.1.1, was applied to calculate elastic features for copper, silver and gold. The analytical formulation of the atomic potential proposed by Salvat et al. [16] was used (see Appendix A). The total elastic scattering cross section is obtained by integrating Eq. (2.9) in the solid angle [Eq.(2.12)] . The results are shown in Fig. 5.16 and compared with tabulated values [17].

To evaluate the scattering angle, the cumulative elastic scattering probabilities are calculated for different values of electron kinetic energy E with Eq. 2.13 . Some of them are shown for the three samples in Fig. 5.17:

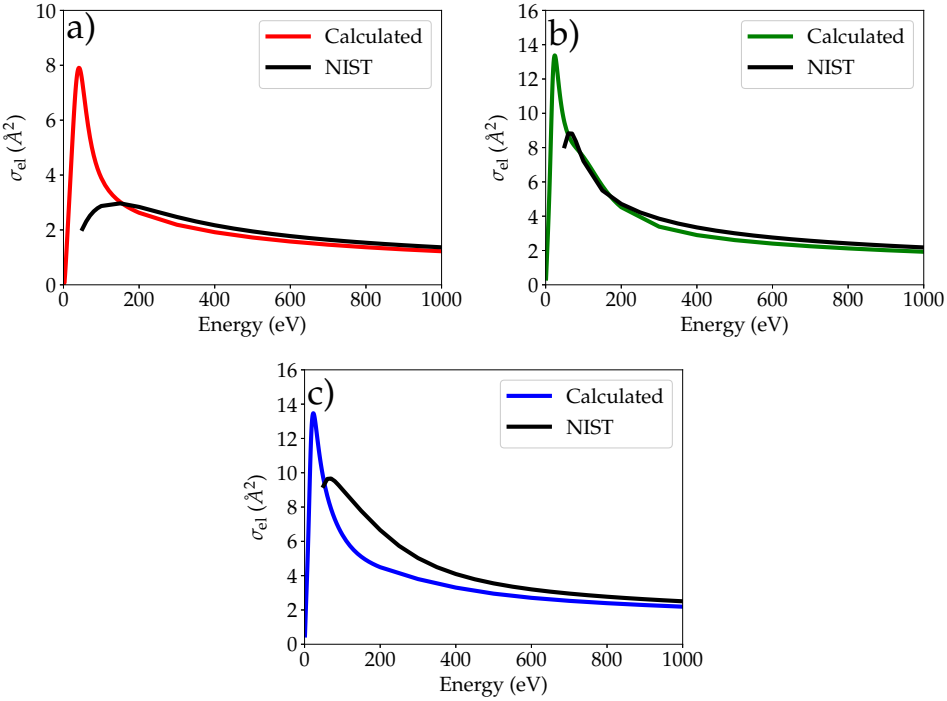

FIGURE 5.16: Total elastic scattering cross section of Cu a), Ag b) and Au c) as a function of electron kinetic energy. Black lines report tabulated values [17, 15].

Inelastic scattering and secondary electron generation

The electrons are slowed down during their path, due to inelastic scattering with atomic electrons. The travelling electrons transfer a fraction of their kinetic energy, producing both excitations and ionizations. To describe these interactions, the Ritchie dielectric theory, as described in section 2.1.2, was applied with some variations. In particular, we decided to use the dielectric functions calculated from experimental REEL spectra by Werner et al. [18]. The obtained functions include both the bulk and the surface excitations. The real and imaginary components were fitted with Drude-Lorentz functions, which represent plasmon oscillations.

The fitting parameters proposed by Werner in ref. [18] are reported in Tab. 5.4 and the resulting components of the dielectric functions of Cu, Ag and Au, for transferred momentum equal to zero, are shown in Fig.5.18.

The ELF, which represents the key quantity in the Ritchie dielectric theory, is defined as:

$$ELF = \mathrm{Im}\left[-\frac{1}{\epsilon(q,W)}\right] \tag{5.3}$$

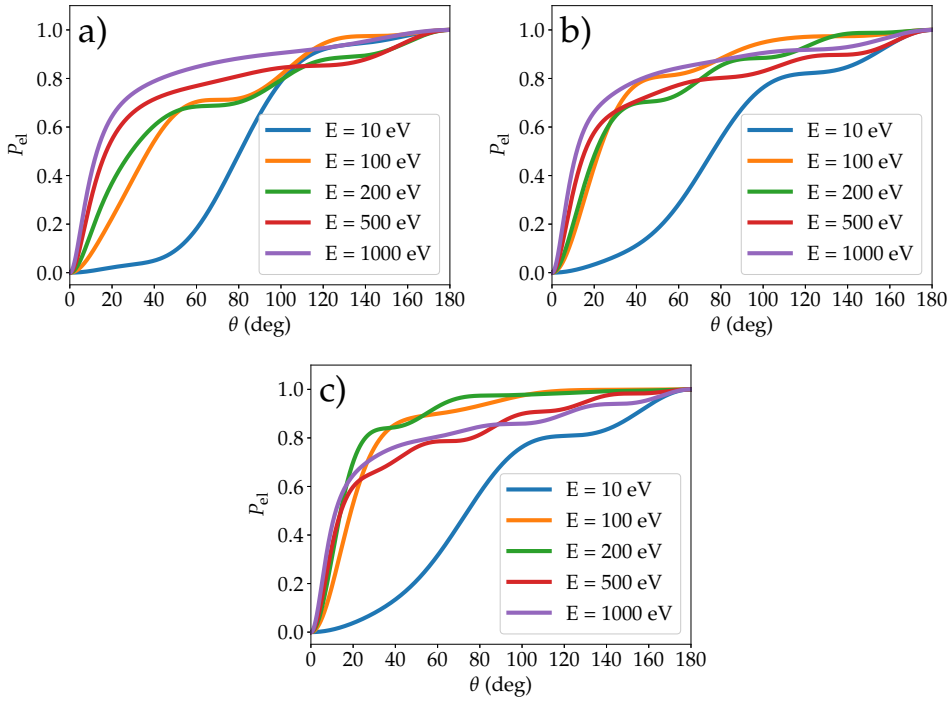

FIGURE 5.17: Cumulative elastic scattering probabilities of Cu a), Ag b) and Au c), as a function of the scattering angle and for different kinetic energies [15].

Cu				Ag				Au			
n	E_n (eV)	Γ_n (eV)	A_n (eV^2)	n	E_n (eV)	Γ_n (eV)	A_n (eV^2)	n	E_n (eV)	Γ_n (eV)	A_n (eV^2)
1	0.00	0.027	86.3	1	0.000	0.065	98.4	1	0.000	0.2	113.1
2	1.0	0.5	19.8	2	1.0	93.8	103.9	2	4.0	1.5	44.6
3	1.0	0.5	21.9	3	4.9	0.7	23.8	3	7.3	3.3	54.8
4	4.0	1.7	30.2	4	10.3	22.0	318.3	4	12.8	11.8	184.9
5	4.8	0.5	2.5	5	13.2	6.3	89.6	5	18.9	71.0	728.1
6	7.2	11.3	157.7	6	21.2	3.3	63.5	6	19.9	2.9	65.7
7	14.2	10.1	130.9	7	30.2	3.7	43.3	7	28.9	3.9	50.0
8	16.9	68.2	108.6	8	43.0	16.7	313.3	8	38.7	13.0	74.7
9	24.3	3.0	40.0	9	65.7	38.8	519.9	9	64.3	51.9	1544.0
10	59.4	55.1	1022.4								

TABLE 5.4: The best-fit parameters (Eq. (2.16)) of effective ELFs of Cu, Ag and Au proposed by Werner in ref [18] .

and can be calculated as:

$$ELF = \frac{\mathrm{Im}[\epsilon]}{\mathrm{Re}[\epsilon]^2 + \mathrm{Im}[\epsilon]^2} \tag{5.4}$$

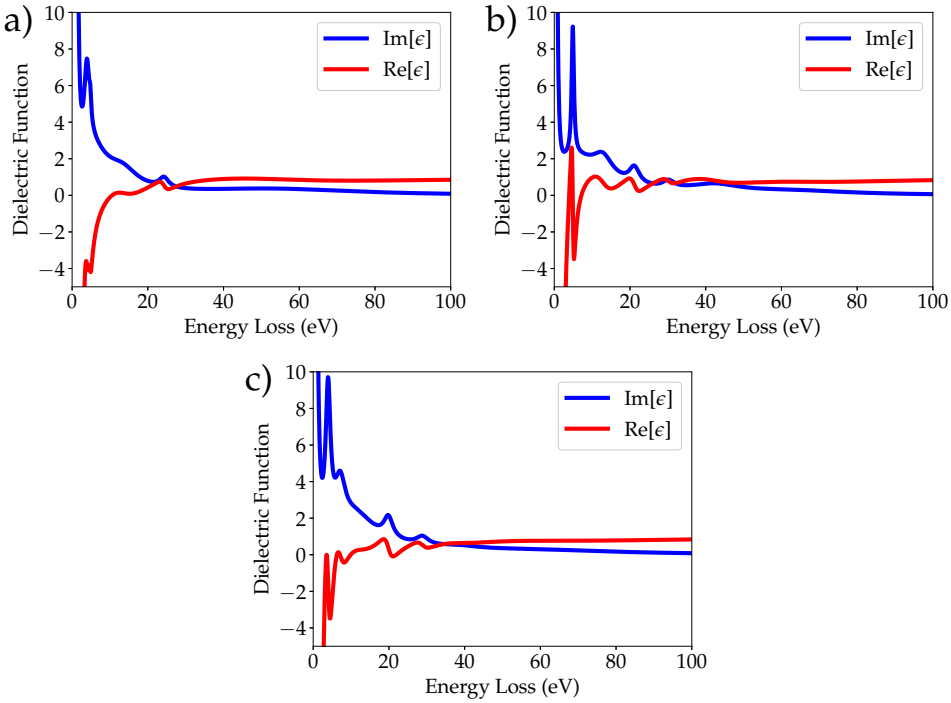

FIGURE 5.18: Dielectric function components of Cu a), Ag b) and Au c), as a function of energy loss and for transferred momentum equal to zero, obtained with fitting parameters by Werner et al. [15, 18].

The ELF calculated, from the dielectric function components reported above, are shown, for the three investigated materials, in Fig. 5.19.

To extend the dielectric function to transferred momentum $\vec{q}$ different from zero, a dispersion law has to be applied to the characteristic energies of the oscillators [$W_i(q)$]:

$$W_i(q) = W_i(q=0) + \beta\frac{(\hbar q^2)}{2m} \tag{5.5}$$

where m is the electron mass, q the transferred momentum and β the dispersion coefficient. The Drude-Lorentz theory was developed to describe the excitation in the low energy region, corresponding to energy losses lower than the semi-core transition energy. To extend properly the Drude-Lorentz theory for higher energy the value of the β dispersion parameter has to be tuned. This latter value was set, according to Ref. [18], to 1 for oscillator energies $W_i(q=0)$ lower than the characteristic energy of the semi-core transitions. For larger oscillators energy, it was set to 0.5, which ensures the highest agreement with experimental data [18]. In particular, for the investigated targets, the threshold energies of the semi-core transitions are for Cu

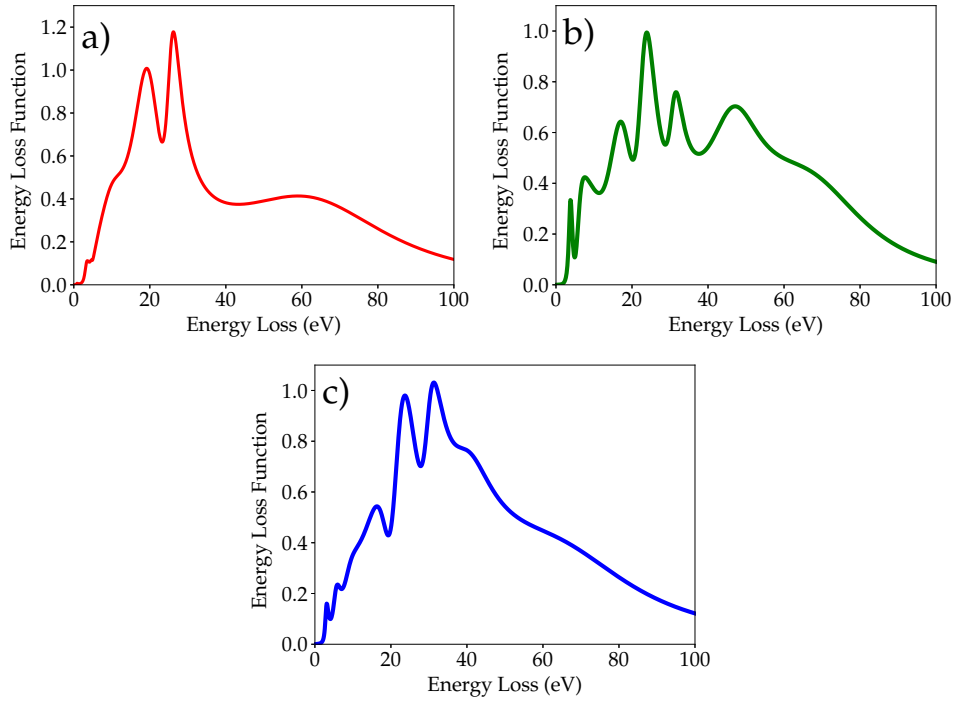

FIGURE 5.19: Energy Loss Functions of Cu a), Ag b) and Au c), as a function of energy loss and for transferred momentum equal to zero, obtained with fitting parameters by Werner et al. [18, 15].

$E_{3p3/2} =$ 75.1eV, for Ag $E_{5p3/2}$ =57.2 eV and for Au $E_{4p3/2} =$ 58.3 eV [18].
Starting from the ELFs thus evaluated and expanded, the calculation of the differential inelastic mean free paths, inelastic mean free paths and inelastic cumulative probabilities proceeds as reported in section 2.1.2. The inelastic mean free paths of the three samples are shown in Fig. 5.20 and compared with calculation presented by Tanuma et al. [19].

As a results of an inelastic interaction, the impinging electron loses a fraction W of its kinetic energy. To identify the energy loss due to each interaction, the cumulative inelastic probabilities $P_{\text{inel}}(E, W)$ were a calculated as in Eq. (2.20). Some distributions are reported in the following figures as a function of energy loss values (Fig. 5.21).

If the energy loss is larger than the first ionization energy <B>, an ionization occurs and a secondary electron is emitted with an initial kinetic energy equal to $W-$<B>. The first ionization energy is the energy required to extract one electron from the external electron shell of the target atom. At this point, the generated secondary electron starts to travel in the target solid. Otherwise the transferred energy triggers an excitation of the atom, without causing the emission of a secondary electron.

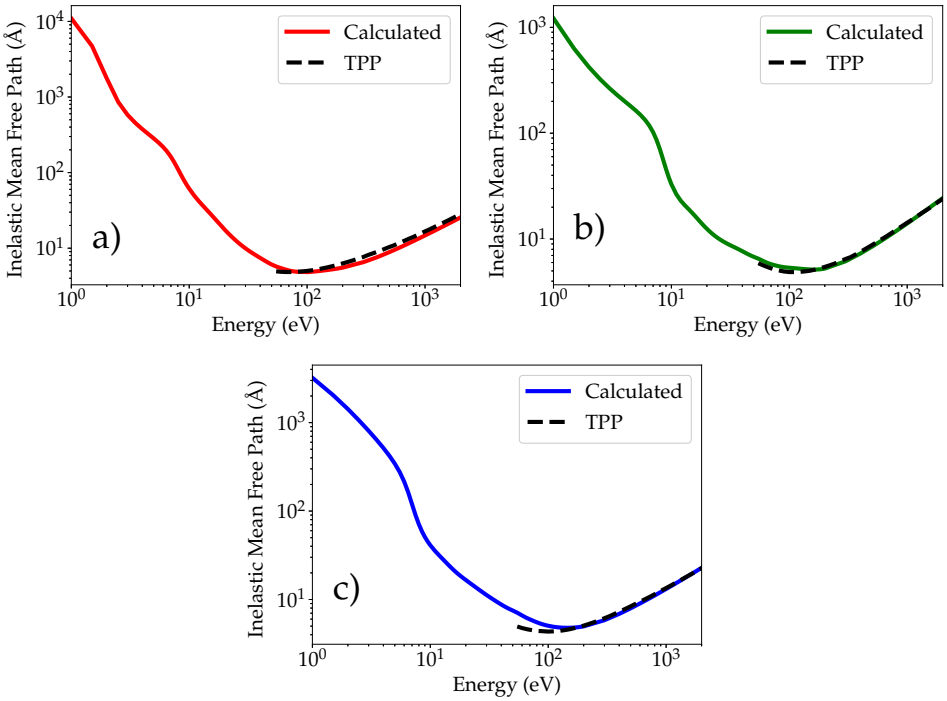

FIGURE 5.20: Inelastic Mean Free Paths of Cu a), Ag b) and Au c), as a function of kinetic electron energy. Dashed lines represent the results obtained by Tanuma et al. [19, 15].

To decide the type of interaction, distribution probabilities and generated random numbers (uniformly distributed in the interval [0,1]) are involved. The distribution probabilities, p_{el} and p_{inel}, regarding the tendency of electrons to undergo respectively an elastic or inelastic scattering, are computed starting from the total mean free path λ, defined as:

$$\lambda^{-1}(E) = \lambda_{\text{inel}}^{-1}(E) + \lambda_{\text{el}}^{-1}(E) \tag{5.6}$$

The distributions, as a function of kinetic energy, are given by:

$$p_{\text{el}} = \frac{\lambda}{\lambda_{\text{el}}} \tag{5.7}$$

$$p_{\text{inel}} = \frac{\lambda}{\lambda_{\text{inel}}} \tag{5.8}$$

These are reported in Fig. 5.22.

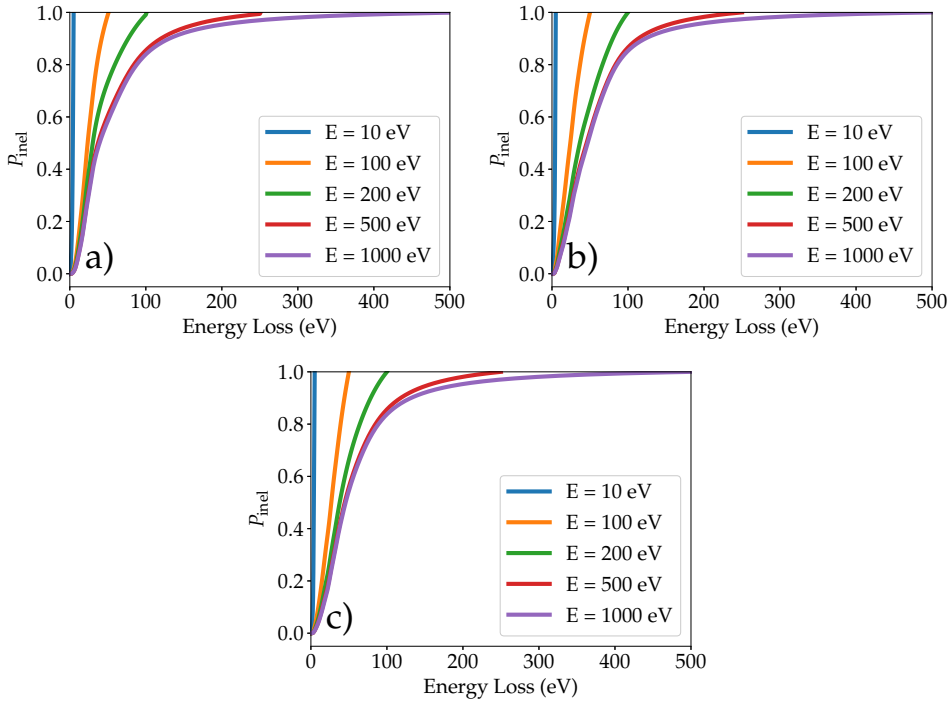

FIGURE 5.21: Cumulative inelastic scattering probabilities of Cu a), Ag b) and Au c), as a function of the energy loss and for different kinetic energies [15].

5.2.1 Results and discussion

In MC simulations, copper, silver and gold bulks were considered as targets. In the following table (Tab. 5.5) the characteristic features are reported. In the next sections the results concerning full spectra of copper and electron yield of the three metals are presented.

Metal	density (g/cm^3)	<B> (eV)
Cu	8.96 [11]	7.726
Ag	10.5[19]	7.576
Au	19.32[10]	9.226

TABLE 5.5: Characteristic quantities of target materials [15].

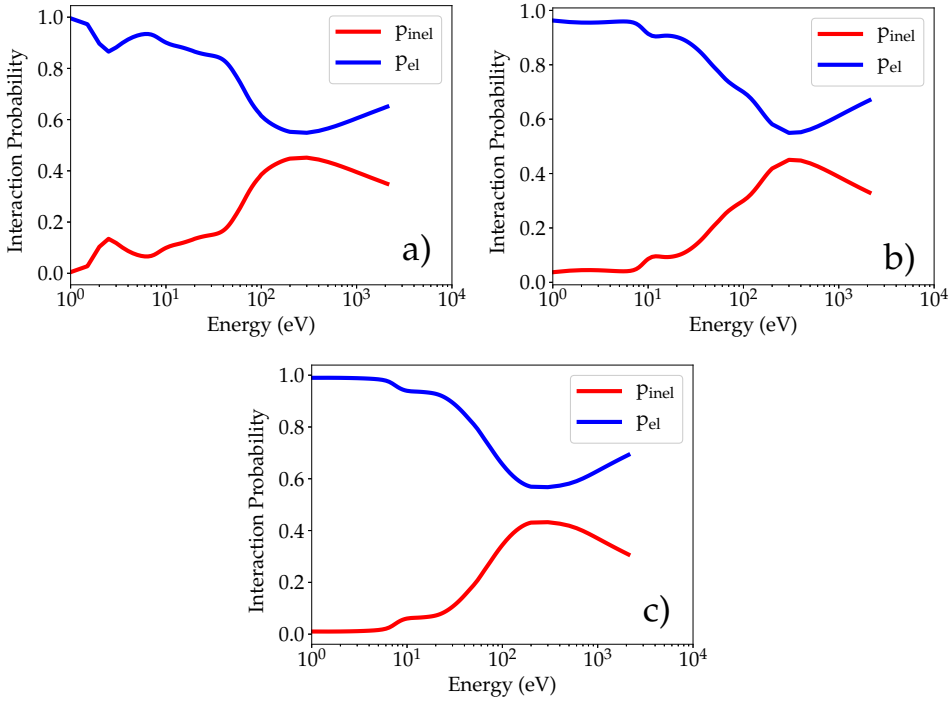

FIGURE 5.22: Scattering probabilities for Cu a), Ag b) and Au c) as a function of the electron energy [15].

Full energy emission spectra of Cu

MC simulations were performed by considering bulk copper as target material, to calculate the full energy emission spectrum for different initial beam energies E. The number of sent electrons was set to 10^7 to ensure stable results. The sample work function was set to 5.4 eV. Emitted electrons are collected as a function of their kinetic energies. The spectra were calculated by considering the initial electron energy distributed as the reference copper experimental elastic peak reported above (Fig. 1). The obtained spectra are compared with experimental data (recorded by R. Cimino INFN group in Frascati) for different initial kinetic energies and they are reported in Fig. 5.23. The left panels show spectra normalized at a common height of the secondary electron (SE) emission peak, the right panels show the spectra normalized at a common area.

The experimental spectra were acquired with a retarding field analyzer (RFA) which is known to cause a characteristic broadening of the elastic peak due to poor resolution at high energies and a strong asymmetry on the low energy side due to the integration of the background [20, 21]. Due to this, the integrated area of the whole elastic peak is always higher than

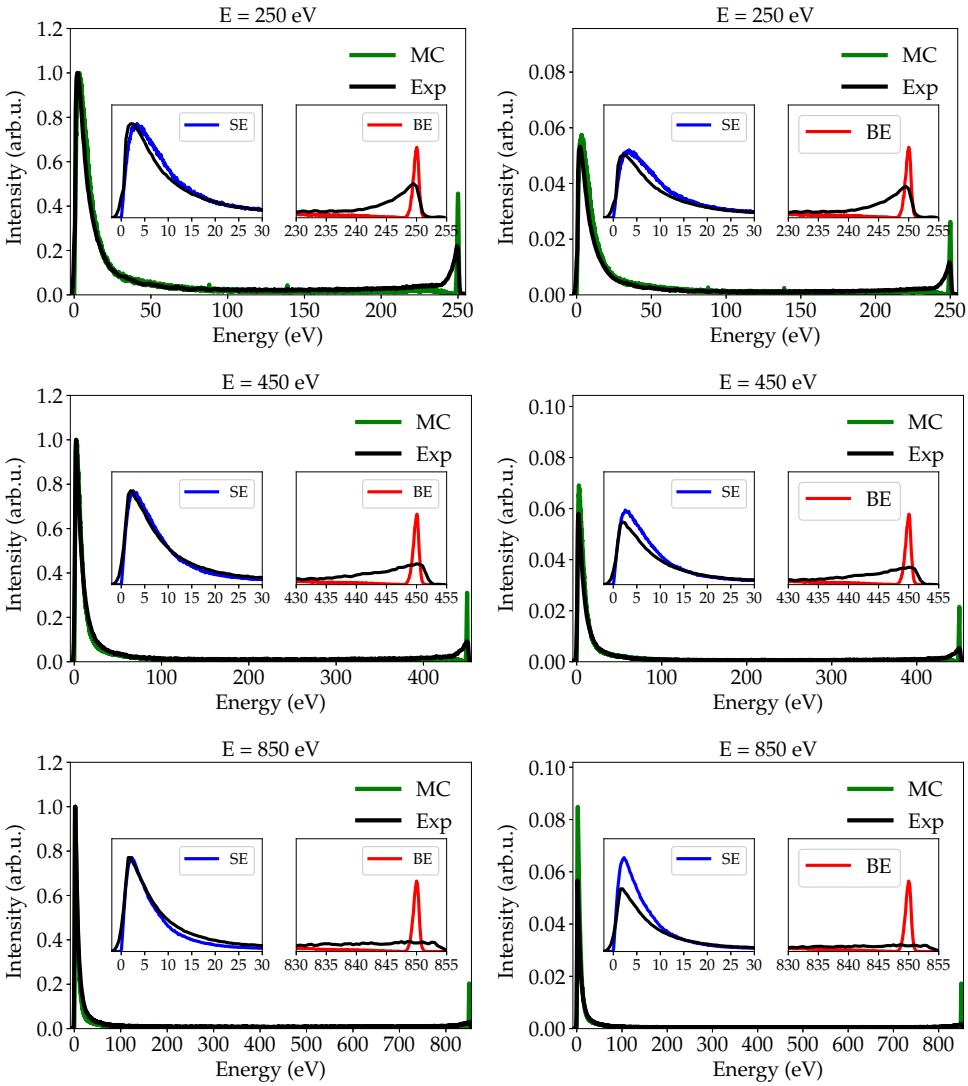

FIGURE 5.23: Electron energy emission spectra for different initial kinetic energies. The central panels of each figures frame the two main parts of the spectrum: the secondary electron (SE) emission peak in blue and the back-scattered electrons (BE) in red. The experimental data are reported in all the figures with black lines. The figures on the left report spectra normalized at a common height of the secondary electron emission peak. The figures on the right show spectra which are normalized at a common total area of the spectrum [15].

the MC one [22, 23]. As a result, in the case of spectra normalized at a common area (right panels), the MC secondary electron (SE) peaks are more intense than the experimental ones. On the other hand, by normalizing at a common height of the secondary electron emission peak, it is evident that a very good agreement is reached between the shape of SE MC peaks and SE experimental peaks.

Electron yield

The electron yield is defined as the total number of emitted electrons divided by the number of electrons in the beam. It was calculated by considering the three investigated metals, Cu, Ag and Au, for different kinetic energies. The role of the work function was investigated: different simulation runs were carried out by changing this parameter. To calculate the electron yield curves, 10^6 electrons in the beam were considered. In Fig. 6.21, calculated electron yield curves are compared to experimental data by Gonzales et al. [24].

These results clearly show that the increase of the energy barrier, represented by the work function, decreases the number of electrons which have the possibility to emerge from the surface. Indeed, curves calculated with a higher value of χ, show lower intensities than the ones obtained with a lower χ. The best agreement with the experimental data [24], is reached for copper, silver and gold respectively with χ equal to 5.4 eV, 4.4 eV and 4.7 eV. The value of χ measured experimentally by Gonzales et al. [24], are for copper, silver and gold equal respectively to 4.6 eV, 4.4 eV and 5.3 eV. Thus, for silver, we got the agreement with yield curves and this agreement is reached by setting the value of the work function equal to the one measured experimentally. In the case of copper, the best MC curve was obtained with a χ higher than the experimental value. The curve which ensures the highest agreement for gold, was achieved by using a value of χ smaller than the experimental value.

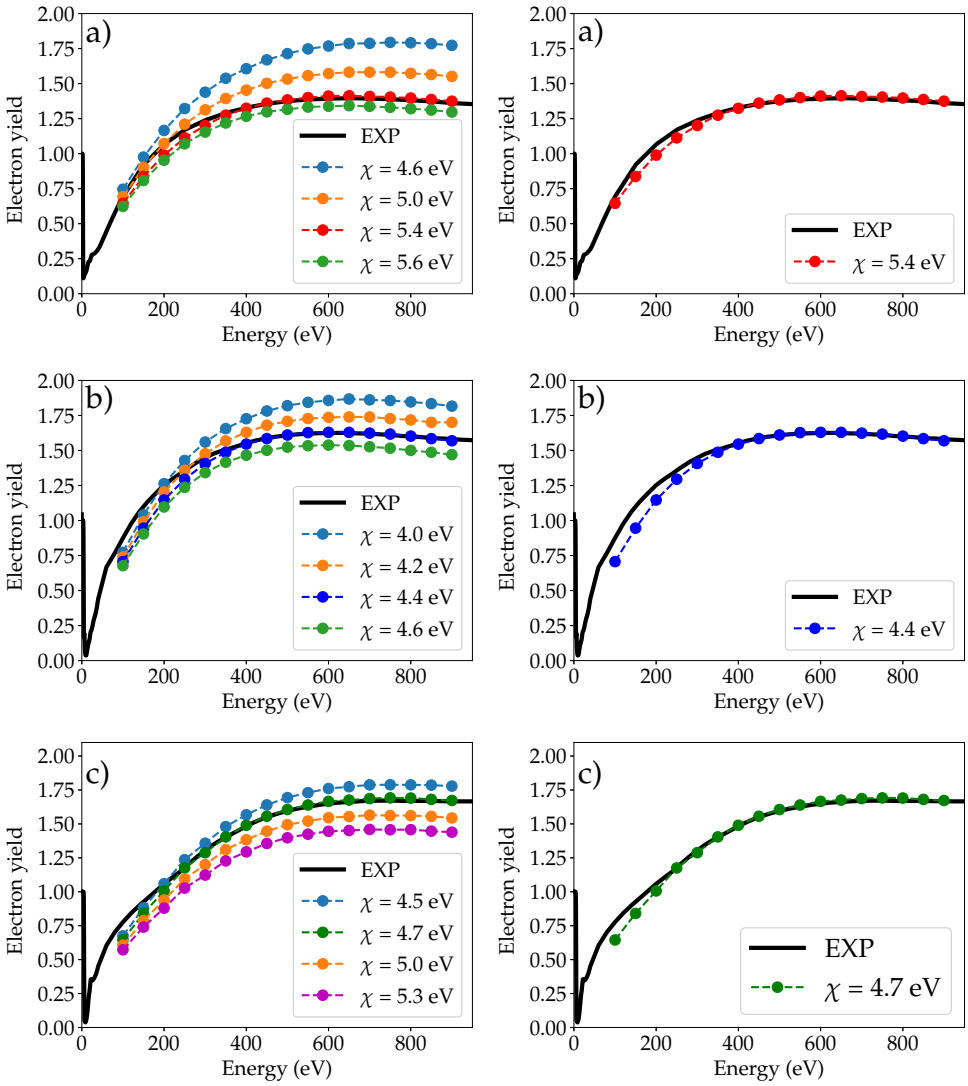

FIGURE 5.24: Electron yield curves of Cu a), Ag b) and Au c) as a function of the electron energy, for different values of work functions χ (left panels). In black experimental data are reported [24]. Right panels show the best agreement between calculated data and experimental curve [15].

5.3 Conclusions

In this section, the performances of MC method against NS of the Ambartsumian - Chandrasekhar equations were compared in terms of accuracy and computational cost for calculating REEL spectra of several metals, such as Cu, Ag and Au. To obtain a fair comparison, the computations were performed using the same input data in each test case, which means the same IMFPs for the relevant test cases. The spectra obtained with these two methods are comparable and show a good agreement with experimental data, even when including the effective description of the ELFs for dealing with surface plasmon excitations. The spectra were further analyzed by resolving the spectral contribution of the electrons as a function of the maximum number of inelastic collisions in their way out of the solid. Even in this case, the results obtained are comparable for any practical purpose. Thus, these two approaches can be considered equivalent with respect to accuracy for the simulation of REEL spectra in solids and they both can be used to test materials dielectric response. Moreover, these approaches are very versatile as they basically require as input data information on the materials ELFs, which can be obtained by using several tools, from experimental measurements to *ab-initio* simulations [25]. Nevertheless, we notice that the NS approach is much faster than MC, having a computational cost lower of about two orders of magnitude concerning CPU time, once input data are provided to the main program routine. However, MC gives access to a number of different data, such as multiple scattering and secondary electron yields, which can be useful to give some insight into SEM microscopy or, generally, into imaging techniques [2]. Indeed, the MC method was then applied in the calculation of secondary electron trajectories for the three different metals (copper, silver and gold). In particular, in the second part of the chapter the MC calculation of the complete electron emission spectra and secondary electron yield curves are presented. The calculations were performed by changing the value of the work functions, and the variations in the secondary electron yields were analyzed. The best agreement with yield experimental curves was reached by setting the values of work function very close to the experimentally measured values [24].

Bibliography

[1] V. Afanasev, D. Efremenko, P. Kaplya, Analytical and numerical methods for computing electron partial intensities in the case of multilayer systems, Journal of Electron Spectroscopy and Related Phenomena 210 (2016) 16.

[2] M. Azzolini, O. Riedzel, P. Kaplya, V. Afanasev, N. M. Pugno, S. Taioli, M. Dapor, Computational tools for calculating reel spectra in solids: a comparison between monte carlo method and the numerical solution of the Ambartsumian-Chandrasekhar equations,, Submitted.

[3] M. Azzolini, Input data set of Cu, Ag and Au, regarding electron elastic and inelastic scattering, for the calculation of the reflection electron energy loss spectra, Mendeley Data, v1 (2018).

[4] M. Dapor, M. Azzolini, Ritchie dielectric theory: calculation of the inelastic mean free path, of the differential inverse inelastic mean free path and of the cumulative inelastic probability distribution, Mendeley Data, v1 (2018).

[5] P. Kaplya, O. Y. Ridzel, M. Azzolini, Calculation of REEL spectra by applying the numerical solution of the Ambartsymian-Chandrasekhar equation, Mendeley Data, v1 (2018).

[6] P. Kaplya, O. Y. Ridzel, M. Azzolini, Electron elastic scattering treated with the Mott theory: calculation of the elastic mean free path, of the differential elastic cross section and of the cumulative elastic probability distribution, Mendeley Data, v1 (2018).

[7] N. Mott, The scattering of fast electrons by atomic nuclei, Proc. R. Soc. London, Ser. A 124 (794) (1929) 425.

[8] F. Salvat, A. Jablonski, C. Powell, Elsepa—dirac partial-wave calculation of elastic scattering of electrons and positrons by atoms, positive ions and molecules, Computer physics communications 165 (2) (2005) 157.

[9] D. Smith, E. Shiles, M. Inokuti, E. Palik, Handbook of optical constants of solids, Handbook of Optical Constants of Solids 1 (1985) 369.

[10] C. Denton, I. Abril, R. Garcia-Molina, J. Moreno-Marín, S. Heredia-Avalos, Influence of the description of the target energy-loss function on the energy loss of swift projectiles, Surface and Interface Analysis 40 (11) (2008) 1481–1487.

[11] C. Montanari, J. Miraglia, S. Heredia-Avalos, R. Garcia-Molina, I. Abril, Calculation of energy-loss straggling of C, Al, Si, and Cufor fast H, He, and Li ions, Physical Review A 75 (2) (2007) 022903.

[12] S. Tanuma, C. Powell, D. Penn, Calculations of electron inelastic mean free paths. IX. data for 41 elemental solids over the 50 eV to 30 keV range, Surface and Interface Analysis 43 (3) (2011) 689.

[13] T. Nagatomi, Y. Takai, B. Crist, K. Goto, R. Shimizu, Construction of database of effective energy-loss functions, Surface and Interface Analysis 35 (2) (2003) 174.

[14] H. Yoshikawa, Y. Irokawa, R. Shimizu, Measurements of reflected electron energy loss spectrometry and x-ray photoelectron spectroscopy spectra for derivations of the energy loss function and source function for Au 4f photoelectrons, Journal of Vacuum Science & Technology A 13 (4) (1995) 1984–1989.

[15] M. Azzolini, M. Angelucci, R. Cimino, R. Larciprete, N. M. Pugno, S. Taioli, M. Dapor, Secondary electron emission and yield spectra of metals from Monte Carlo simulations and experiments, Journal of Physics: Condensed Matter 31 (5) (2018) 055901.

[16] F. Salvat, J. Martinez, R. Mayol, J. Parellada, Analytical Dirac-Hartree-Fock-Slater screening function for atoms (Z=1–92), Phys. Rev. A 36 (1987) 467–474.

[17] A. Jablonski, F. Salvat, C. Powell, Nist electron elastic-scattering cross-section database, NIST Standard Reference Database 64.

[18] W. S. Werner, K. Glantschnig, C. Ambrosch-Draxl, Optical constants and inelastic electron-scattering data for 17 elemental metals, Journal of Physical and Chemical Reference Data 38 (4) (2009) 1013–1092.

[19] S. Tanuma, C. Powell, D. Penn, Calculations of electron inelastic mean free paths. IX. Data for 41 elemental solids over the 50 eV to 30 keV range, Surface and Interface Analysis 43 (2011) 689.

[20] G. Gergely, Elastic backscattering of electrons: determination of physical parameters of electron transport processes by elastic peak electron spectroscopy, Progress in surface science 71 (1-4) (2002) 31–88.

[21] A. Sulyok, G. Gergely, B. Gruzza, Spectrometer corrections for a retarding field analyser used for elastic peak electron spectroscopy and auger electron spectroscopy, Acta Physica Hungarica 72 (1) (1992) 107.

[22] D. Zeze, L. Bideux, B. Gruzza, F. Gołek, D. Dańko, S. Mroz, Retarding field analyser used in elastic peak electron spectroscopy, Vacuum 48 (3-4) (1997) 399–401.

[23] B. Gruzza, S. Chelda, C. Robert-Goumet, L. Bideux, G. Monier, Monte carlo simulation for multi-mode elastic peak electron spectroscopy of crystalline materials: Effects of surface structure and excitation, Surface Science 604 (2) (2010) 217–226.

[24] L. Gonzalez, M. Angelucci, R. Larciprete, R. Cimino, The secondary electron yield of noble metal surfaces, AIP Advances 7 (11) (2017) 115203.

[25] M. Azzolini, T. Morresi, G. Garberoglio, L. Calliari, N. M. Pugno, S. Taioli, M. Dapor, Monte carlo simulations of measured electron energy-loss spectra of diamond and graphite: Role of dielectric-response models, Carbon 118 (2017) 299.

Chapter 6

SiO_2: substrate for FEDIB technique

The purpose of this chapter is to analyze the contribution of backscattered and secondary electron in the focused electron beam induced deposition (FEBID) technique in the deposition of 2D and 3D nanostructures. This procedure involves a high energy electron beam impinging on a layer of adsorbed molecules deposited on a given substrate. The high energy electrons (primary and backscattered) fragment precursor adsorbed molecules by dissociative ionization, resulting in a complete loss of all ligands. Moreover, given their high energy these electrons reach the substrate and traveling inside the solid they generate avalanches of secondary electrons. Those low energy electrons can manage to reach the surface and escape. Even if they also interact with adsorbed molecules, they participate in the precursors fragmentation with a dissociative electron attachment process, resulting in an incomplete ligand loss. Hence a consistent action of secondary will produce "dirty" nanostructures at the end of the overall deposition process [1]. To simulate the FEDIB process two different models has to be combined: (i) for the transport of primary and secondary electrons through the substrate the MC model is used and (ii) to consider the fragmentation, dynamics and reaction of precursor molecules on the substrate [2] the irradiation driven molecular dynamics (IDMD) is implemented. In particular, the MC procedure allows obtaining electron energy spectra at several annular patches around the beam center. The electron energies and fluxes will be used to determine fragmentation rates for precursor molecules, to be used in IDMD. Then IDMD can be used to follow the time evolution of precursor molecules in the silica substrate and the growing nanostructures (size and composition). In this section only the first part, regarding the MC simulation is treated. The theoretical group at the University of Alicante and at the University of Murcia contributes in the calculation of input inelastic cross sections and performed the IDMD procedure. As a working example, the same situation as in [2] will be considered: a 30 keV primary electron beam of 5 nm-radius impinging on a SiO_2 surface covered with $W(CO)_6$ molecules. This choice in materials was done since the availability of experimental data on these samples. In this chapter, the calculation of input data for the MC model and a detailed discussion of the delivered results of the relative simulations are provided.

6.1 Set up of the Monte Carlo simulation

Monte Carlo simulations of electron transport were realized by considering as target material SiO_2 with the following characteristic quantities (Tab.6.1) :

Z	30
atomic mass	60.0735 u.m.a
density	2.19 g/cm^3
Energy Band Gap (E_g)	8.9 eV
Work Function (χ)	0.9 eV (Ref. [3])
Mean Ionization Energy (<B>)	12.2 eV

TABLE 6.1: Characteristic quantities of target material.

The MC simulations were carried out as reported in section 2.1 by including inelastic and elastic scattering and also electron−phonon interaction. Among those the inelastic interaction involves a loss of energy, if the value of the energy loss results to be larger than the mean binding energy for outer shell electrons <B>, an ionization occurs and a secondary electron is generated. The initial kinetic energy of the secondary electron is equal to the loss of energy minus the mean ionization energy. For lower transferred energy loss an excitation atomic electron cloud occurs, without the emission of secondary electrons.

6.1.1 Beam cross section

To properly model the cross section of the impinging primary electron beam two different distributions of the electrons in the spot were taken into account: the uniform distribution and the Gaussian distribution. In the next paragraph we present these two distributions.

Circular spot with uniform distribution: An incident beam with a spot diameter of 10 nm has to be mathematically modeled. Incidence positions in the plane, for each electron in the beam, were evaluated by generating two random numbers (r_1 and r_2), uniformly distributed in the interval (0,1). The two coordinates of the incidence position (x, y) were obtained as:

$$\begin{aligned} \theta &= 2\,\pi\,r_1 \\ x &= R\,\sqrt{r_2}\,\cos\theta \\ y &= R\,\sqrt{r_2}\,\sin\theta \end{aligned} \tag{6.1}$$

where R is equal to 5 nm. The resulting pattern, for 10^5 electrons, is the one reported in Fig. 6.1.

Circular spot with Gaussian distribution: To generate a Gaussian distributed circular beam spot (diameter of 10 nm), two random numbers (r_1 and r_2) have to be generated. In particular, r_1 is sampled uniformly in the interval (0,1), and r_2 is selected accordingly to the

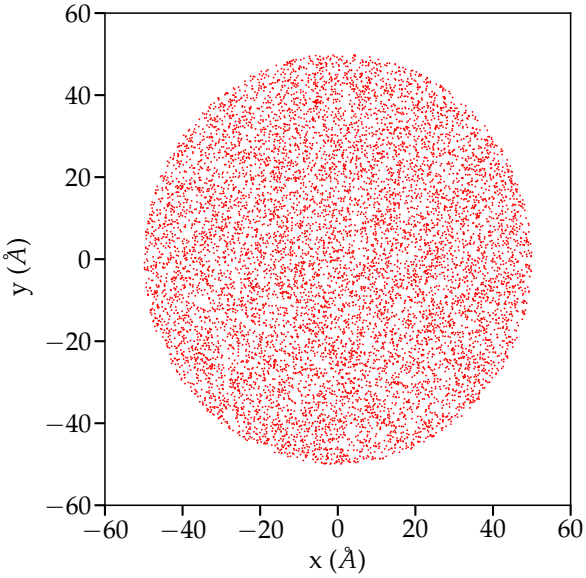

FIGURE 6.1: Beam section pattern.

following Gaussian distribution (Fig. 6.2a):

$$p(x) = \frac{1}{\sqrt{2\pi\sigma^2}} \exp\left(-\frac{x^2}{2\sigma^2}\right)$$

with $\sigma = 25$nm. The two coordinates of the incidence position (x, y) were obtained as:

$$\begin{aligned} \theta &= 2\ \pi\ r_1 \\ R &= r_2 \\ x &= R\ \cos\theta \\ y &= R\ \sin\theta \end{aligned} \tag{6.2}$$

The resulting pattern, for 10^5 electrons, are the one reported in Fig. 6.2(b).

6.1.2 Elastic scattering

The elastic scattering was described by the Mott theory [4] and it was evaluated starting from the Salvat potential [5] (See section 2.1.1 and Appedix A). The total elastic scattering cross section σ_{el} of SiO_2 was obtained by considering the stoichiometry of the compound. Indeed, it was computed as the sum of twice the σ_{el} of oxygen and once the σ_{el} of silicon. In Fig. 6.3 σ_{el} of oxygen, silicon and SiO_2 are reported.

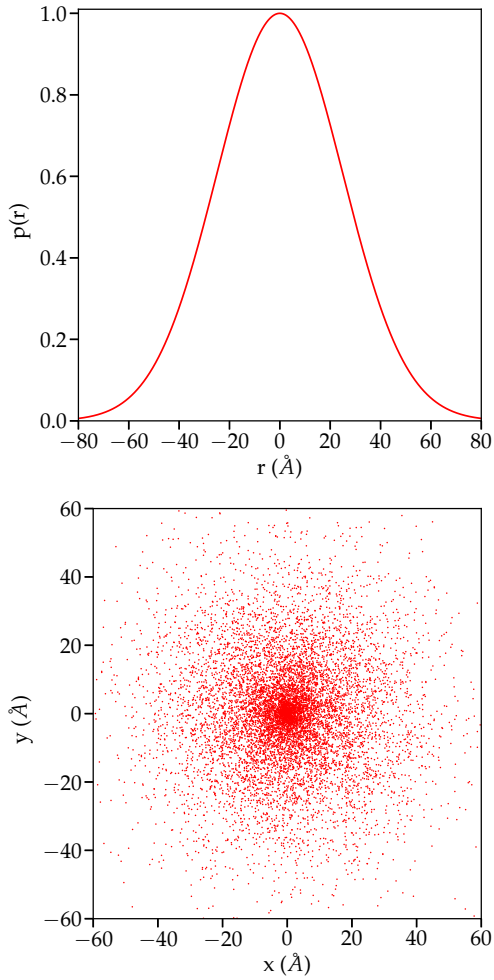

FIGURE 6.2: On the left the Gaussian distribution adopted to sample the value of the Radius, on the right the obtained beam section pattern.

The elastic scattering cross section should tend to zero for low kinetic energy because at lower energies the electron−phonon interaction should be the main elastic interaction. To correct the σ_{el} in that energy region the Ganachaud-Mokrani method was used (see section 2.1.1). Different values of the α parameter were tested and the resulting corrected σ_{el} are shown in Fig. 6.4.

To fix the proper value, tests of the secondary electron yield calculation were performed

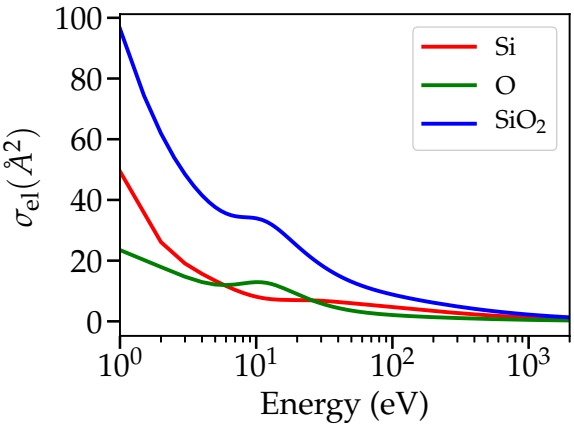

FIGURE 6.3: In red silicon, in green oxygen and in blue SiO_2 elastic scattering cross section.

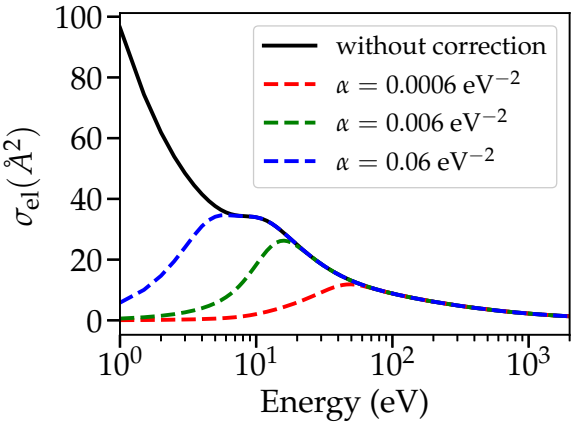

FIGURE 6.4: Elastic scattering cross sections: in blue as calculated, dashed lines with the Ganachaud-Mokrani correction with different values of the coefficient α.

(will be presented later) in order to reach the highest agreement with the experimental measurements. The value which allows the best agreement with the measurements is $\alpha = 0.06$ eV^{-2}. With this value of α, the values of elastic mean free path results to be of the order of the lattice parameters as can be seen in the following figures (Fig. 6.5). Starting from the corrected σ_{el}, the elastic scattering cumulative distribution probabilities [Eq. (2.13)] for different fixed kinetic energies were computed as a function of the scattering angle θ (see Fig. 6.6).

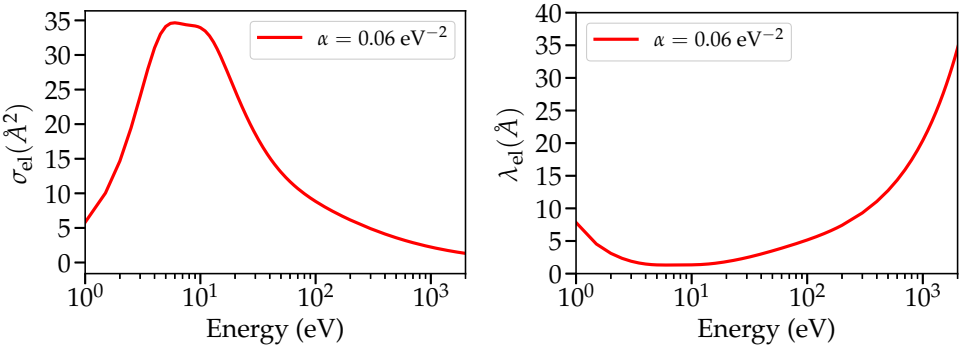

FIGURE 6.5: Elastic scattering cross section and elastic mean free path obtained with the application of the Ganachaud-Mokrani correction.

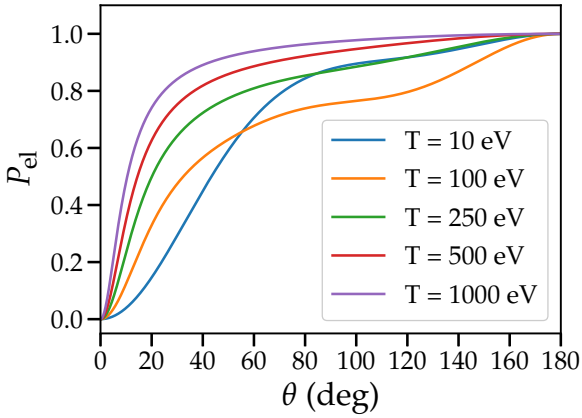

FIGURE 6.6: Elastic scattering cumulative distribution probability for a set of intial kinetic energies.

6.1.3 Inelastic scattering

Inelastic scattering cross sections were calculated according to [6] . The mean binding energy of SiO_2 has been estimated from data taken from Refs. [7, 8, 9, 10], by obtaining an average value of <B>=12.2 eV . The ELF has been taken from data from Palik [11].

From the calculated cross sections, the total inelastic mean free path is obtained, as shown in Fig. 6.7. The results is compared with experimental data by Murat et al. [12]and by Jung et al. [13] . Starting from the differential inelastic scattering cross sections, the cumulative inelastic probability distributions were computed as indicated in Eq.(2.20) for a set of kinetic energies. Fig.6.8 shows that the cumulative inelastic scattering probability distributions are

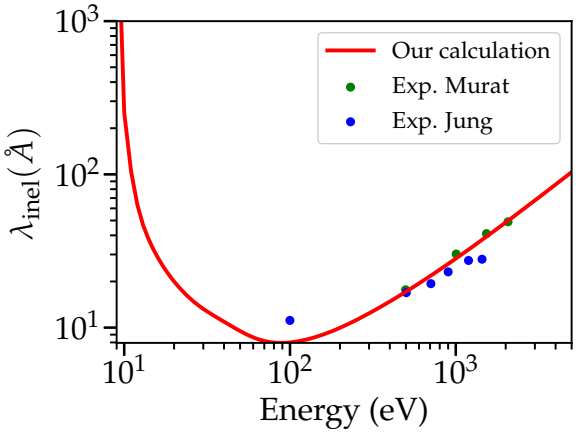

FIGURE 6.7: Calculated inelastic mean free path as a function of the kinetic energy in red compared to experimental data by Murat [12] and by Jung [13].

rather similar for electrons with energies larger than 1 keV. The differences appear at low electron energies.

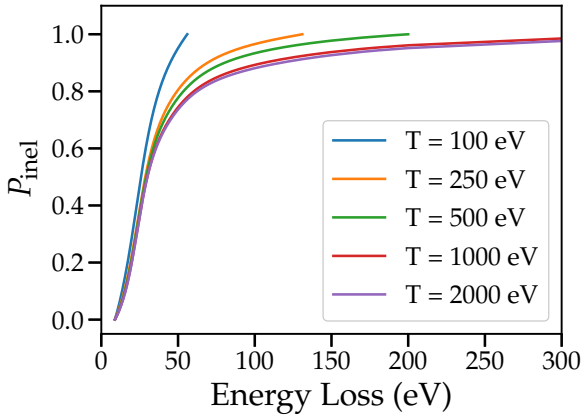

FIGURE 6.8: Inelastic scattering cumulative probability distributions as a function of the energy loss for a set of kinetic energies.

6.1.4 Electron Phonon interaction

The electron-phonon interaction was modeled using the Frölich theory [14] as described in section 2.1.3. In the computation of the relative mean free path [λ_{ph} Eq. (2.21)] ϵ_0 and ϵ_∞, respectively the static and the high frequency dielectric constants, were set to 3.84 and 2.24, as reported in [3]. The simulations were realized by fixing the temperature T to 273°K. After a series of tests and comparisons with experimental data of secondary electron yields, it was found that the value of the average mean energy W_{ph} which ensures the highest agreement with the experimental data is 0.15 eV.

6.1.5 Scattering probabilities

The mean free path, which takes into account all the possible interactions, is computed in this case as:

$$\frac{1}{\lambda} = \frac{1}{\lambda_{el}} + \frac{1}{\lambda_{inel}} + \frac{1}{\lambda_{ph}} \tag{6.3}$$

The probabilities to undergo each kind of interaction are evaluated by applying these relations:

$$\begin{aligned} p_{el} &= \frac{\lambda}{\lambda_{el}} \\ p_{inel} &= \frac{\lambda}{\lambda_{inel}} \\ p_{ph} &= \frac{\lambda}{\lambda_{ph}} \end{aligned} \tag{6.4}$$

The various scattering probabilities are reported, as a function of the kinetic energy, in Fig. 6.9. As a result of the application of the Ganachaud - Mokrani correction, the electron-phonons interaction becomes significant in the low energy range, to detriment of elastic scattering.

6.2 Results of Monte Carlo simulations

6.2.1 Validation of the Code

Before considering high energy electron beams, simulations at low beam energy were realized in order to validate the model. With this aim, simulated REEL spectra and secondary electron yields were compared to experimental data to validate the code and determine optimal parameters for the accurate description of each kind of interaction.

Reflection Electron Energy Loss spectra

REEL spectra were simulated by setting the number of electrons in the beam equal to 10^9. Different initial kinetic energies were considered and the results were compared with our experimental data [15, 16] in Fig. 6.10. The data are normalized to a common height of the main plasmon peak.

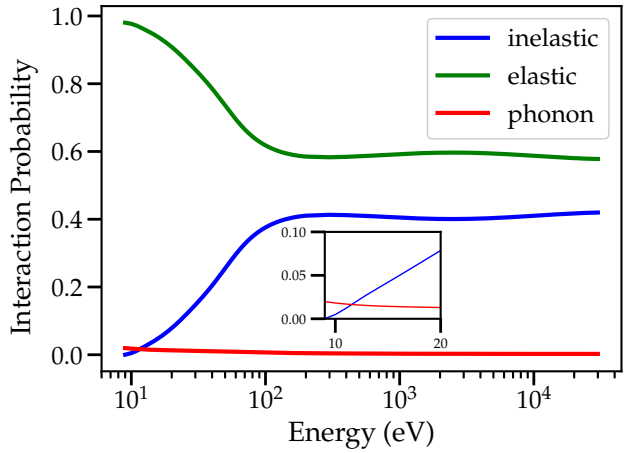

FIGURE 6.9: Scattering probabilities as a function of the kinetic energy.

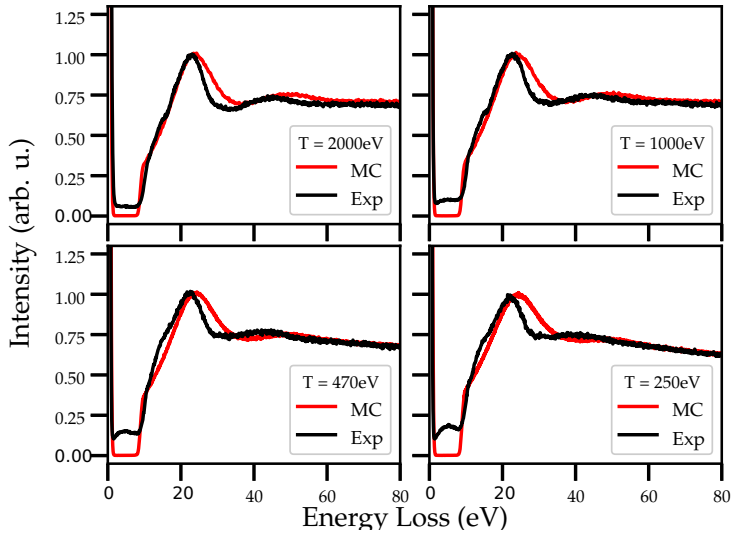

FIGURE 6.10: Reflection Electron Energy Loss spectra of SiO_2 at different kinetic energy of the beam. In red simulated spectra and in black experimental spectra [15, 16]. The data are normalized to a common height of the main plasmon peak.

These results show a good agreement between simulated and measured spectra. Even if the MC main plasmon peak results to be slightly wider than the experimental one, the part of the spectra corresponding to multiple plasmon excitations is well reproduced by the simulated results.

Secondary electron spectra

A complete electron emission energy spectra was obtained by generating 10^6 electron trajectories and by setting the beam energy at 100 eV. The simulated spectrum is compared in Fig. 6.11 to another theoretical spectrum achieved by Schreiber and Fitting [3]. This latter is in turn in agreement with experimental data by Fitting at al. [17].

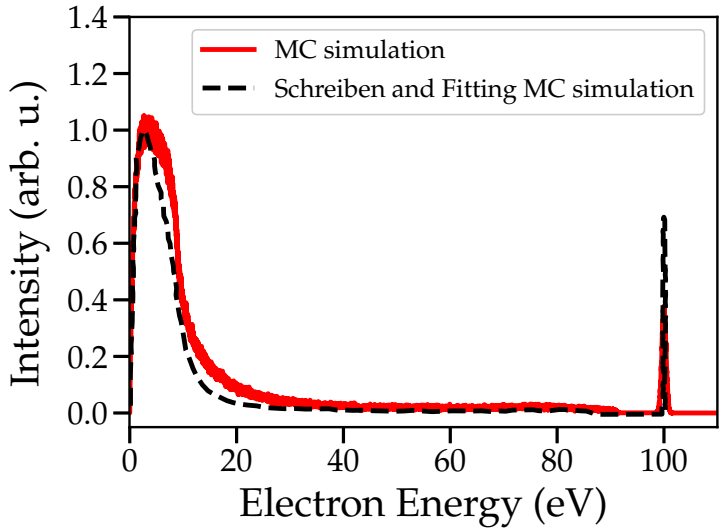

FIGURE 6.11: Energy spectrum of SiO_2 for an initial kinetic energy of 100 eV. In red our calculated spectrum, in black the calculated spectrum by Schreiber and Fitting [3]. The data are normalized to a common height of the secondary electron emission peak.

By taking into account the low resolution of the reference theoretical spectrum, a good agreement can be found between the two theoretical line shapes.

Secondary electron yield

Monte Carlo simulations were performed to calculate the secondary electron yield of SiO_2. In this case, to assure the statistical significance of the calculation, the number of trajectories was set to 10^5. In Fig. 6.12 results of different runs carried out using different values of the Ganachaud-Mokrani coefficient are reported, maintaining fixed the value of the energy loss W_{ph} due to the electron-phonon interaction to 0.15 eV. The curves thus obtained are compared

with numerical results of Schreiber and Fitting [3] and the experimental data by Glavatskikh and Yi [18, 19].

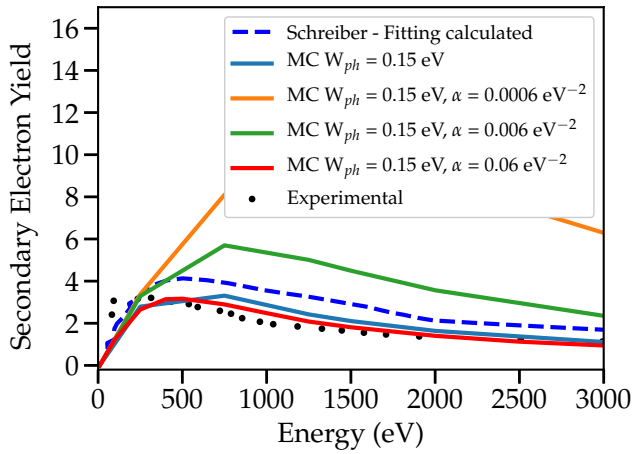

FIGURE 6.12: Secondary electron yield of SiO_2. In green the curve obtained without the Ganchaud-Mokrani correction. The other curves were obtained with different values of the α parameter of the Ganchaud-Mokrani correction. The dashed blue line reports the calculated curve by Schreiber and Fitting [3] and the black dotted curve represents experimental data by Glavatskikh and Yi [18, 19].

By choosing the value of α equal to 0.06 eV^{-2}, a good agreement is reached with both experimental and computational reference data.

Fig. 6.13 shows the results achieved by changing the values of the energy loss W_{ph} due to the electron-phonon interaction and by maintaining constant the value of the Ganachaud-Mokrani coefficient α to 0.06 eV^{-2}.

From the comparison with experimental data reported in Ref.[18, 19], it was determined that the proper value of α is 0.06 eV^{-2} and the proper value of W_{ph} is 0.15 eV. By setting these parameters, characteristic of the sample, the optimized secondary electron yield curve is the one reported in Fig. 6.14. This calculated signal shows the same shape of the Schreiber and Fitting [3] theoretical results. Schreiber and Fitting reported that their calculated curve resulted to be higher than experimental data. Our calculated curve is in agreement with the experimental data by Glavatskikh and Yi [18, 19].

The MC model was so validated for this target and can be applied to perform speculative simulations, in order to acquire quantitative information about the action of primary and secondary electrons in the FEDIB process.

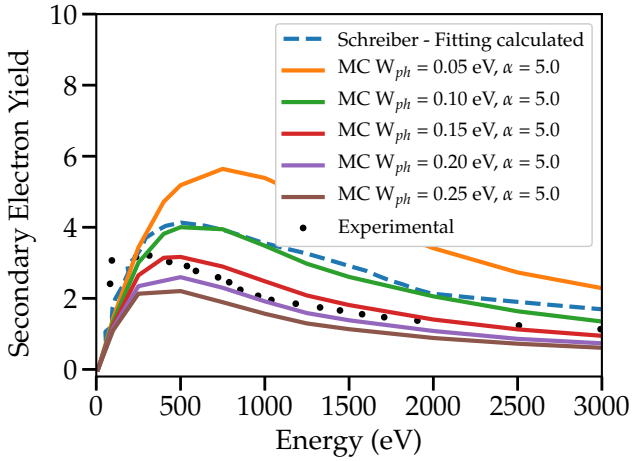

FIGURE 6.13: Secondary electron yield of SiO_2. Continuous curves were obtained with different values of the W_{ph} parameter and by maintaing fixed the value of α parameter to 5.0. The dashed blue line reports the calculated curve by Schreiber and Fitting [3] and the black dotted curve represents experimental data by Glavatskikh and Yi [18, 19].

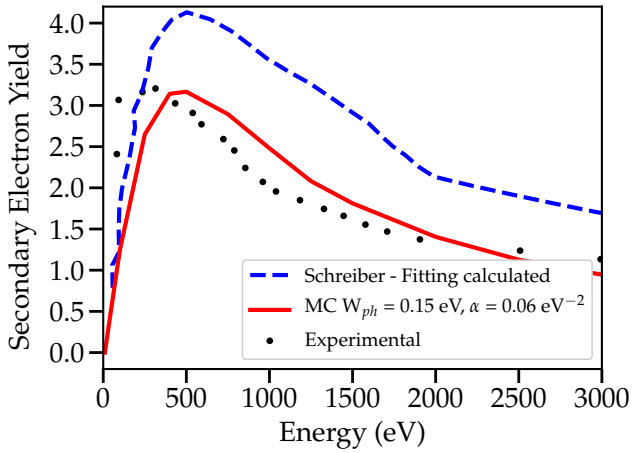

FIGURE 6.14: Secondary electron yield of SiO_2. In solid line our calculated curve. In dashed line the calculated curve by Schreiber and Fitting [3]. In points the experimental data by Glavatskikh and Yi [18, 19].

6.2.2 High energy simulations

With the aim to understand the general behaviour of primary and secondary electrons traveling in SiO_2, different sets of simulations were performed by choosing the beam energy in the range between 1 keV and 30 keV. The incident beam was modeled with a uniform spot distribution and composed by N = 10^7 or 10^8, depending on the scope, primary electrons. In particular, the study on secondary electrons position generation and energy deposition was carried out. The kinetic energy and the distance of the emission position from the center of the incident beam were recorded for each emitted electron and, by analyzing these records, energy spectra and distance distribution spectra were realized.

Spectra

The emission energy spectra obtained for different initial kinetic energies, starting from 10^7 primary electrons, are shown in Fig. 6.15.

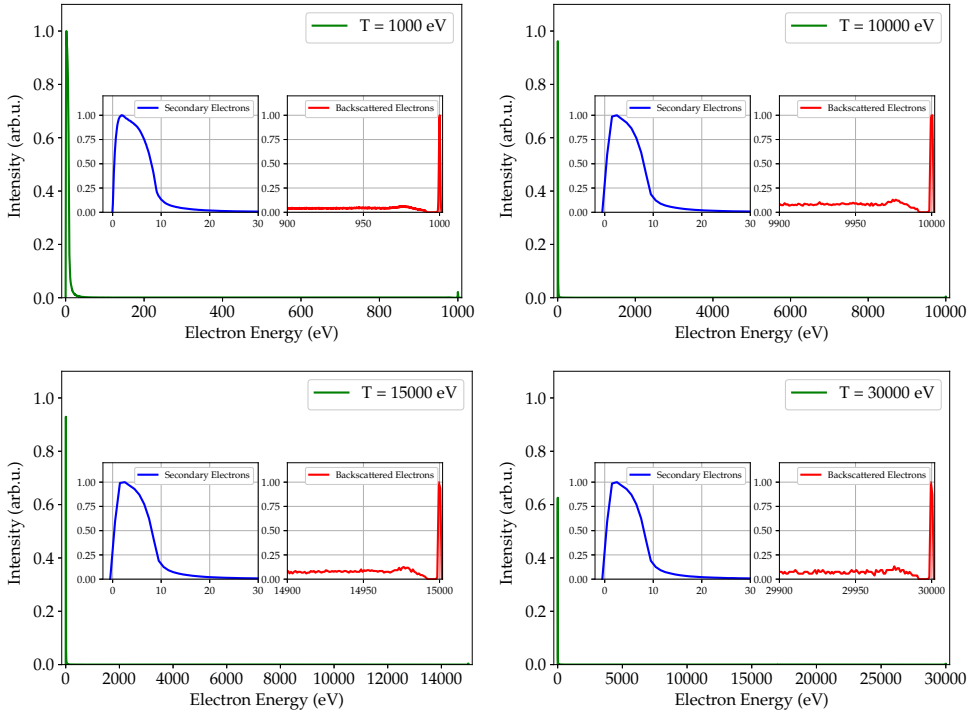

FIGURE 6.15: Calculated energy emission spectra obtained for different initial kinetic energies. In green the full spectrum is reported. In blue the secondary electron emission peak is shown. In red the back scattered emission spectra is presented. In each plot the data are normalized to the highest peak value.

From these results we see that the variation of the initial beam energy does not influence the shape of the secondary electron emission peak. The intensity of the secondary electron emission peak remain progressively higher than the elastic peak.

Secondary electron generation yield

The secondary electron generation yield is the total number of generated secondary electrons divided by the number of primary electrons. In is worth noting that it is different from the secondary electron yield, which accounts for emitted electrons. The secondary electron generation yield is not measurable experimentally, it was evaluated with simulations, for a set of different beam energies. The results are reported in Fig. 6.16.

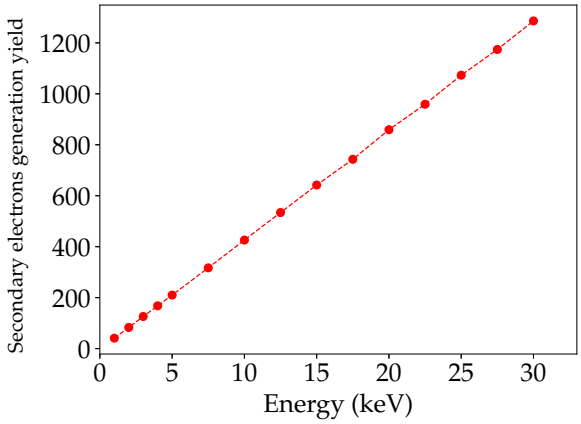

FIGURE 6.16: Secondary electron generation yield as a function of the initial kinetic energy of the beam.

The figure shows a linear trend: the secondary electron generation is enhanced by the increase of the beam energy. The depths of the positions in which the secondary electrons are generated were recorded. The distributions of depth position are reported in Fig. 6.17, and the positions at which the distributions are maxima were indicated in Fig. 6.18 as a function of beam energy.

Also the depth position increases with the increase of the beam energy. Thus higher the beam energy higher the depth generation position and the number of secondary electrons which are generated. However, the number of secondary electrons which manage to escape from the target decreases as the beam energy increases. This is clearly shown by Fig. 6.19 where the ratio between the number of emitted secondary electrons and the number of generated secondary electrons is reported. So, a high energy beam produces a big drop of generated secondary electrons, but electrons have to travel a long way in order to emerge. In this way they continue performing interactions, losing energy till their stop or they emerge.

The initial kinetic energy assigned to each generated secondary electrons was also recorded. The energy distributions are reported in Fig. 6.20 for different beam energies. The distributions

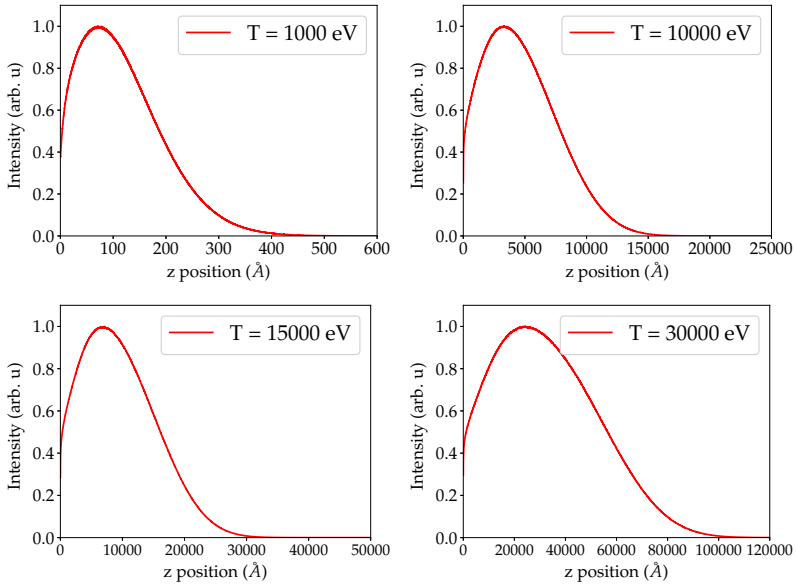

FIGURE 6.17: Secondary electrons generation position depth distributions for different values of the beam energy.

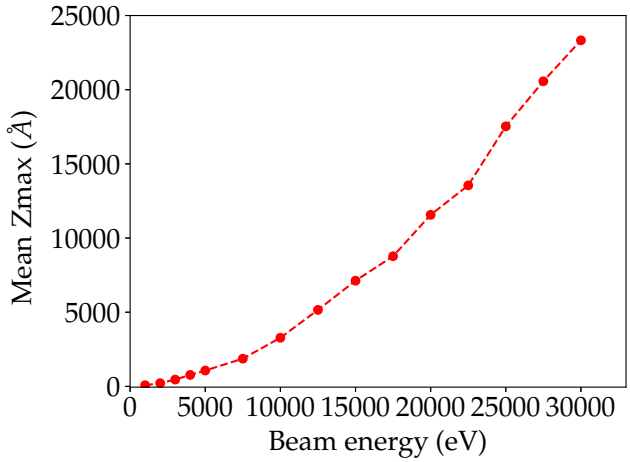

FIGURE 6.18: Position depths correspondent to the maximum of position depth distribution as a function of beam energy.

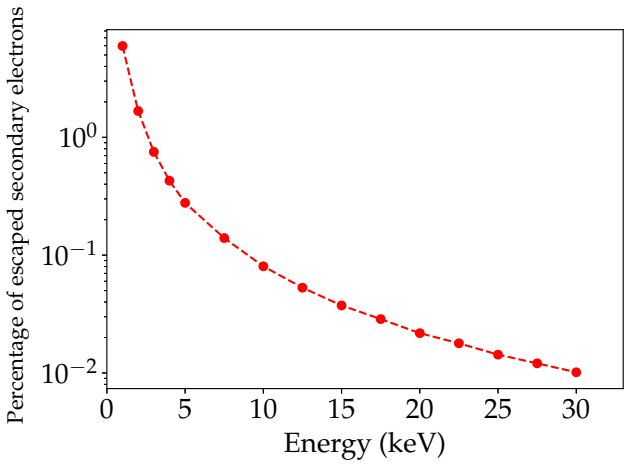

FIGURE 6.19: Percentage of the ratio between the number of emitted secondary electrons and the number of generated secondary electrons, as a function of the beam energy.

evidence the same trend as the cumulative inelastic probability distributions, related to peak positions in the ELF function. The MC model recognizes the nature of the electron, whether it

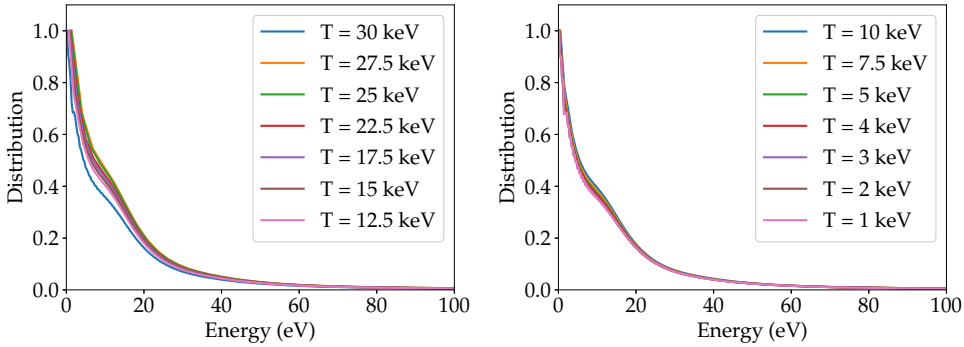

FIGURE 6.20: Intial kinetic energy of generated secondary electrons distributions for different values of the beam energies.

is a primary beam electron or a generated one, thus the yields considering this difference were also evaluated. The back-scattering coefficient is the ratio between the back-scattered electrons and the number of the electrons in the beam. The secondary electrons yield is the ratio between the emitted secondary electrons and number of the electrons in the beam. The total yield is the

sum of the two yields. These three features as a function of initial beam energies are reported in Fig. 6.21.

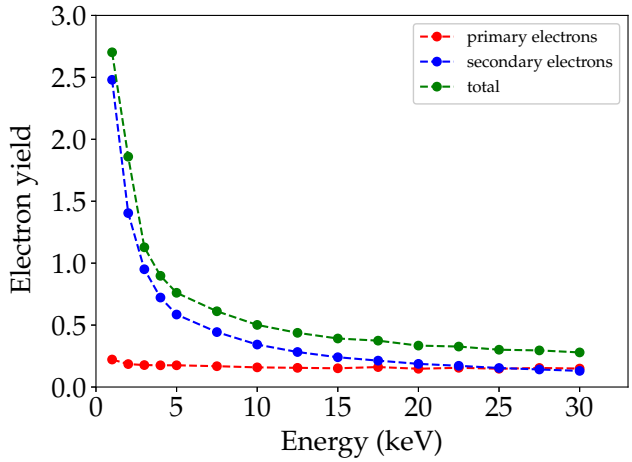

FIGURE 6.21: Electrons yields as a function of the beam energy. In red the primary electrons yield, in blue the secondary electrons yield and in green the total yield.

In light of these results, the contribution of the primary electron yield can be considered constant, while the contribution of the secondary electron yield decreases as the beam energy increases.

Emission position distribution

The position emission distance from the center of the incidence beam was recorded for each emitted electron. Then, these data were analyzed counting the number of electrons emitted in an interval centered at a specific value of the distance (Fig. 6.22 , left side). These counts were also normalized dividing by the area of the annulus relative to the specific value of the distance, in order to obtain a flux. Being dR the interval between two subsequent distance values in the set and D the specific value of the distance, the annulus area was calculated as:

$$Area = \pi[(D + dR/2)^2 - (D - dR/2)^2] \tag{6.5}$$

and are shown in Fig. 6.22 (right side).

The curves reporting counts show a peak around 50 Å which corresponds to the radius of the incident beam section. Moreover, at radial distances larger that 10 times the initial radius of the beam (at 500 Å), the number of emitted electrons is almost 3 order of magnitude lower. The normalized curves, for a distance lower than 50 Å, which corresponds to the beam radius, are constant. This is due to the uniform distribution of incident positions in the beam spot. Moreover, we note that the distributions reach higher distances for higher kinetic energy of the beam.

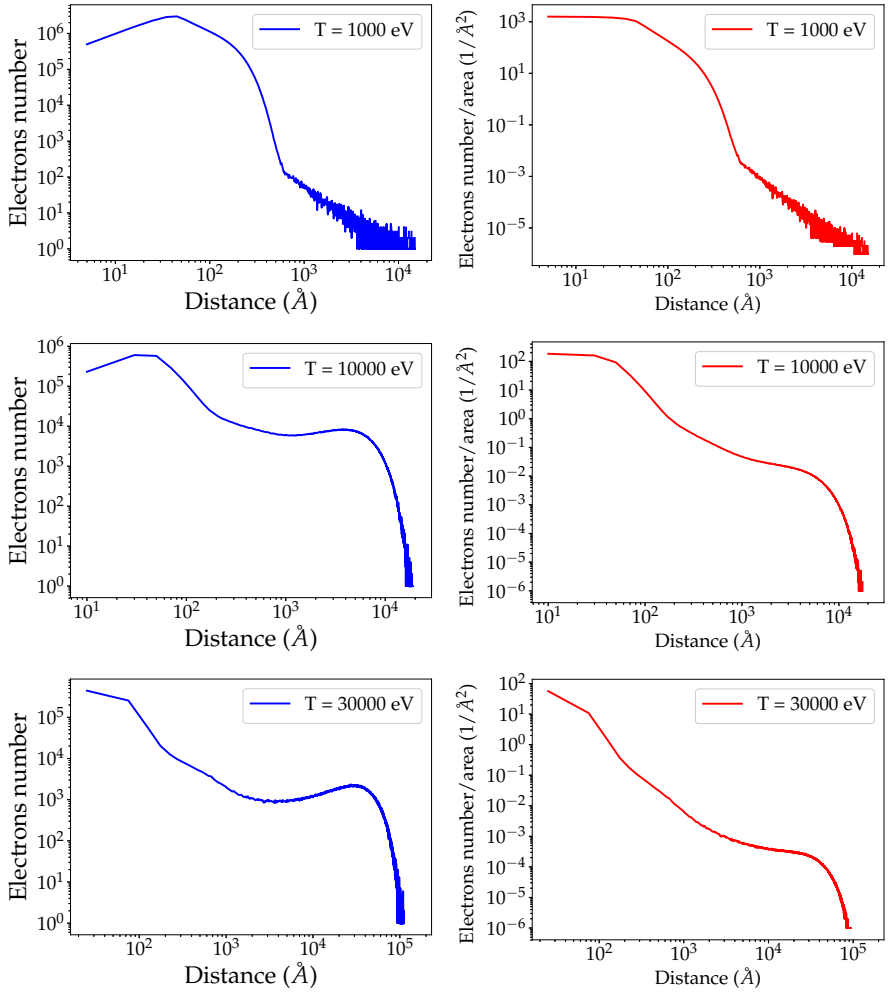

FIGURE 6.22: Emission position distance distributions for different initial beam energies. Figures on the left (in blue) report the number of emitted electrons with the specified distance from the center of the beam. Plots on the right (in red) report the data of the pictures on the left side normalized respect to the annulus area.

Emission angle distribution

The value of electron emission angles with respect to the normal direction to the target surface were acquired. Then the distributions were elaborated and reported in Fig. 6.23 for different kinetic energies. From this figure it can be notice that the distributions remain substantially

constant for different initial kinetic energies of the beam.

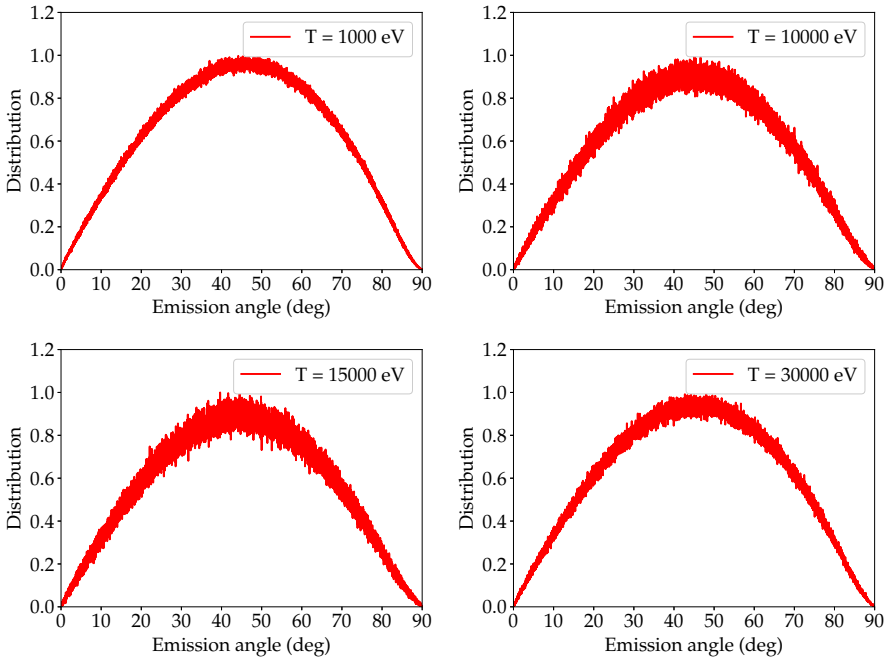

FIGURE 6.23: Emission angle distributions for different values of the beam energy.

Energy and position spectra

These results were carried out by considering 10^8 primary electrons in the impinging beam.

Beam energy equal to 1keV The data were analyzed by setting the energy bin dE equal to 0.1 eV and the distance bin dR to 10 Å. The maximum distance taken into account for the sampling is 10000 Å. To obtain the spectra the electrons were counted depending on their kinetic energy and emission position (Fig. 6.24). Then these values were divided by the value of the energy bin dE, by the number of sent electrons N and by the area of the annulus. These results are shown in Fig. 6.25. From the complete emission spectra, the consistent difference in intensity between secondary electron emission peaks and elastic peaks is evident. The normalized curves, concerning the backscattered electrons, show peaks related to the excitation of plasmon oscillations. By normalizing the data, the profile of secondary electron peaks in the distance direction is the same reported in the previous investigation shown in Fig. 6.22.

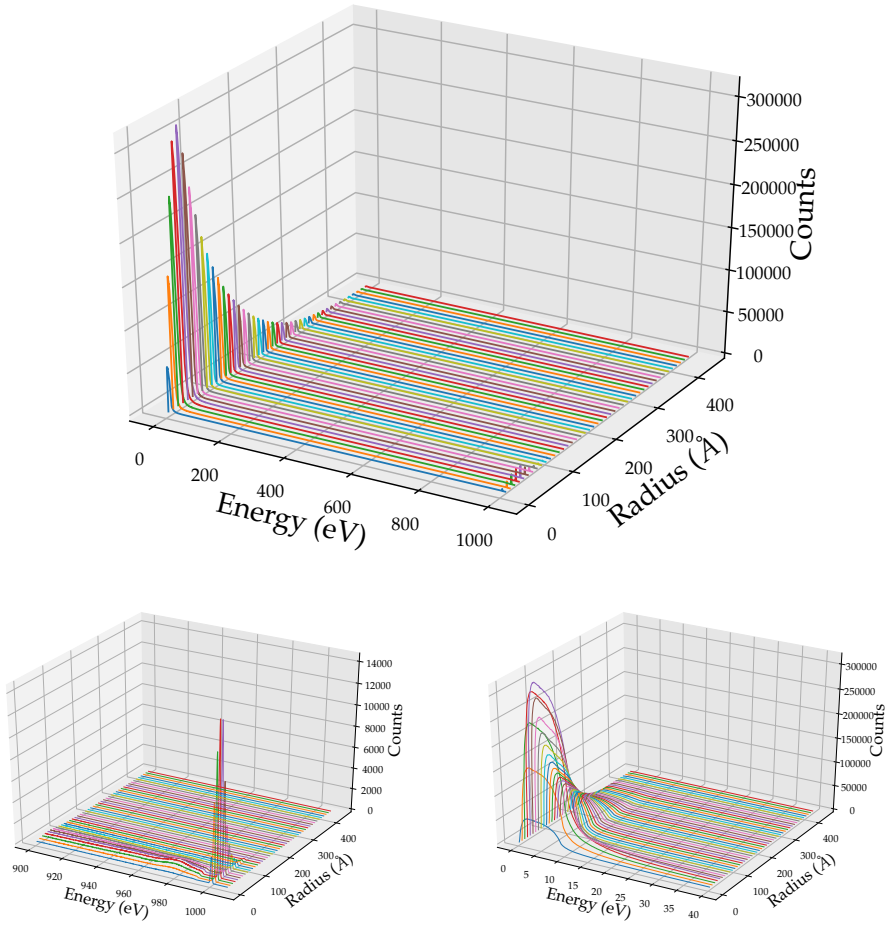

FIGURE 6.24: In the upper panel the full spectra are reported. In these the counts are reported as a function of emission distance and as a function of emission energy. In the cetral panel the REEL portion of spectra is zoomed, and in the bottom panel SE emission spectra are reported.

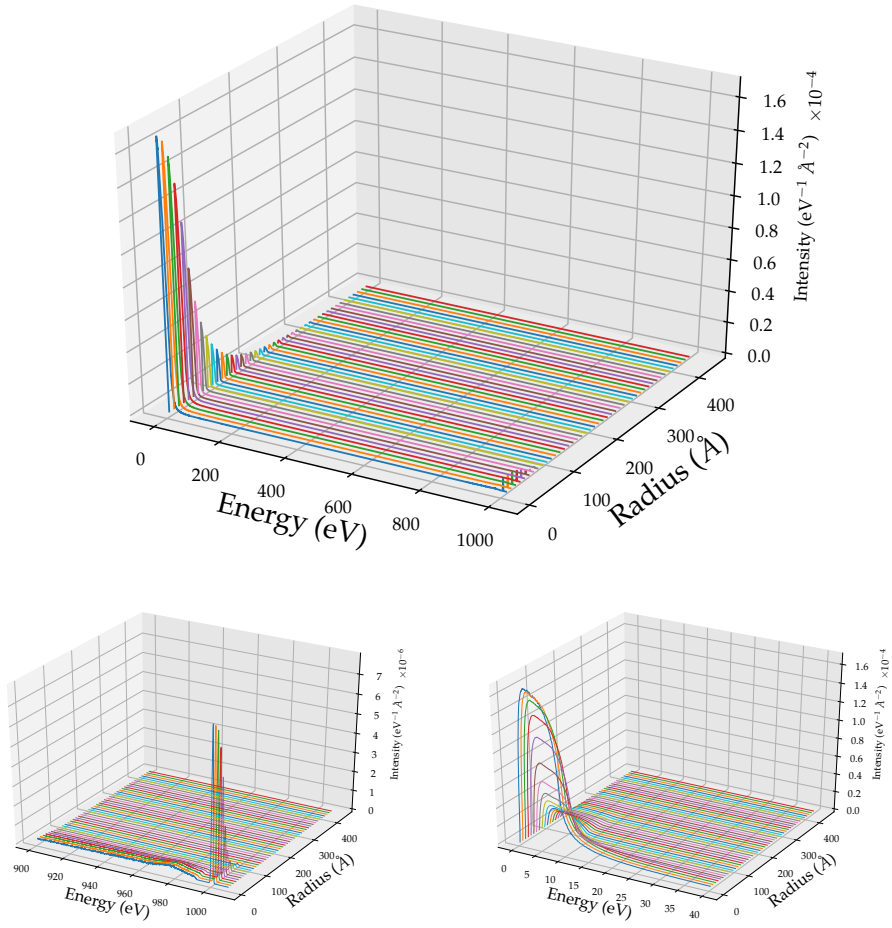

FIGURE 6.25: In the upper panel the full spectra are reported. In these the normalized counts are reported as a function of emission distance and as a function of emission energy. In the central panel the REEL portion of spectra is zoomed, and in the bottom panel SE emission spectra are reported.

Beam energy equal to 30keV The data were analyzed by setting the energy bin dE equal to 1 eV and the distance bin dR to 10 Å. The maximum distance taken into account for the sampling is 30000 Å. The energy and emission position spectra are reported in Fig. 6.26. The normalized spectra are then shown in Fig. 6.27. In light of these results, we notice that the emission of secondary electrons is concentrated in a narrow radial distance and that the backscattered electrons are emitted at higher distances. Secondary electrons are emitted with an energy lower than 50 eV. By considering the simple counts result, the secondary electron emission peak reaches its maximum value around the distance equal than the radius of the beam, as can be expected. For normalized counts, the secondary electrons peak value remains constant till distance equal the beam spot radius, then progressively decreases. The normalized data were passed to the IDMD model, to consider the charge transfer to precursor molecules represented by different kind of emitted electrons.

Simulations details

In the following table characteristic quantities of simulations and data analysis are reported. These features were recorded by considering the beam composed by 10^7 primary electrons.

Beam energy (eV)	N° CPUs	computational time	N° emitted electrons	Maximum distance (Å)	dR (Å)	dE (eV)
1000	2048	00:16:22	27017149	2.53×10^8	10.0	0.1
10000	2048	03:45:53	5014371	3.12×10^{10}	20.0	1
15000	2048	02:38:15	3916981	1.40×10^8	20.0	1
30000	2048	05:15:18	2793844	2.63×10^6	50.0	1

TABLE 6.2: Characteristic quantities of Monte Carlo simulations.

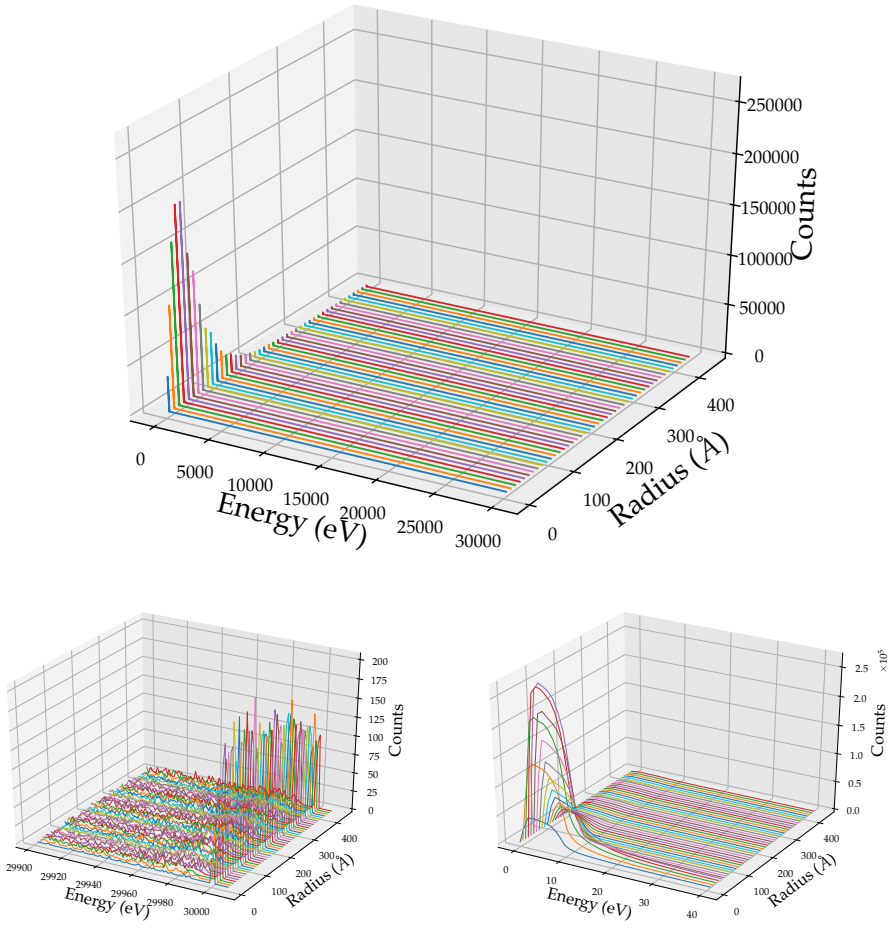

FIGURE 6.26: In the upper panel the full spectra are reported. In these the counts are reported as a function of emission distance and as a function of emission energy. In the central panel the REEL portion of spectra is zoomed, and in the bottom panel SE emission spectra are reported.

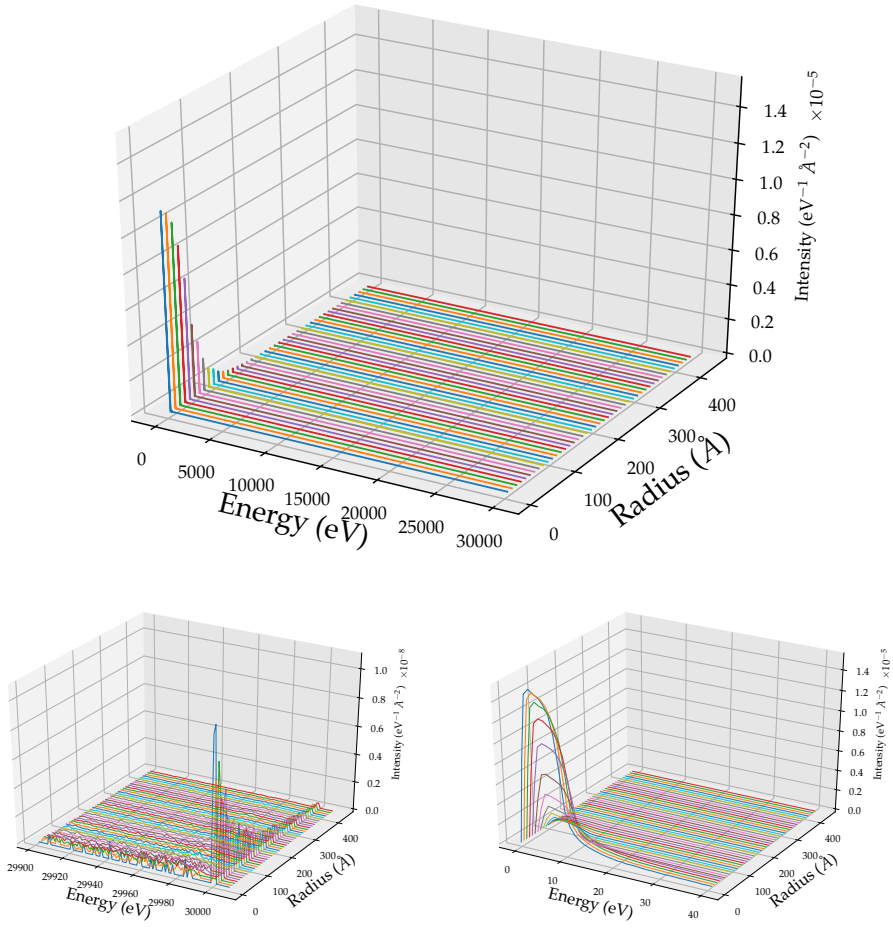

FIGURE 6.27: In the upper panel the full spectra are reported. In these the normalized counts are reported as a function of emission distance and as a function of emission energy. In the central panel the REEL portion of spectra is zoomed, and in the bottom panel SE emission spectra are reported.

Gaussian distributed beam pattern

A simulation with the beam energy set at 30 keV and the beam spot realized with a Gaussian distribution of the radius was realized. The simulation were realized by initially considering 10^7 primary electrons.

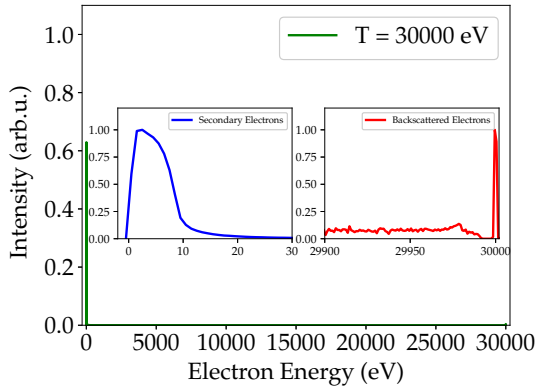

FIGURE 6.28: Calculated energy emission spectra obtained for initial kinetic energy equal to 30keV and a Gaussian distributed beam pattern. In green the full spectrum is reported. In blue the secondary electron emission peak is shown. In red the backscattered emission spectra is presented. In each plot the data are normalized to the highest peak value.

Emitted electrons were counted as a function of their emission distance from the beam center. The bin of the sampling dR was set equal to 10Å for a total number of bins equal to 3000. The emission distance spectrum is reported in Fig. 6.29. In this case, the normalized

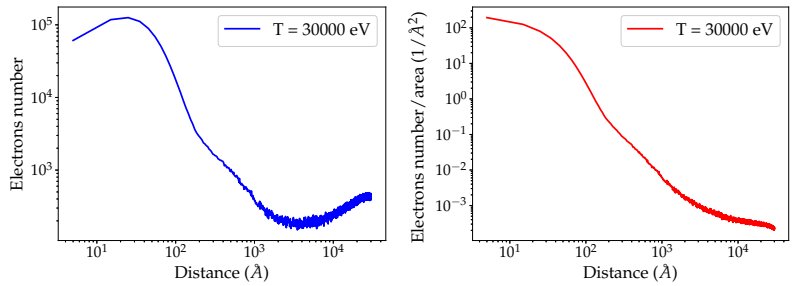

FIGURE 6.29: Emission position distance distributions: the figure on the left (in blue) reports the number of emitted electrons with the specified distance from the centre of the beam. the plot on the right (in red) report the data of the pictures on the left side normalized respect to the annulus area.

distance emission distribution presents a decreasing shape also for low distance value, due to the Gaussian beam spot distribution. The energy and emission position spectra are reported in Fig. 6.30. The normalized spectra are then shown in Fig. 6.31.
It is worth noting that, compared to previous results at 30 keV achieved with a constant distribution, the number of primary electrons in the beam is one order lower and this justifies the more noisy signals. However the overall behaviour of emitted electrons is not substantially affected by the variation of beam spot distribution.

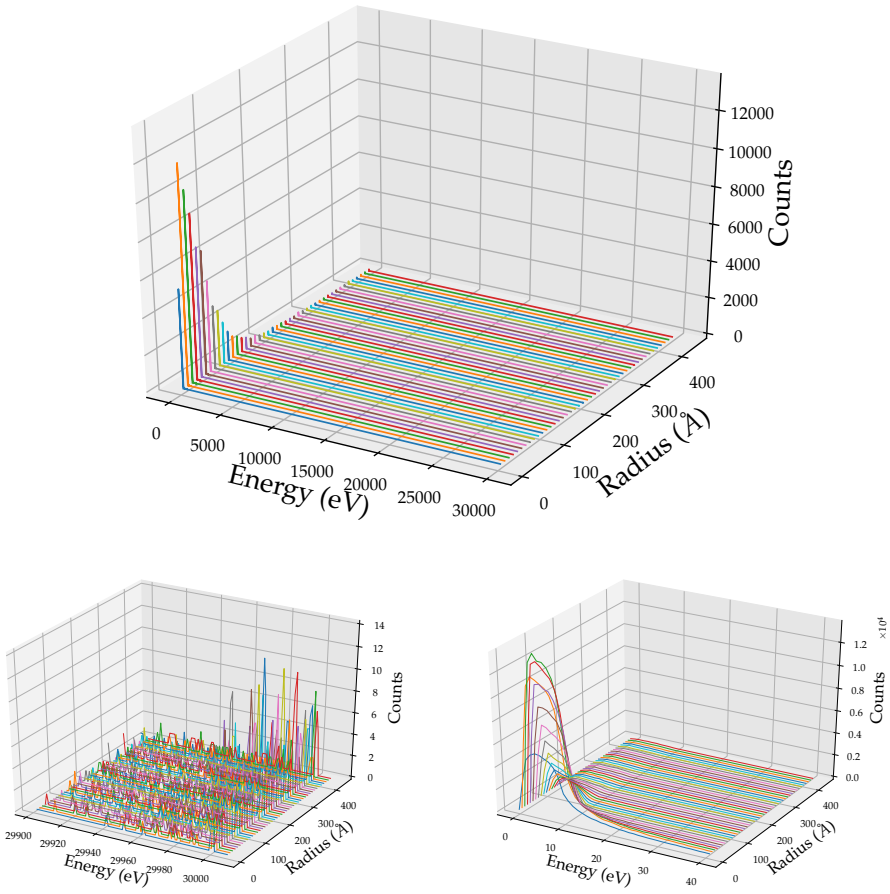

FIGURE 6.30: In the left panel the full spectra are reported. The initial kinetic energy is equal to 30 keV. The counts are reported as a function of emission distance and as a function of emission energy. In the central panel the REEL portion of spectra is zoomed, and in the right panel SE emission spectra are reported.

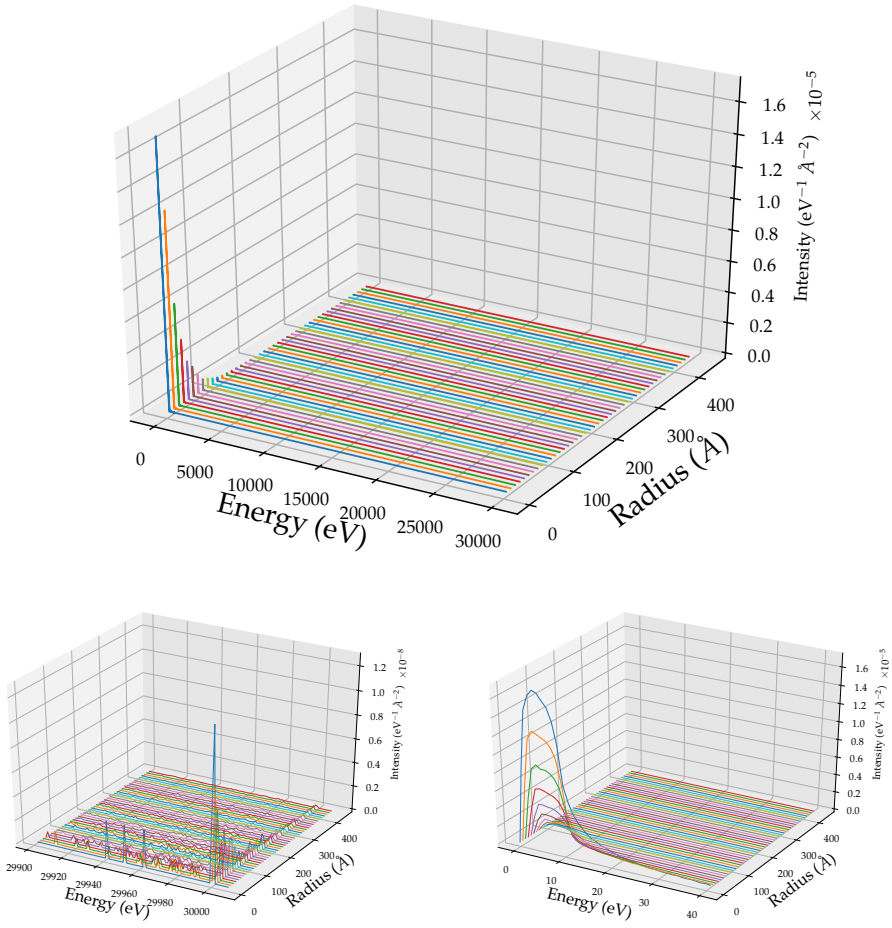

FIGURE 6.31: In the left panel the full spectra are reported, the initial kinetic energy is equal to 30keV. In these the normalized counts are reported as a function of emission distance and as a function of emission energy. In the central panel the REEL portion of spectra is zoomed, and in the right panel SE emission spectra are reported.

6.3 Conclusions

In this chapter, the electron emission from a bulk of SiO_2 bombarded by a high energy electron beam was analyzed in details. Initially, the MC procedure was tested by comparing calculated emission spectra and secondary electrons yield to experimental measurements. A remarkably good agreement was found between calculated and measured spectra and yield values. This allowed further studies focused on the secondary electron generation, the consistency of the avalanches, their generation depth and initial energy distribution. High energy beam involves a significant generation of secondary electrons. However, given the huge depth at which they are generated, only a decreasing part of them manage to reach the surface and be emitted. Thus, we found that the quantity of emitted electrons decrease as the the beam energy increases. Further investigations were aimed at the acquisition of energy and position emission distributions of electrons for high energy beam. By feeding IDMD technique with these results, might allow understanding the overall processes due to the FEDIB deposition technique, with the aim to provide the experimentalists with recommendations about optimized beam conditions.

Bibliography

[1] R. M. Thorman, T. P. Ragesh Kumar, D. Howard Fairbrother, O. Ingólfsson, The role of low-energy electrons in focused electron beam induced deposition: Four case studies of representative precursors, Beilstein Journal of Nanotechnology 6 (1) (2015) 1904–1926.

[2] G. B. Sushko, I. A. Solov'yov, A. V. Solov'yov, Molecular dynamics for irradiation driven chemistry: application to the FEBID process*, The European Physical Journal D 70 (10) (2016) 217.

[3] E. Schreiber, H.-J. Fitting, Monte carlo simulation of secondary electron emission from the insulator SiO_2, Journal of Electron Spectroscopy and Related Phenomena 124 (1) (2002) 25–37.

[4] N. Mott, The scattering of fast electrons by atomic nuclei, Proceedings of the Royal Society of London. Series A, Containing Papers of a Mathematical and Physical Character 124 (794) (1929) 425.

[5] F. Salvat, J. Martinez, R. Mayol, J. Parellada, Analytical Dirac-Hartree-Fock-Slater screening function for atoms (Z=1–92), Phys. Rev. A 36 (1987) 467–474.

[6] P. de Vera, R. Garcia-Molina, I. Abril, A. V. Solov'yov, Semiempirical Model for the Ion Impact Ionization of Complex Biological Media, Physical Review Letters 110 (2013) 148104.

[7] S. K. Nayak, B. K. Rao, S. N. Khanna, P. Jena, Atomic and electronic structure of neutral and charged SinOm clusters, Journal of Chemical Physics 109 (4) (1998) 1245–1250.

[8] K. N. Joshipura, B. G. Vaishnav, S. Gangopadhyay, Electron impact ionization cross-sections of plasma relevant and astrophysical silicon compounds: SiH4, Si2H6, Si(CH3)4, SiO, SiO2, SiN and SiS, International Journal of Mass Spectrometry 261 (2-3) (2007) 146–151.

[9] O. Kostko, M. Ahmed, R. B. Metz, Vacuum-ultraviolet photoionization measurement and ab initio calculation of the ionization energy of gas-phase SiO_2, Journal of Physical Chemistry A 113 (7) (2009) 1225–1230.

[10] L. Dan-Dan, Z. Hong, Photoabsorption Spectra of (SiO 2) n (n $\leq$ 5) Clusters on the Basis of Time-Dependent Density Functional Theory, Chinese Physics Letters 27 (9) (2010) 093601.

[11] E. D. Palik, G. Ghosh, The Electronic Handbook of Optical Constants of Solids, Academic Press, San Diego, 1999.

[12] M. Murat, A. Akkerman, J. Barak, Spatial distribution of electron-hole pairs induced by electrons and protons in sio/sub 2, IEEE transactions on nuclear science 51 (6) (2004) 3211–3218.

[13] R. Jung, J. Lee, G. Orosz, A. Sulyok, G. Zsolt, M. Menyhard, Determination of effective electron inelastic mean free paths in sio2 and si3n4 using a si reference, Surface science 543 (1-3) (2003) 153–161.

[14] H. Fröhlich, Electrons in lattice fields, Advances in Physics 3 (11) (1954) 325–361.

[15] M. Filippi, L. Calliari, M. Dapor, Joint experimental and computational study of silicon dioxide electron energy loss spectra, Physical Review B 75 (12) (2007) 125406.

[16] M. Dapor, Energy loss spectra of low primary energy ($E_0 \leq$1 keV) electrons backscattered by silicon dioxide, Surface science 600 (20) (2006) 4728–4734.

[17] H.-J. Fitting, J. Boyde, J. Reinhardt, Monte-carlo approach of electron emission from SiO_2, physica status solidi (a) 81 (1) (1984) 323–332.

[18] I. Glavatskikh, V. Kortov, H.-J. Fitting, Self-consistent electrical charging of insulating layers and metal-insulator-semiconductor structures, Journal of Applied Physics 89 (1) (2001) 440–448.

[19] W. Yi, T. Jeong, S. Yu, J. Lee, S. Jin, J. Heo, J. Kim, Study of the secondary-electron emission from thermally grown SiO_2 films on Si, Thin Solid Films 397 (1) (2001) 170–175.

Chapter 7

Deep investigation of secondary electron emission spectra of P3HT

7.1 Introduction

Understanding nanoscale molecular ordering within organic electronic materials is a crucial factor in building better organic electronic devices. In this chapter, we present secondary electron (SE) spectroscopy to probing molecular ordering in P3HT. Early work in the SE spectroscopy of organic materials showed that peaks in the SE spectrum emitted from graphite reflect the energy levels of conduction band minima [1]. More recently, the influence of sample doping [2] and the sample's bonding structure[8] of SE spectral features have also been explored. However, the process of SE generation, transport and subsequent emission is highly complex, involving a 'cascade' of interactions with sample atoms, electrons, phonons and trap sites, each of which can influence the properties of an emitted SE [3]. As a result, the energy distribution of emitted SEs results from a complex convolution of various material and electronic properties. In this work, we investigate the material properties that influence the shape of the SE spectrum emitted from poly(3-hexylthiophene) (P3HT), a semicrystalline polymer with organic electronic applications. P3HT films are an ideal test subject for investigating SE emissions, as the electron transport and emission properties are dependent on molecular ordering, and controllable with film processing [4, 5, 6, 7] . Further, P3HT is a popular conjugated polymer with applications across the field of organic electronics [8]. In particular, we demonstrate that crystalline content in a P3HT film alters its SE energy spectrum, and find that the localised SE spectrum reflecting the presence of amorphous and crystalline phases in a semi-crystalline film. We investigate the origin of SE spectral features using both experimental and modelling approaches, and find that the different electronic properties of amorphous and crystalline P3HT (most notably electron affinity) cause SEs to be emitted with different energy distributions. The overall investigation is reported in Ref. [9].

7.2 Monte Carlo model

The simulation of the shape of secondary electron emission peak was realized by means of the Monte Carlo method as presented in section 2.1. A monoenergetic electron beam impinging on the target material was taken into account. The trajectories of both beam and secondary electrons were calculated. The emission spectrum was elaborated by collecting the electrons which escape from the material and counting them as a function of their kinetic energy to obtain the emission spectrum. All the 4 kinds of interactions were included in the model:

1. *the elastic scattering between electrons and atomic nuclei* was evaluated starting from the elastic scattering cross section by applying the Mott theory [10] (see section 2.1.1). The P3HT elastic scattering cross section was obtained by a linear combination of elastic cross sections of single elements which compose the molecule. Given the molecular composition of this organic compound equal to $C_{10}H_{14}S$, the resulting total elastic scattering cross section is obtained by the weighted sum of elastic scattering cross sections of the three constituent elements, where the coefficients of the combination are given by the stoichiometry of the compound. To determine the element elastic scattering cross section, the correspondent analytical formulation of atomic potential by Salvat was used [11]. The resulting total elastic scattering cross section is shown in Fig. 7.1.

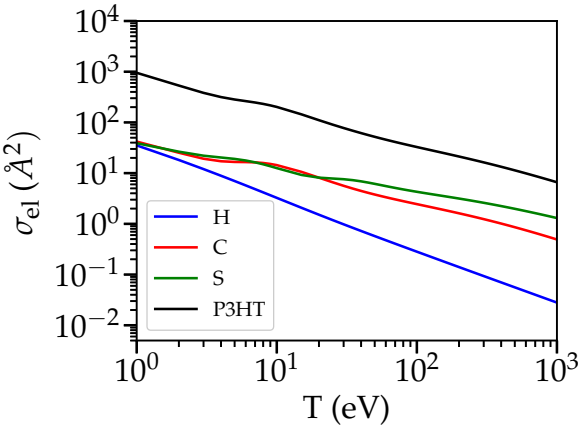

FIGURE 7.1: Total elastic scattering cross section of P3HT and of their component elements as a function of the kinetic energy.

Moreover, the Ganachaud and Mokrani correction was applied to the total elastic scattering cross section [12]. The parameter α equal to 0.01 eV^{-2} ensures the highest agreement with experimental data. The corrected total elastic scattering cross section and the correspondent elastic mean free path are shown in Fig. 7.2 as a function of the electron kinetic energy.

2. *the inelastic scattering between travelling electrons and target electrons* was considered by implementing the Ritchie dielectric theory. It involves the energy loss function, that is

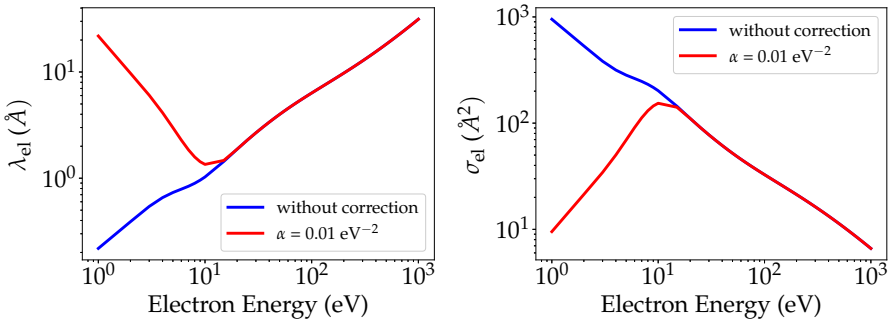

FIGURE 7.2: On the left elastic mean free path and on the right total elastic scattering cross section of P3HT, with or without the Ganachau and Mokrani correction.

n	E_n (eV^2)	Γ_n (eV)	A_n (eV)
1	2.80	0.913	0.265
2	22.50	15.000	268.313

TABLE 7.1: Fitting parameters ELF in the optical limit with D–L functions for P3HT [14].

described as a sum of Drude-Lorentz functions, representing electron oscillations [13] (section 2.1.2). The values of the strength, energy and width of the oscillators are proposed in Ref. [14] and reported in Tab. 7.1.

and the obtained energy loss function in the optical limit is shown in Fig. 7.3. This is composed by only two oscillators, with the one centered at 20 eV as the prominent. The first peak corresponds to π plasmon excitation and its influence on the SE spectrum will be discussed later.

Secondary electrons are generated as a result of inelastic interactions: if the energy loss of the travelling electron is larger than the threshold energy, this energy is transferred to an electron of a target atom. Thus, the secondary electron is emitted and also its trajectory is calculated. The threshold energy, in this case, was set equal to 2.5 eV, a value corresponding to the mean value of energy band gaps found in the literature [5].

3. *the electron-phonon interaction* was treated by applying the Froehlich theory [15] (see section 2.1.3). This interaction influences mainly the low energy electron region. The value of high frequency and static dielectric constants, respectively equal to ϵ_∞ = 3.6 and ϵ_0 = 3.0 [16], were employed in the calculation. Moreover, the single energy loss due to the electron-phonon interaction was set to W_{ph} = 0.05 eV [17].
4. *the trapping phenomenon* was dealt as reported in section 2.1.3 and the characteristics parameters were set, after a series of comparison with experimental records, to C_{trap} = 0.001 Å^{-1}, and γ_{trap} = 0.105 eV^{-1} [18].

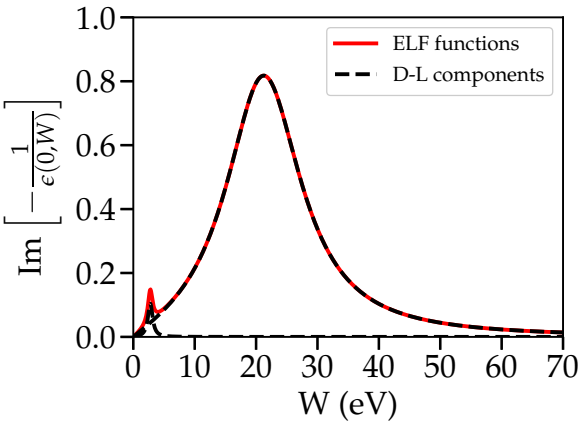

FIGURE 7.3: Energy loss function in the optical limit of P3HT, obtained with the fit function proposed by Drude - Lorentz [Eq. (2.16)] with the parameters provided by [14].

By considering these phenomena the interaction probabilities as a function of the electron energy (Eq. 2.4) result to be as shown in Fig. 7.4.

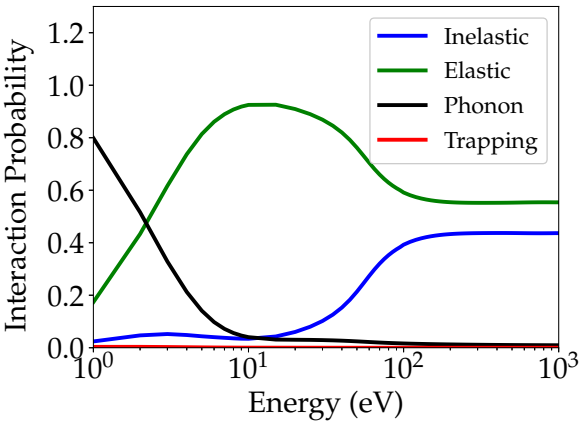

FIGURE 7.4: Interaction probabilities as a function of electron energy.

A key role in the calculation is represented by the electron affinity, acting as the energy barrier that electrons must overcome to be emitted. The surface of the P3HT shows amorphous and crystalline regions. To model this feature, regions with different electrons affinities were considered in the simulation.

7.3 Model results

The emission spectra were calculated by setting an initial kinetic energy of the beam to 700 eV. The number of primary electrons was set to 10^7, these are sufficient to produce significant low noise signals by considering the huge number of generated secondary electrons. This beam energy value, minimize experimentally the charging and electron beam damage issues, effects which are not accounted for in the Monte Carlo model. Two different samples were considered: (i) the semi-crystalline film and (ii) the amorphous film.

The accuracy of the MC method was verified by modelling the SE spectrum of an amorphous P3HT film. Indeed, amorphous P3HT is an ideal test case for this purpose; electron transport in an amorphous film is simpler to model due to its homogeneity [13]. We compared the modelled spectra with experimental spectra measured in the FEI Sirion tool (Fig. 7.5).

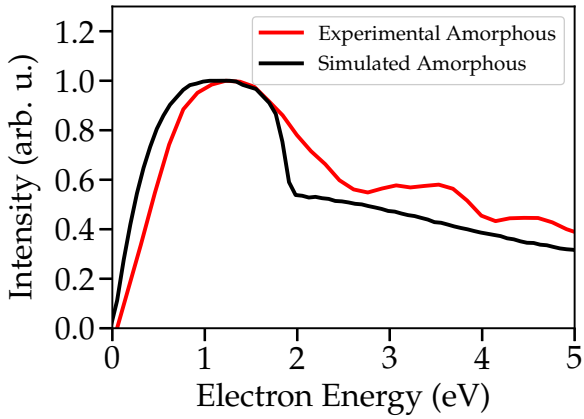

FIGURE 7.5: Comparison between calculated and experimental secondary electron emission spectra of amorphous P3HT, for energy of the beam equal to 700 eV [9].

The modelled spectrum demonstrates two primary features: a large, dominant peak at low energies (< 2 eV), with a long tail at higher energies. This produces a good match for the general shape of the experimental spectrum. With this model having successfully simulated the SE emissions of P3HT, we used it to investigate the effects of different sample parameters on the nature of the SE spectrum. In Fig. 7.6, the effect of altering the electron affinity on the simulated SE spectrum shape of P3HT can be observed.

The values of P3HT electron affinity in literature take a range of values, from 2.1 eV [5] to 3.2 eV [18], as such the χ values modelled in Fig. 7.6 (χ = 1.7 eV and χ = 2.5 eV) are a reasonable match to real P3HT films. This is especially the case given that measurements of P3HT electron affinity in the literature are bulk measurements that take no account of the localised variation. Moreover, in Fig.7.6 , we observe that with a higher electron affinity value, the low-energy peak becomes narrower and less intense. This is an unsurprising effect; the electron affinity can be taken as an analogue for the energy barrier that an internal SE must overcome if it is to be emitted. A larger electron affinity therefore has the effect 'cutting-off'

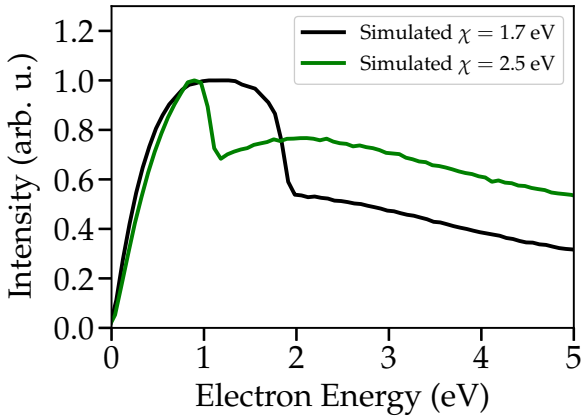

FIGURE 7.6: Comparison between two calculated spectra at different values of the electron affinity, for the beam energy equal to 700 eV [9].

low-energy SEs from the emitted spectrum, and 'compressing' the low-energy peak in to a smaller energy range. Due to the narrow low-energy peak at higher electron affinities, the higher-energy spectral feature that is observed as a tail for χ= 1.7 eV is revealed to be a peak at 2 eV in the χ = 2.5 eV spectrum. The shape and intensity of this feature is independent of the electron affinity value, indicating that it is representative of some other feature of the sample. Thus the effect of different electron affinity values on the SE spectrum shape can explain the 'double' peak feature observed around 1 eV in the wide-field SE spectrum of semi-crystalline P3HT. We model the semi-crystalline P3HT film as a two-phase system consisting of domains of different electron affinity. A SE can then be emitted from an area of the film with one of two electron affinity values. By setting the electron affinities of these two phases to χ = 1.7 eV and χ = 2.5 eV respectively, our modelled P3HT spectrum accurately recreates the double-peak feature around 1 eV. As the semi-crystalline P3HT sample emits a SE peak at lower energies than the amorphous sample, we ascribe an average χ = 2.5 eV to the crystalline phase, and an average χ = 1.7 eV to the amorphous phase. The relative intensities of the two peaks can be used to infer the fraction of the sample surface consisting of each domain. Modelled SE spectra from P3HT samples consisting of different fractions of crystalline and amorphous phase are observed in Fig. 7.7.

Matching the wide-field semi-crystalline SE spectrum, we roughly approximate from the wide-field spectra that 25% of the semi-crystalline P3HT film surface is crystalline. The absolute crystallinity content of P3HT films is difficult to compare with literature due to the effects of surfaces and interfaces on the absolute values [19].

Investigation on π plasmon peak The importance of π-electron plasmon excitations to the nature of the SE spectrum is a crucial sample feature in the discussion of molecular ordering. Indeed, the strength of the π-plasmon has been closely related to the presence of molecular ordering in the material as found in TEM-EELS studies [20, 21]. π-plasmon excitations are an

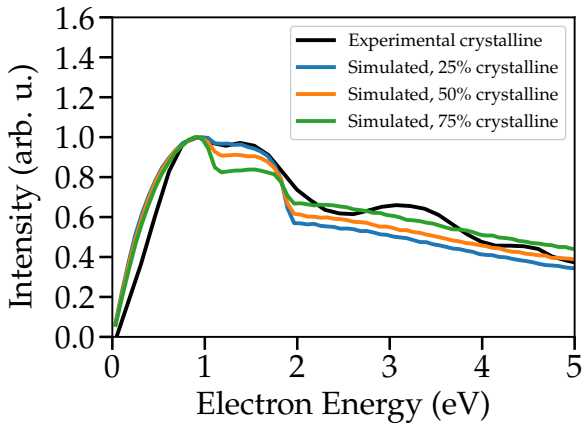

FIGURE 7.7: Simulating the SE spectrum of a semicrystalline P3HT film by considering the different electronic properties of amorphous and crystalline phases [9].

important factor in determining the SEs interactions within the material, and can influence the nature of the emitted SE spectrum as a result [14]. The model used to generate the previous spectra uses the low-loss electron energy loss-spectrum of P3HT films measured at 300 keV in the transmission electron microscope to calculate the nature of π-electron oscillations in real P3HT films as an input parameter. However, the interaction of P3HT with a 700 eV electron beam (as used in this study) and the 300 keV beam used to measure the π-plasmon properties is expected to differ. This is due to greater losses to surface plasmons and lower-energy plasmon oscillations at lower energies. In order to explore this effect, we increased the intensity of the π-plasmon oscillator in our model by up to 10 times and modelled the effect on the resulting SE spectrum in Fig. 7.8. We find that the shape of the low-energy peak does show a small reduction in the peak energy of this feature, although the shape of the spectrum does not change dramatically. For the qualitative nature of this modelling comparison, we therefore find that the π-plasmon as observed at 300 keV is a reasonable input parameter to our simulations.

Fig. 7.8 is also relevant for understanding how the presence of crystallinity in a material may affect its SE spectrum. Indeed these results also suggest that crystalline P3HT phases with a stronger π-electron structure would display a spectrum peak at lower energies. However, this effect is relatively small in comparison to that of electron affinity, and as such we expect that electron affinity remains the dominant effect.

7.4 Conclusions

In this work, we found that the shape of the SE spectrum of electrons emitted from P3HT samples in the SEM is dependent on the level of molecular ordering within the film. We demonstrated that specific SE spectral features can be linked empirically to crystalline content in the

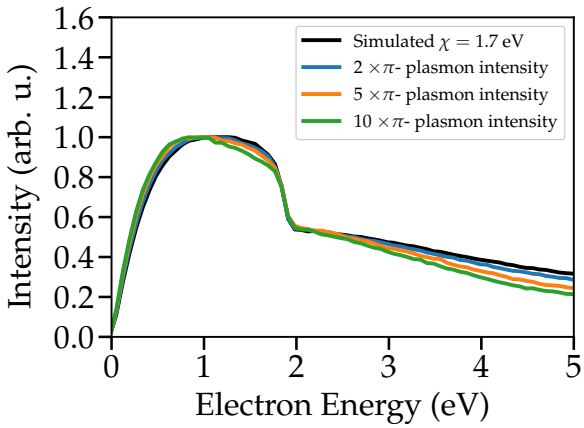

FIGURE 7.8: Comparison between two calculated SE spectra of P3HT, obtained for two different values of electron affinity [9].

film. By applying advanced Monte Carlo modelling techniques to simulate the shape of the P3HT SE spectrum, we showed that these spectral features linked to crystallinity can be related to the localised electronic properties of the film (themselves a function of localised molecular ordering). We found that the electron affinity of the sample is a dominant factor determining the shape of the spectrum. As electronic devices shrink to ever smaller sizes, considering these nanoscale variations will be of increasing importance.

Bibliography

[1] R. Willis, B. Feuerbacher, B. Fitton, Experimental investigation of the band structure of graphite, Physical Review B 4 (8) (1971) 2441.

[2] P. Kazemian, S. Mentink, C. Rodenburg, C. Humphreys, High resolution quantitative two-dimensional dopant mapping using energy-filtered secondary electron imaging, Journal of applied physics 100 (5) (2006) 054901.

[3] M. Dapor, Transport of Energetic Electrons in Solids, Vol. 257, Springer Tracts in Modern Physics, 2017.

[4] L. Biniek, S. Pouget, D. Djurado, E. Gonthier, K. Tremel, N. Kayunkid, E. Zaborova, N. Crespo-Monteiro, O. Boyron, N. Leclerc, et al., High-temperature rubbing: a versatile method to align π-conjugated polymers without alignment substrate, Macromolecules 47 (12) (2014) 3871–3879.

[5] K. Kanai, T. Miyazaki, H. Suzuki, M. Inaba, Y. Ouchi, K. Seki, Effect of annealing on the electronic structure of poly (3-hexylthiophene) thin film, Physical Chemistry Chemical Physics 12 (1) (2010) 273–282.

[6] U. Bielecka, P. Lutsyk, K. Janus, J. Sworakowski, W. Bartkowiak, Effect of solution aging on morphology and electrical characteristics of regioregular p3ht fets fabricated by spin coating and spray coating, Organic Electronics 12 (11) (2011) 1768–1776.

[7] C. Scharsich, R. H. Lohwasser, M. Sommer, U. Asawapirom, U. Scherf, M. Thelakkat, D. Neher, A. Köhler, Control of aggregate formation in poly (3-hexylthiophene) by solvent, molecular weight, and synthetic method, Journal of Polymer Science Part B: Polymer Physics 50 (6) (2012) 442–453.

[8] B. Park, A. Aiyar, J.-i. Hong, E. Reichmanis, Electrical contact properties between the accumulation layer and metal electrodes in ultrathin poly (3-hexylthiophene)(p3ht) field effect transistors, ACS applied materials & interfaces 3 (5) (2011) 1574–1580.

[9] R. C. Masters, N. Stehling, K. Abrams, V. Kumar, M. Azzolini, N. M. Pugno, A. Dapor, M.. Huber, P. Schäfer, D. G. . Lidzey, C. Rodenburg, Secondary electron energy spectroscopy in the scanning electron microscope: Origins and applications for a conjugated polymer, Advanced Science (2019) 1801752.

[10] N. Mott, The scattering of fast electrons by atomic nuclei, Proc. R. Soc. London, Ser. A 124 (794) (1929) 425.

[11] F. Salvat, J. Martnez, R. Mayol, J. Parellada, Analytical Dirac-Hartree-Fock-Slater screening function for atoms (Z= 1–92), Physical Review A 36 (2) (1987) 467.

[12] J. Ganachaud, A. Mokrani, Theoretical study of the secondary electron emission of insulating targets, Surf. Sci. 334 (1995) 329.

[13] M. Azzolini, T. Morresi, G. Garberoglio, L. Calliari, N. M. Pugno, S. Taioli, M. Dapor, Monte carlo simulations of measured electron energy-loss spectra of diamond and graphite: Role of dielectric-response models, Carbon 118 (2017) 299–309.

[14] M. Dapor, R. C. Masters, I. Ross, D. G. Lidzey, A. Pearson, I. Abril, R. Garcia-Molina, J. Sharp, M. Unčovskỳ, T. Vystavel, Secondary electron spectra of semi-crystalline polymers–a novel polymer characterisation tool?, J. Electron Spectrosc. Relat. Phenom. 222 (2018) 95–105.

[15] H. Fröhlich, Electrons in lattice fields, Advances in Physics 3 (11) (1954) 325–361.

[16] R. Singh, R. K. Singh, J. Kumar, R. Kant, V. Kumar, The origin of dc electrical conduction and dielectric relaxation in pristine and doped poly (3-hexylthiophene) films, Journal of Polymer Science Part B: Polymer Physics 48 (10) (2010) 1047–1053.

[17] J. Schafferhans, A. Baumann, A. Wagenpfahl, C. Deibel, V. Dyakonov, Oxygen doping of p3ht: Pcbm blends: Influence on trap states, charge carrier mobility and solar cell performance, Organic Electronics 11 (10) (2010) 1693–1700.

[18] J. Nolasco, R. Cabré, J. Ferré-Borrull, L. Marsal, M. Estrada, J. Pallares, Extraction of poly (3-hexylthiophene)(p3ht) properties from dark current voltage characteristics in a p3ht/n-crystalline-silicon solar cell, Journal of Applied Physics 107 (4) (2010) 044505.

[19] X. Shen, W. Hu, T. P. Russell, Measuring the degree of crystallinity in semicrystalline regioregular poly (3-hexylthiophene), Macromolecules 49 (12) (2016) 4501–4509.

[20] H. Ahn, D. Oblas, J. Whitten, Electron irradiation of poly (3-hexylthiophene) films, Macromolecules 37 (9) (2004) 3381–3387.

[21] M. Pfannmöller, H. Flugge, G. Benner, I. Wacker, C. Sommer, M. Hanselmann, S. Schmale, H. Schmidt, F. A. Hamprecht, T. Rabe, et al., Visualizing a homogeneous blend in bulk heterojunction polymer solar cells by analytical electron microscopy, Nano letters 11 (8) (2011) 3099–3107.

Chapter 8

Conclusions

In this thesis we presented different situations where the modeling and simulations were applied to deeply understand physical phenomena. In particular, the Monte Carlo method to simulate electron transport was developed and tested on different samples. Molecular dynamics simulations were performed to investigate the mechanical properties of 2D materials and the dynamic evolution of the peeling of a layer.

First of all, carbon-based materials were taken into account. Different dielectric models were tested in the modelling of electron transport in diamond and graphite[1]. Found out that the proper description is the one assessed by means of *ab initio* methods, this was applied to further develop the MC model. Indeed, the code was further improved to consider the influence of the anisotropic structure of graphite on the electron transport [2].

By carrying out molecular dynamics simulations, mechanical properties of graphene and adhesion energy between two layers of it were evaluated. Different simulations were performed to investigate the peeling of a graphene layer from a bulk of graphite. The implementation of these computational tools allowed the determination of the optimal conditions to achieve the peeling of the top layer without perturbing the substrate.

By considering as samples copper, silver and gold, the Monte Carlo method was also tested and compared to another numerical method based on the solution of the Ambartsumian-Chandrasekhar equations [3]. It was found that the method assures a remarkably good agreement with experimental data also in the evaluation of secondary electrons yield as a function of beam energy [4].

The modelling of electron transport in solid target was also applied in identifying the optimized conditions for the focused electron beam induced deposition (FEBID) technique in the deposition of 2D and 3D nanostructures. The case study of $W(CO)_6$ deposited on SiO_2 substrate was investigated. Simulations with SiO_2 as the target material were performed by considering high energy beam. The calculated radial energy distributions of emitted electrons represent input data for further irradiation driven molecular dynamics simulations. By the combination of these two different computational tools, the understanding of the overall process can be achieved.

Moreover, also in the field of organic electronic material, modelling and simulations can bring their contribution. Indeed, Monte Carlo simulations had a key role in understanding the influence of molecular ordering in the emission of secondary electrons in a sample composed by poly(3-hexylthiophene) (P3HT). The model was further developed to include areas of the sample surface with different electron affinities. This reflects the fact that differently ordered

molecules show different electronic properties that can be modeled by different values of the electron affinity [5]

In conclusion, we presented different cases of study in which computational tools substantially contribute to the overall understanding of the phenomena. The comparison with the experimental data and others simulated results were always performed in order to further develop and validate the methods. The aim to construct stable and general codes to produce predictive results remains the main focus. Following this path, the optimized conditions for proper applications of several samples can be a priori determined, avoiding expensive trail experiments.

Bibliography

[1] M. Azzolini, T. Morresi, G. Garberoglio, L. Calliari, N. M. Pugno, S. Taioli, M. Dapor, Monte carlo simulations of measured electron energy-loss spectra of diamond and graphite: Role of dielectric-response models, Carbon 118 (2017) 299–309.

[2] M. Azzolini, T. Morresi, K. Abrams, R. Masters, N. Stehling, C. Rodenburg, N. M. Pugno, S. Taioli, M. Dapor, Anisotropic approach for simulating electron transport in layered materials: Computational and experimental study of highly oriented pyrolitic graphite, The Journal of Physical Chemistry C 122 (18) (2018) 10159–10166.

[3] M. Azzolini, O. Riedzel, P. Kaplya, V. Afanasev, N. M. Pugno, S. Taioli, M. Dapor, Computational tools for calculating reel spectra in solids: a comparison between monte carlo method and the numerical solution of the Ambartsumian-Chandrasekhar equations,, Submitted.

[4] M. Azzolini, M. Angelucci, R. Cimino, R. Larciprete, N. M. Pugno, S. Taioli, M. Dapor, Secondary electron emission and yield spectra of metals from monte carlo simulations and experiments, Journal of Physics: Condensed Matter 31 (5) (2018) 055901.

[5] R. C. Masters, N. Stehling, K. Abrams, V. Kumar, M. Azzolini, N. M. Pugno, A. Dapor, M Huber, P. Schäfer, D. G. Lidzey, C. Rodenburg, Secondary electron energy spectroscopy in the scanning electron microscope: Origins and applications for a conjugated polymer, Advanced Science (2019) 1801752.

Appendix A

Elastic scattering cross section: calculation by using the analytical formulation of the atomic potential

The atomic potential employed in Eq. 2.7 can be obatined by *ab initio* calculation or by using an analytical formulation. The *ab initio* calculation provides the value of the potential for a set of distances. In the case of the analytical formulation, the potential is computed for the desired distance r by applying the correspondent formula. Here the formulation proposed by Salvat et al. is considered [1, 2]. The analytical formula is expressed, in atomic units, as:

$$V(r) = -\frac{Z}{r}\psi, \tag{A.1}$$

In particular, it takes into account the atomic screening function ψ that stands for the effect of the electron cloud. This screening function is expanded as:

$$\psi = \sum_{i=1}^{3} A_i^{\text{tab}} \exp(-\alpha_i^{\text{tab}} r), \tag{A.2}$$

with the condition $A_1^{\text{tab}} + A_2^{\text{tab}} + A_3^{\text{tab}} = 1$. The values of these constants for different elements are all reported in Ref. [1]. In order to use the obtained potential in the unit system of the previous formulation for the calculation of the elastic scattering cross section, the constants have to be scaled:

$$\begin{aligned} \alpha_i &= \alpha_i^{\text{tab}} \frac{K}{a_0}, \\ A_i &= A_i^{\text{tab}}. \end{aligned} \tag{A.3}$$

where the factor is $K = h/(2\pi mc)$, with h the Plank constant, m the electron mass and c the speed of light It is worth noting that the radius r is expressed in unit of $factor$, so to scale all the quantities the formulation for the potential is consistent. These values are multiplied by r that is expressed in unit of K. Therefore the potential is calculated with these corrections inside the program:

$$V(r) = \left[-\frac{Z\, e^2}{r\, K} \sum_{i=1}^{3} A_i^{\text{tab}} \exp(-\alpha_i^{\text{tab}} \frac{K}{a_0} r) \right] \frac{1}{mc^2}. \tag{A.4}$$

The differential cross section is given by the sum of square of the scattering amplitudes (Eq. 2.9); these are given by the sum on the angular momentum of functions dependent on the phase shift $\delta_l^{\pm}$. This is in turn dependent by the phases $\phi_l^{\pm}$ that are determined by solving the Dirac equation (Eq. 2.7) at large distance from the scattering center. Therefore, within an iterative cycle, that runs on the l-values, the values of $\phi_l^{\pm}$ were obtained integrating the Eq. (2.7) with the 4-th order Runge Kutta methods. It requires initial conditions. They were founded considering the series expansion of the potential at small distances r from the scattering center:

$$V(r) \rightarrow_{r\to 0} -\frac{Z_0 + Z_1 r + Z_2 r^2 + Z_3 r^3}{r}, \tag{A.5}$$

Comparing this with the Eq. (A.1) the coefficients can be computed as:

$$\begin{aligned}
\alpha_i &= \alpha_i^{tab} \frac{factor}{a_0}, \\
Z_0 &= \frac{Z\, e^2}{factor\, mc^2} \sum_{i=1}^{3} A_i = \frac{Z\, e^2}{factor\, mc^2}, \\
Z_1 &= -Z_0 \sum_{i=1}^{3} A_i \alpha_i, \\
Z_2 &= \frac{Z_0}{2} \sum_{i=1}^{3} A_i \alpha_i^2, \\
Z_3 &= -\frac{Z_0}{6} \sum_{i=1}^{3} A_i \alpha_i^3.
\end{aligned} \tag{A.6}$$

Then also phase functions can be expanded as:

$$\phi_l^{\pm} = \phi_{l0}^{\pm} + \phi_{l1}^{\pm} r + \phi_{l2}^{\pm} r^2 + \phi_{l3}^{\pm} r^3. \tag{A.7}$$

Replacing these expansions in Eq. (2.7), and considering the expansion up to the second order, the coefficients of the phase can be computed as:

$$\begin{aligned}
\phi_{l0}^{\pm} &= \sin^{-1}\left(-\frac{Z0}{k}\right), \\
\phi_{l1}^{\pm} &= \frac{W + Z_1 - \cos(2\phi_{l0}^{\pm})}{1 - 2k^{\pm} cos(2\phi_{l0}^{\pm})}, \\
\phi_{l2}^{\pm} &= \frac{2\phi_{l1}^{\pm}\sin(2\phi_{l0}^{\pm})(1 - k^{\pm}\phi_{l1}^{\pm} + Z_2)}{2 - 2k^{\pm}\, cos(2\phi_{l0}^{\pm})}, \\
\phi_{l3}^{\pm} &= \frac{2\phi_{l2}^{\pm}\, \sin(2\phi_{l0}^{\pm}\, (1 - 2k^{\pm}\phi_{l1}^{\pm} + 2\phi_{l1}^{\pm 2}\cos(2\phi_{l0}^{\pm})(1 - 2/3k^{\pm}\phi_{l1}^{\pm})}{3 - 2k^{\pm}\, \cos(2\phi_{l0}^{\pm})}.
\end{aligned} \tag{A.8}$$

Thus the initial value of the phase function can be computed. In order to obtain the phase functions at large distances from the scattering centre, the initial condition is integrated by using Eq. (2.7) with the Runge Kutta method formulated as:

$$\phi(r + dr) = \phi(r) + \frac{dr}{6}(h_0 + 2h_1 + 2h_2 + h_3), \tag{A.9}$$

with:

$$\begin{aligned}
h_0 &= \frac{k}{r}\sin[2\phi_l(r)] - cos[2\phi_l(r)] + W - V(r), \\
h_1 &= \frac{k}{r + \frac{dr}{2}}\sin[2(\phi_l(r) + h_0\frac{dr}{2})] - \cos[2(\phi_l(r) + h_0\frac{dr}{2})] + W - V(r + \frac{dr}{2}), \\
h_2 &= \frac{k}{r + \frac{dr}{2}}\sin[2(\phi_l(r) + h_1\frac{dr}{2})] - \cos[2(\phi_l(r) + h_1\frac{dr}{2})] + W - V(r + \frac{dr}{2}), \\
h_3 &= \frac{k}{r + dr}\sin[2(\phi_l(r) + h_2\, dr)] - \cos[2(\phi_l(r) + h_2\, dr)] + W - V(r + dr).
\end{aligned} \tag{A.10}$$

The phase shift $\delta_l^{\pm}$ can be evaluated using Eq.(2.8), for each value of l. Then the value of the scattering amplitudes is calculated using Eqs. (2.10) and (2.11) . Finally the value of the differential elastic scattering cross section is computed [Eq. (2.9)] [3].
In order to obtain the total cross section, the differential cross section is integrated:

$$\sigma_{\mathrm{el}} = \int \frac{d\sigma}{d\Omega} d\Omega = 2\pi \int_0^{\pi} \frac{d\sigma}{d\Omega}\sin(\theta) d\theta. \tag{A.11}$$

A C++ code was developed to calculate differential and total elastic cross section by applying the illustrated procedure. The results obtained, for the different investigated materials, were compared to the results obtained with the ELSEPA code [4] obtaining a good agreement in particular for energy greater than 100 eV. Our developed code allows to calculate elastic cross sections for low electron kinetic energy, below the limit of the ELSEPA code set at 50 eV. The knowledge of these features at lower energy results to be important in the simulation of

the secondary electrons generations, in the calculation of secondary electron emission spectra and secondary electron yield. High energy calculations of elastic cross sections are sufficient for the simulation of reflection electron energy loss spectra , since in this phenomenon electrons with kinetic energy higher than 50 eV are involved. Indeed, for the simulation of REEL spectra of metals (see Chapter 4.1.1) the ELSEPA code was employed in the calculation of input data.

Bibliography

[1] F. Salvat, J. Martnez, R. Mayol, J. Parellada, Analytical dirac-hartree-fock-slater screening function for atoms (Z= 1–92), Physical Review A 36 (2) (1987) 467.

[2] F. Salvat, R. Mayol, Elastic scattering of electrons and positrons by atoms. Schrödinger and Dirac partial wave analysis, Computer physics communications 74 (3) (1993) 358.

[3] M. Dapor, Transport of Energetic Electrons in Solids, Vol. 257, Springer Tracts in Modern Physics, 2017.

[4] F. Salvat, A. Jablonski, C. Powell, Elsepa—dirac partial-wave calculation of elastic scattering of electrons and positrons by atoms, positive ions and molecules, Computer physics communications 165 (2) (2005) 157.

Acknowledgments

I would like to thank my supervisors Prof. Nicola Pugno and Dr. Maurizio Dapor for their inspiring view and valuable support during my journey.
I am also grateful to Dr. Simone Taioli for his constant support and precious suggestions.
Then I would thank Dr. Giovanni Garberoglio for introducing me to the field of Computational Physics and for his encouraging questions.
I would like to express my gratitude to my colleagues of the first floor of the ECT* Rustico, Tommaso Morresi and Dr. Andrea Pedrielli, for their help and their friendship throughout this journey.
I thank K. Abrams, I. Abril, V. Afanasev, M. Angelucci, L. Calliari, R. Cimino, R. Garcia-Molina, P. Kaplya, R. Larciprete, R. Masters, O. Riedzel, C. Rodenburg, P. de Vera, N. Stehling for their inspiring discussions and collaborations.
I thank my family and Giacomo for their constant and precious support.

The aim of this thesis is the study of electronic transport and mechanical properties of materials using computer simulations. In particular, we dealt with the charge transport in semiconductor and metallic samples and with the peeling of a graphene layer from bulk graphite. The computational methods used to investigate the samples are (i) the Monte Carlo (MC) statistical method to simulate the transport of electrons in solids and (ii) the molecular dynamic (MD) approach to study the mechanical characteristics.
A relevant part of this thesis is focused on carbon-based material, such as diamond and graphite, and the stable two-dimensional allotrope, graphene. The response of diamond and graphite to external electromagnetic perturbations was investigated by calculating reflection electron energy loss (REEL) spectra with MC simulations. An extension to these models to describe the anisotropic response of graphite to an external electromagnetic perturbation was developed and included in the MC approach. Owing to the central role of carbon for future electronic and technological applications, also its mechanical properties were investigated by means of MD simulations. In particular, the peeling process of a layer of graphene from a bulk of graphite was investigated. This process is exploitable for graphene production and for adhesive applications of this material. Moreover, the MC approach was tested and compared to other computational techniques based on the solution of the Ambartsumian-Chandrasekhar equations. This consistency test was realized by considering three metals (copper, silver and gold) as target materials. Further studies were carried out on these materials by calculating secondary electron emission yields as a function of the electron beam energy.
Finally the MC approach was also used to investigate electron transport in SiO2 and in an organic polymer (P3HT). In this latter case, these studies allow a deeper knowledge of the influence of the molecular ordering in the secondary electron emission.

Martina Azzolini PhD candidate in Civil, Environmental and Mechanical Engineering, in a joint program between the University of Trento and Fondazione Bruno Kessler - ECT*. Her work focuses mainly on modeling and simulations of condensed matter systems. She holds a Master degree cum laude in Experimental Physics obtained at the University of Trento.